

DELFT UNIVERSITY OF TECHNOLOGY  
DEPARTMENT OF CIVIL ENGINEERING AND GEOSCIENCES

---

# Improving the quality control of Cofra Roller Compaction:

A study on the relation between the impact acceleration  
and the soil compaction

---

*Author:*  
D.V. Kalloe

Student number: 4360761  
Thesis committee: Dr. F. Pisanò, Geo-Engineering, TU Delft  
Dr. W. Broere, Geo-Engineering, TU Delft  
Dr. A. Tsouvalas, Offshore engineering, TU Delft  
J. Vink, Cofra B.V.  
J. Dijkstra, Cofra B.V.

in partial fulfillment of the requirements for the degree of

*Master of Science in Applied Earth Sciences*

February 19, 2020





# Abstract

Ground improvement in the form of soil compaction plays an important part in reclamation projects. The development of the Cofra Roller Compaction (CRC), a non-circular impact roller, has proven to be valuable in these projects. However, the heterogeneity of the subsoil causes locally a non-uniform degree of compaction. Traditional compaction control tests are limited in measuring depth, expensive and cause time delay. Therefore, the Continuous Compaction Control (CCC) and Continuous Impact Response (CIR) method were developed in order to provide more real-time information of the compaction based on the response of the drum of the roller. The aim of this study is to develop a semi-empirical energy model which is based on the contact forces of the roller-soil interface as most CCC systems, but also uses field test data as was given in the CIR system to validate this model.

The relevant parameters needed for this model were obtained from the field test conducted for the HES Hartel Tank Terminal project in Rotterdam. These included the impact acceleration, the cone resistance, the in situ density, the dynamic modulus and the dynamic plate load test velocity.

Two methods are considered in this thesis and both aim to reproduce the measured values from the dynamic plate load test during the field test. The first method considers the acceleration signals and includes double numerical integration of these signals to obtain the displacement, while the other considers modelling the roller as a dynamic plate load test and obtaining the displacement from solving a 2-DOF spring-mass-damper system.

However, after analysis of the motion of the roller, it was observed that due to the non-circular shape of the roller, a wedge effect was created where horizontal shearing forces caused loosening of the soil. This inhibited soil compaction up to 0.5 m depth. The impact acceleration signals were thus not representative of the soil compaction.

Nonetheless, the DPL-Soil model was proven to be successful in correlating the soil settlement to the dynamic modulus. This study considers a silty sand, so further research should be carried out to obtain correlations for various soils. In order to develop the semi-empirical energy model, it is thus recommended to capture an accurate acceleration response. This can be done by placing accelerometers at a minimum depth of 0.5 m, replacing the 8G accelerometer with e.g. 16G accelerometer and increasing the sampling rate to at least 1000 Hz. In order to filter out the soil variability, a field test with the roller should be performed on a homogeneous sand without fines. Correlations can then be drawn again for the same field tests performed in this thesis. Finite Element Modelling (FEM) could be used to model the interaction between the non-circular shape of the lobe, the rolling motion and the soil. This might form a better correction method for the acceleration signals than those explained in this thesis. Low frequency geophones can be used to measure the velocity directly. This because low frequency data of the accelerometer should be removed and the roller works on a low frequency. The load imparted to the ground could also be measured directly by burying earth pressure cells at a minimum depth of 0.5 m and at various depths to get a more accurate representation of the pressure distribution through the soil layers. By using other numerical integration methods such as Simpson's 3/8 rule and Boole's rule, the numerical accuracy of the displacement response of the roller could also be improved.



# Preface

This thesis has been produced as final work to fulfill my Master in Science program in Applied Earth Sciences at the Delft University of Technology. As part of an internship, this work was mainly carried out at Cofra B.V. in Amsterdam.

I first want to thank my thesis committee: Federico Pisanò, Wout Broere, Apostolos Tsouvalas, Jeroen Dijkstra and Jan-Willem Vink. I am grateful for your feedback, discussions and support during our meetings.

A special thank you goes out to Ruben and Kaj for helping me during the field test and coming up with fresh ideas and quick solutions. Furthermore, I want to thank Dr. Johannes Pistor for the skype meetings; these were proven to be very useful in this thesis.

I definitely cannot forget to thank my family and friends, Sudarshini, Boedjie, Avinash, and Misha, for being there for me. Finally, my parents for the unconditional love and support during these months.

*D. V. Kalloe  
Delft, February 2020*



# Contents

<b>List of Tables</b>	<b>vii</b>
<b>List of Figures</b>	<b>ix</b>
<b>Nomenclature</b>	<b>xiii</b>
<b>1 Introduction</b>	<b>1</b>
1.1 Problem description . . . . .	1
1.2 Research objective and questions . . . . .	1
1.2.1 Research objective . . . . .	1
1.2.2 Research questions . . . . .	2
1.3 Scope of the research . . . . .	2
1.4 Research approach and outline . . . . .	2
<b>2 Literature review</b>	<b>5</b>
2.1 Compaction . . . . .	5
2.2 Non-circular impact roller . . . . .	6
2.3 Cofra Roller Compaction . . . . .	7
2.4 CCC system . . . . .	8
2.5 CIR system . . . . .	9
2.6 Signal processing . . . . .	10
2.7 Past field tests . . . . .	12
2.8 Synthesis . . . . .	12
<b>3 Field test</b>	<b>13</b>
3.1 Trial location . . . . .	13
3.2 Soil . . . . .	14
3.3 Schedule of works . . . . .	15
3.4 Methodology . . . . .	16
3.4.1 Trial pits . . . . .	16
3.4.2 Cone penetration test . . . . .	17
3.4.3 Dynamic plate load test . . . . .	17
3.4.4 Nuclear density gauge test . . . . .	18
3.4.5 Vibration monitoring . . . . .	18
3.4.6 Standard proctor test . . . . .	19
3.5 Results . . . . .	20
3.5.1 Cone penetration test . . . . .	20
3.5.2 Dynamic plate load test . . . . .	24
3.5.3 Nuclear density gauge- and Standard proctor test . . . . .	25
3.5.4 Vibration monitoring . . . . .	26
<b>4 Correlations</b>	<b>29</b>
4.1 Peak acceleration . . . . .	29
4.2 Integrated peak velocities . . . . .	31
<b>5 Response of the roller</b>	<b>33</b>
5.1 Signal processing . . . . .	33
5.2 Displacement response of the roller . . . . .	38
5.2.1 Original displacement response . . . . .	38
5.2.2 Verification of numerical integration method . . . . .	39
5.2.3 Correction based on non-deformable surface . . . . .	39
5.2.4 Correction based on accelerometer in rest state . . . . .	41

<b>6</b>	<b>DPL-Soil model</b>	<b>43</b>
6.1	Model setup. . . . .	43
6.1.1	DPL . . . . .	43
6.1.2	Soil. . . . .	44
6.1.3	DPL-Soil interaction system . . . . .	44
6.2	Results . . . . .	45
<b>7</b>	<b>Discussion</b>	<b>47</b>
7.1	Field test . . . . .	47
7.2	Correlations. . . . .	48
7.3	Response of the roller. . . . .	48
7.3.1	Signal processing . . . . .	48
7.3.2	Displacement response . . . . .	48
7.4	DPL-Soil model . . . . .	49
<b>8</b>	<b>Conclusion</b>	<b>51</b>
<b>9</b>	<b>Recommendations</b>	<b>53</b>
	<b>Bibliography</b>	<b>55</b>
<b>A</b>	<b>Correlations</b>	<b>57</b>
A.1	Peak accelerations . . . . .	57
A.1.1	Mean peak acceleration of each cycle . . . . .	57
A.1.2	Peak acceleration of the last pass of each cycle. . . . .	58
A.1.3	Mean peak acceleration of the last pass of each cycle . . . . .	60
A.2	Integrated peak velocities . . . . .	61
A.2.1	Mean integrated peak velocities of each cycle . . . . .	61
A.2.2	Integrated peak velocity of the last pass of each cycle . . . . .	62
A.2.3	Mean integrated peak velocity of the last pass of each cycle . . . . .	64
<b>B</b>	<b>Displacement response of the roller</b>	<b>67</b>
B.1	Displacement response with band-pass filter of 1 to 28 Hz . . . . .	67
B.2	Displacement response for the first 5 passes at location 270 . . . . .	83

# List of Tables

2.1	Past field tests . . . . .	12
3.1	Overview of trial activities . . . . .	15
3.2	Overview of DPL test results for location 264 . . . . .	16
3.3	Overview of CPT's (lateral influence) . . . . .	23
3.4	Overview of DPL test results . . . . .	24
3.5	NDG results overview compared to Proctor results . . . . .	25



# List of Figures

1.1	Schematic overview of the research approach . . . . .	3
2.1	Compaction, (a) Compaction curves (Patel, 2019), (b) Stages of wetting during compaction (Based on (Hogentogler, 1937) . . . . .	5
2.2	Various roller shapes: (a) three-sided, (b) four-sided, (c) five-sided (Ranasinghe, 2017) . . . . .	6
2.3	Effectiveness of different compaction methods with respect to the nail/hammer analogy (Ranasinghe, 2017) modified from Pinard(1999) . . . . .	7
2.4	Motion of the CRC (CofraB.V., 2016) . . . . .	7
2.5	Roller dimensions (CofraB.V., 2018) . . . . .	8
2.6	Example of CRC data . . . . .	8
2.7	Current CCC systems (Cacciola, 2013) . . . . .	9
2.8	CIR maps (Kelly and Gil, 2012a) . . . . .	10
2.9	Frequency response to the Butterworth, Chebyshev, Elliptic and Bessel filter (EEEguide) . . . . .	11
2.10	Low-cut Butterworth filter in the frequency domain and the time domain with a cut-off frequency of 0.05 Hz (Boore and Bommer, 2005) . . . . .	12
3.1	Field test location . . . . .	13
3.2	Track definitions (a) & General layout (b) . . . . .	14
3.3	Grain size distribution curves (Mathijssen, 2019) . . . . .	14
3.4	Compactive effort (Cofra B.V.) . . . . .	15
3.5	Heaving and loosening of the topsoil due to the motion of the roller . . . . .	16
3.6	Preparing the trial pits . . . . .	17
3.7	CPT truck . . . . .	17
3.8	DPL test . . . . .	18
3.9	NDG test . . . . .	18
3.10	Vibration monitor . . . . .	19
3.11	Standard proctor test procedure . . . . .	19
3.12	CPT 281 . . . . .	20
3.13	CPT 264 . . . . .	21
3.14	CPT 270 . . . . .	21
3.15	CPT 284 . . . . .	22
3.16	CPT 267 . . . . .	22
3.17	Robertson and Campanella, 1990 . . . . .	23
3.18	Lateral influence CPT 270 at L3 . . . . .	24
3.19	Overview of DPL test results (averaged) . . . . .	25
3.20	Influence of compactive effort on compaction (flatGEO Consulting Company Limited)(after BS 1377 : 1990 - Part 4) . . . . .	26
3.21	Vibration velocity as a function of the distance between the roller and the vibration monitor . . . . .	26
3.22	Vibration acceleration as a function of the distance between the roller and the vibration monitor . . . . .	27
3.23	Measured vibration acceleration and corresponding roller acceleration . . . . .	27
4.1	In situ density vs. Maximum peak acceleration per cycle . . . . .	29
4.2	Dry density vs. Maximum peak acceleration per cycle . . . . .	30
4.3	Dynamic modulus vs. Maximum peak acceleration per cycle . . . . .	30
4.4	Average cone resistance vs. Maximum peak acceleration per cycle . . . . .	30
4.5	In situ density vs. Maximum integrated peak velocity per cycle . . . . .	31
4.6	Dry density vs. Maximum integrated peak velocity per cycle . . . . .	31
4.7	Dynamic modulus vs. Maximum integrated peak velocity per cycle . . . . .	32
4.8	Average cone resistance vs. Maximum integrated peak velocity per cycle . . . . .	32

5.1	Ellipse A2 8g accelerometer(systems, 2018) . . . . .	33
5.2	Accelerometer location on the centre of the drum axis . . . . .	33
5.3	Overview of raw accelerations signals per location . . . . .	34
5.4	Overview of Fourier spectra per location . . . . .	35
5.5	Unfiltered vs. filtered acceleration signal with a cut-off frequency of 28 Hz . . . . .	36
5.6	Unfiltered vs. filtered acceleration signal of 2 to 28 Hz . . . . .	37
5.7	Unfiltered vs. filtered acceleration signal of 3 to 28 Hz . . . . .	37
5.8	Unfiltered vs. filtered acceleration signal of 4 to 28 Hz . . . . .	37
5.9	Displacement response with a bandwidth of 1 to 28 Hz . . . . .	37
5.10	Displacement response with a bandwidth of 2 to 28 Hz . . . . .	37
5.11	Fourier spectra of mean acceleration signals . . . . .	38
5.12	Filtered Fourier spectrum of mean acceleration signals . . . . .	38
5.13	Displacement response of the roller after 5 passes at location 270 . . . . .	38
5.14	Integrated displacement response of the roller . . . . .	39
5.15	Differentiated velocity vs. integrated velocity . . . . .	39
5.16	Differentiated acceleration vs. roller acceleration signal . . . . .	39
5.17	Dropheight of the roller (Kelly) . . . . .	39
5.18	Displacement response of the roller after 5 passes at location 270 . . . . .	40
5.19	Unfiltered vs. Filtered mean acceleration signal after 5 passes at location 270 . . . . .	40
5.20	Corrected displacement response of the roller after 5 passes at location 270 . . . . .	41
5.21	Displacement response of the roller after 5 passes at location 270 . . . . .	41
5.22	Unfiltered vs. Filtered mean acceleration signal after 5 passes at location 270 . . . . .	42
5.23	Corrected displacement response of the roller after 5 passes at location 270 . . . . .	42
6.1	Mechanical model of the DPL (Adam and Adam, 2003) . . . . .	44
6.2	One-dimensional soil model of the elastic homogeneous halfspace (Adam and Adam, 2003) . . . . .	44
6.3	DPL-Soil interaction system (Adam and Adam, 2003) . . . . .	45
6.4	DPL field test vs. DPL-Soil model . . . . .	46
6.5	Correlation between the soil settlement and the dynamic modulus . . . . .	46
A.1	In situ density vs. Mean peak acceleration per cycle . . . . .	57
A.2	Dry density vs. Mean peak acceleration per cycle . . . . .	57
A.3	Dynamic modulus vs. Mean peak acceleration per cycle . . . . .	58
A.4	Average cone resistance vs. Average peak acceleration per cycle . . . . .	58
A.5	In situ density vs. Peak acceleration of the last pass per cycle . . . . .	58
A.6	Dry density vs. Peak acceleration of the last pass per cycle . . . . .	59
A.7	Dynamic modulus vs. Peak acceleration of the last pass per cycle . . . . .	59
A.8	Average cone resistance vs. Peak acceleration of the last pass per cycle . . . . .	59
A.9	In situ density vs. Mean peak acceleration of the last pass per cycle . . . . .	60
A.10	Dry density vs. Mean peak acceleration of the last pass per cycle . . . . .	60
A.11	Dynamic modulus vs. Mean peak acceleration of the last pass per cycle . . . . .	60
A.12	Average cone resistance vs. Mean peak acceleration of the last pass per cycle . . . . .	61
A.13	In situ density vs. Mean integrated peak velocity per cycle . . . . .	61
A.14	Dry density vs. Mean integrated peak velocity per cycle . . . . .	61
A.15	Dynamic modulus vs. Mean integrated peak velocity per cycle . . . . .	62
A.16	Average cone resistance vs. Mean integrated peak velocity per cycle . . . . .	62
A.17	In situ density vs. Integrated peak velocity of the last pass per cycle . . . . .	62
A.18	Dry density vs. Integrated peak velocity of the last pass per cycle . . . . .	63
A.19	Dynamic modulus vs. Integrated peak velocity of the last pass per cycle . . . . .	63
A.20	Average cone resistance vs. Integrated peak velocity of the last pass per cycle . . . . .	63
A.21	In situ density vs. Mean integrated peak velocity of the last pass per cycle . . . . .	64
A.22	Dry density vs. Mean integrated peak velocity of the last pass per cycle . . . . .	64
A.23	Dynamic modulus vs. Mean integrated peak velocity of the last pass per cycle . . . . .	64
A.24	Average cone resistance vs. Mean integrated peak velocity of the last pass per cycle . . . . .	65
B.1	Displacement response of the roller after 5 passes at location 1 . . . . .	68
B.2	Displacement response of the roller after 5 passes at location 2 . . . . .	69

---

B.3	Displacement response of the roller after 5 passes at location 264 . . . . .	70
B.4	Displacement response of the roller after 20 passes at location 264 . . . . .	71
B.5	Displacement response of the roller after 30 passes at location 264 . . . . .	72
B.6	Displacement response of the roller after 5 passes at location 267 . . . . .	73
B.7	Displacement response of the roller after 20 passes at location 267 . . . . .	74
B.8	Displacement response of the roller after 30 passes at location 267 . . . . .	75
B.9	Displacement response of the roller after 5 passes at location 270 . . . . .	76
B.10	Displacement response of the roller after 20 passes at location 270 . . . . .	77
B.11	Displacement response of the roller after 30 passes at location 270 . . . . .	78
B.12	Displacement response of the roller after 5 passes at location 281 . . . . .	79
B.13	Displacement response of the roller after 20 passes at location 281 . . . . .	81
B.14	Displacement response of the roller after 30 passes at location 281 . . . . .	82
B.15	Displacement response of the roller for 5 passes at location 270; Red signal depicts the filtered displacement response for the mean acceleration signal for 5 passes . . . . .	83



# Nomenclature

## **Abbreviations**

<i>AC20</i>	After compaction (20 passes)
<i>AC30</i>	After compaction (30 passes)
<i>AC5</i>	After compaction (5 passes)
<i>BC</i>	Before compaction
<i>CPT</i>	Cone penetration test
<i>CRC</i>	Cofra Roller Compaction
<i>DOF</i>	Degrees of freedom
<i>DPL</i>	Dynamic plate load
<i>HEIC</i>	High energy impact compaction
<i>HHTT</i>	HES Hartel Tank Terminal
<i>NDG</i>	Nuclear density gauge
<i>SMD</i>	Spring-mass-damper



# Introduction

This Chapter starts with the problem description, followed by the research objective and questions. Hereafter the scope of the research is given. Lastly, this Chapter is closed with the research approach and the outline of this report.

## 1.1. Problem description

Cofra B.V. is an innovative contractor specialising in ground improvement techniques and membrane construction. Their adaptation of the Cofra Roller Compaction (CRC) technique, a High Energy Impact Compaction (HEIC) technique, has proven to be of great advantage for the compaction of large reclamation projects.

However, the heterogeneity of the subsoil causes locally a non-uniform degree of compaction. This non-uniformity represents zones of overcompacted and undercompacted soil, potentially leading to differential settlements.

Hence, compaction control is required over the complete project site in order to determine the density or stiffness of the compacted layers. They are mainly executed using spot tests.

These spot tests carry their own complications such as (Adam and Brandl, 1997):

- Limited measuring depth of 20 to 40 cm
- Expensive
- Delay in construction work

The solution for this is the current state of the art method Continuous Compaction Control (CCC), which is already used for vibratory roller compaction and oscillatory roller compaction.

The current theory of CCC is based on smooth drum vibratory rollers where excentres cause a vibration and create a response from the subsoil. The non-circular drums of the CRC do not contain excentres and cause an impact on the subsoil due to the rotation of non-circular masses, the weight of each module (6 tonne) and the high towing speed of the tractor (10 - 15 km/h).

Currently there is no CCC method for impact rollers, however, Landpac developed a Continuous Impact Response (CIR) system, where site monitoring is performed by relating GPS- and acceleration data per impact to soil properties. The CRC has the availability to the same data.

## 1.2. Research objective and questions

### 1.2.1. Research objective

The aim of this thesis is to gain insight into the effect of a high energy impact compactor such as the Cofra Roller Compaction on the subsoil by usage of the accelerometer located on the centre of the axis of the drum.

The main research objective is formulated as:

*To develop a semi-empirical energy model which is based on the contact forces of the roller-soil interface as*

*most CCC systems, but also uses field test data as was given in the CIR system to validate this model*

These relevant parameters for the semi-empirical energy model are obtained from a field test and include the roller impact acceleration, the soil density and the dynamic modulus of the soil.

The sub-objectives include:

- Performing a field test and obtaining the relevant parameters
- Signal processing of the acceleration signals
- Obtaining the correct displacement response
- Developing the load-displacement curves
- Obtaining the model dynamic modulus and validation with the field test dynamic modulus

### 1.2.2. Research questions

The following research questions are answered to achieve the research objective.

1. Which soil properties influence the compaction of the soil?
2. What are the differences between the compaction control systems? (CCC vs. CIR)
3. What are the relevant parameters needed for the Roller-Soil model?
4. Which steps should be considered when analyzing acceleration data for displacement purposes?

## 1.3. Scope of the research

This thesis focuses on the compaction process of this interacting roller-soil system. The soil in this case is granular material and all other soil types are considered out of scope. The matric suction of the soil will also not be considered during the compaction process. An analysis of the motion of the roller with regard to the shape of the roller forms the critical part in developing the semi-empirical model. The complex dynamic soil behaviour is reduced to an one-dimensional wave propagation problem, which is represented by a frequency independent spring-mass-damper system with linear springs, viscous dampers and point masses. Data obtained from a field test performed at the Hartelstrook in the port of Rotterdam (HES Hartel Tank terminal) is used as validation of the model.

## 1.4. Research approach and outline

In order to fulfill the main research objective, this research is carried out by using two methods.

Both methods consider the dynamic modulus to prove soil compaction and aim to reproduce the measured values from the dynamic plate load test during the field test.

The first method considers the acceleration signals to determine the dynamic modulus. In order to obtain the correct displacement response, the acceleration signals are filtered and double numerically integrated. The corresponding load is also obtained from these corrected acceleration signals.

The second method considers the interface between the roller and the soil, to first be modeled as a dynamic plate load (DPL) test. The input for this DPL-Soil model is obtained from the field test measurements.

This model considers a 2-DOF system with corresponding spring stiffness and damper coefficients for the DPL and the soil. The obtained soil settlements are then validated with the measured soil settlements from the DPL.

The Roller-Soil model considers the spring stiffness and damper coefficient for the soil from the DPL-Soil model as input and incorporates the geometry of the roller. The schematic overview of the research approach is given in Figure 1.1.

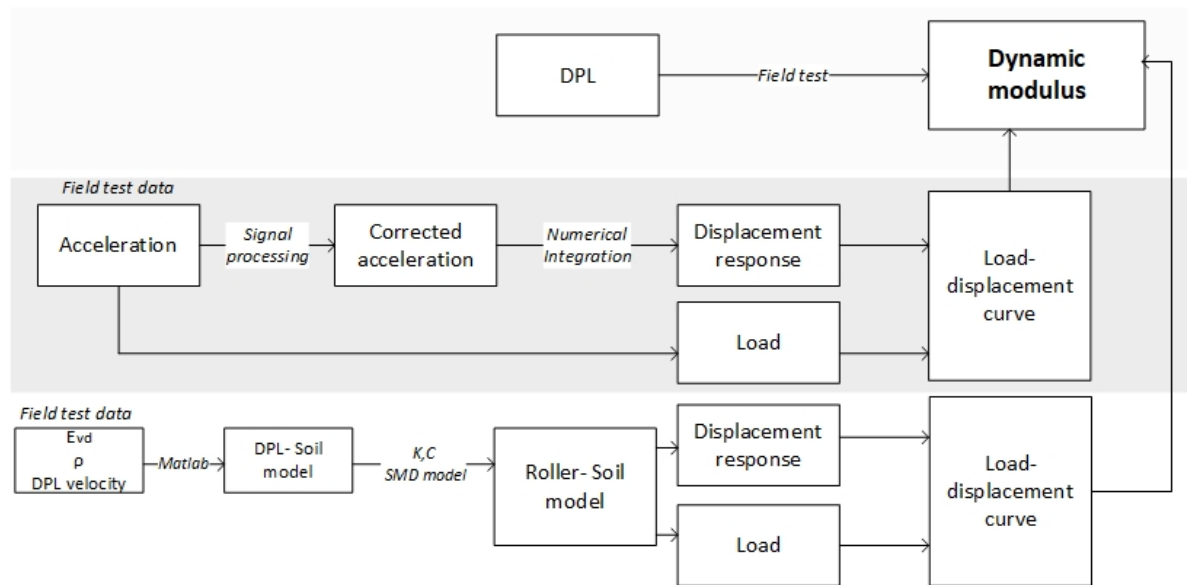


Figure 1.1: Schematic overview of the research approach

This report is structured in the following manner. Firstly, the literature review is presented in Chapter 2. This Chapter results in answering research questions 1 and 2. Subsequently Chapter 3 focuses on the methodology of the field experiments and the analysis of the obtained results. Afterwards the correlations of the peak impact accelerations and the integrated peak velocities with the obtained field test measurements are depicted in Chapter 4. Hereafter Chapter 6 follows, which introduces the DPL-Soil model and its purpose. Chapter 7 presents the discussion of the field test results, the correlations and the DPL-Soil model. Subsequently in Chapter 8 the answers to the research questions and the main research question are given. Lastly, recommendation for further research are stated in Chapter 9.



# 2

## Literature review

In this Chapter an overview is given of relevant literature. First, the compaction theory is explained, followed by a general overview of Cofra Roller Compaction. Hereafter, the current control systems for compaction, namely Continuous Impact Response (CIR) and Continuous Compaction Control (CCC), are presented.

### 2.1. Compaction

According to (Patel, 2019) compaction is the process of applying mechanical energy to a soil mass, causing rearrangement of the particles and densification through the expulsion of air from the voids between the soil grains. It has the following effect on engineering properties of the soil (Patel, 2019):

- Increase in shear strength and consequently the bearing capacity of the soil
- Increase in stiffness
- Decrease in void ratio and thus decrease in permeability

Figure 2.1(a) depicts the relationship between the moisture content and the dry density of various soils. An increasing water content leads to an increase in dry density until the optimum moisture content is reached, which corresponds to the maximum dry density, and hereafter the dry density decreases.

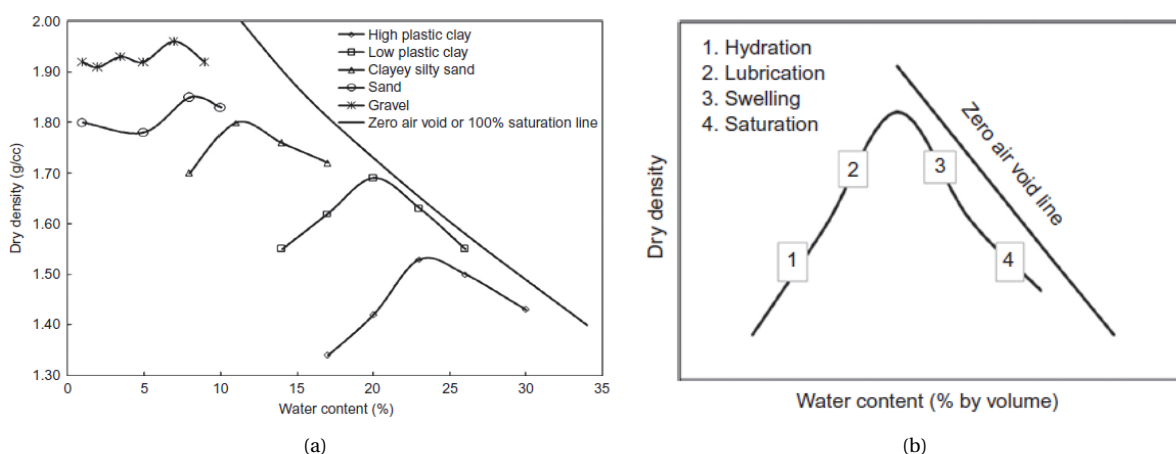


Figure 2.1: Compaction, (a) Compaction curves (Patel, 2019), (b) Stages of wetting during compaction (Based on (Hogentogler, 1937)

The general compaction methods in laboratory and in the field include static loading, impact loading, vibrating, rolling, gyrating, kneading and tamping. The effectiveness of these methods depend on the frictional

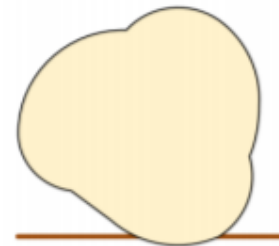
force between soil particles supported by the capillary action, and the lubrication effect of the moisture film around the soil particle. These consecutively depend upon the size, shape, soil mineralogy, and the pore water. Figure 2.1(b) shows the four stages of wetting the soil encounters during compaction. At the optimum moisture content, the compacting force is fully used to rearrange the soil particles to the most dense state due to neutralization of the capillary force as a result of the right amount of water (Patel, 2019).

## 2.2. Non-circular impact roller

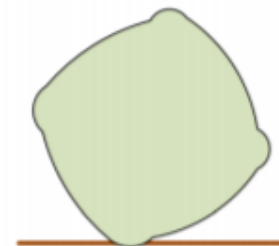
High energy impact compaction (HEIC) can be employed by various non-circular shaped roller. These include the three-, four- and five-sided roller depicted in Figure 2.2.



(a)



(b)



(c)

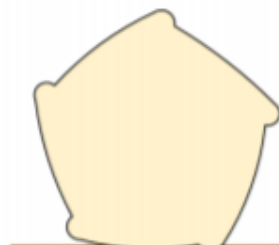


Figure 2.2: Various roller shapes: (a) three-sided, (b) four-sided, (c) five-sided (Ranasinghe, 2017)

The HEIC technique is a technique that densifies loose granular materials due to lifting and falling of the non-circular rotating masses. This method of compaction is also referenced in papers as rolling dynamic compaction (RDC). Due to the combination of potential and kinetic energy and the large mass of drums, this compaction technique produces a larger amount of compactive effort than traditional compaction techniques such as static and vibratory compaction. The amount of compactive effort can be related to the influence depth, as given in Figure 2.3.

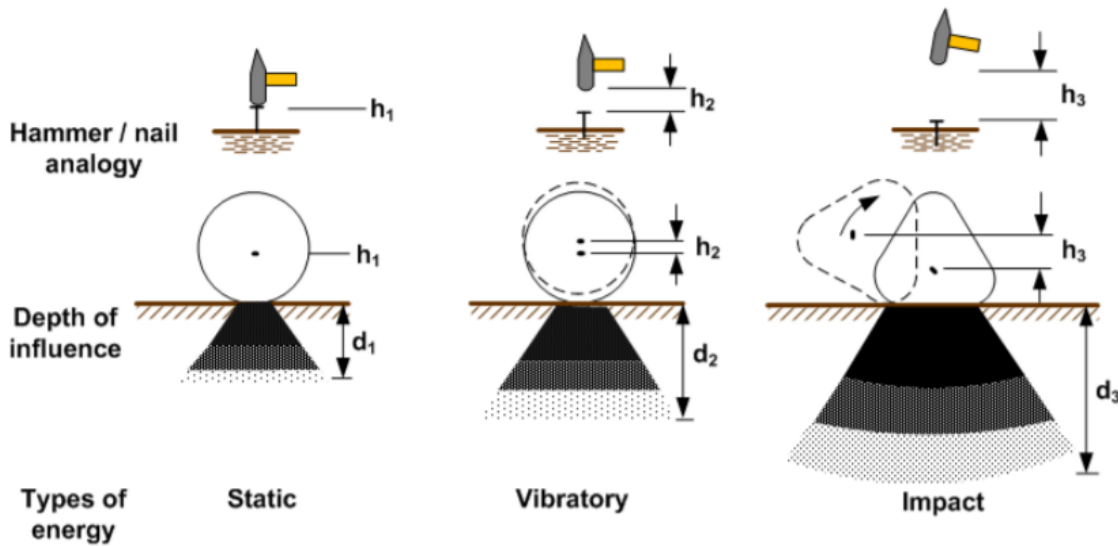


Figure 2.3: Effectiveness of different compaction methods with respect to the nail/hammer analogy (Ranasinghe, 2017) modified from Pinard(1999)

### 2.3. Cofra Roller Compaction

The Cofra Roller Compaction (CRC) is a three-sided impact roller, which uses a high energy impact compaction (HEIC) technique. As the name suggests, this technique is based on the high energy generated by the roller by means of the lifting and falling motion of the non-circular rotating masses. This motion is depicted in Figure 2.4.

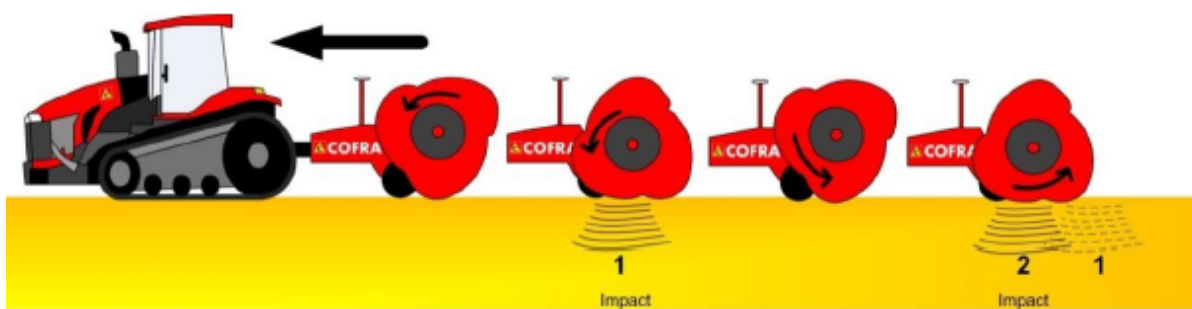


Figure 2.4: Motion of the CRC (CofraB.V., 2016)

The CRC consists of

- a roller with two modules
- a tractor
- a data recording system

The dimensions of the roller are given in Figure 2.5.

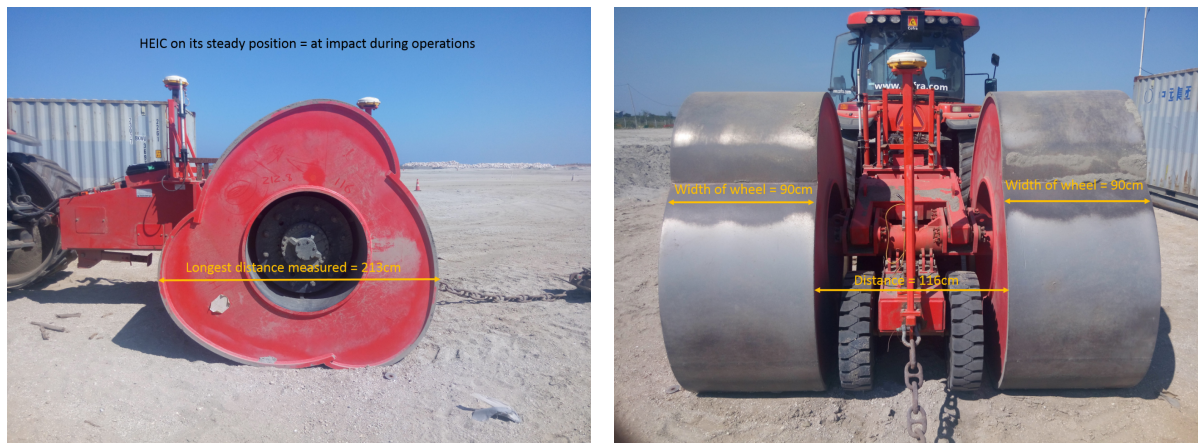


Figure 2.5: Roller dimensions (CofraB.V., 2018)

The data recording system consists of GPS trimbles and an accelerometer. The accelerometer is located on the drums tube axle. With each impact, the location coordinates, deceleration and the number of passes is recorded in this system. An example of this data is given in Figure 2.6.

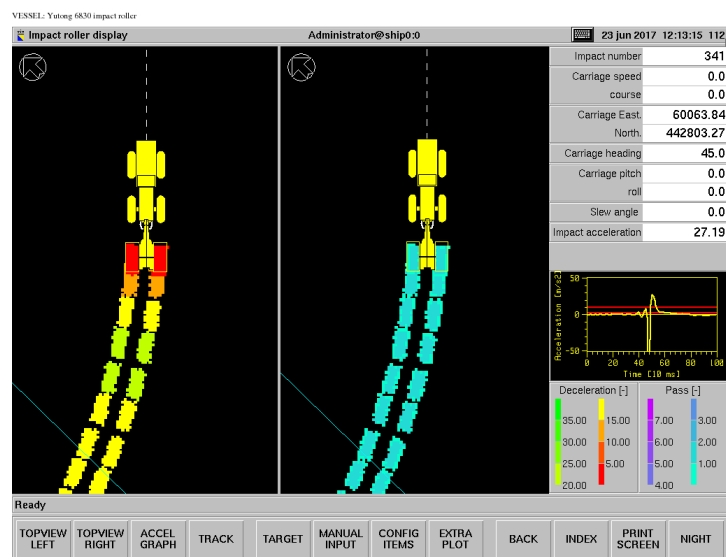


Figure 2.6: Example of CRC data

The levelling unit is not part of the basic setup. This is needed to prevent wear of the equipment due to the uneven ground and high speed. It can either be attached to the roller or to a separate machine. The former will cause a decrease in roller speed and impact energy, while the latter will have no such effect.

## 2.4. CCC system

The Continuous Compaction Control (CCC) systems have been the state of the art method when assessing the compaction of the soil due to vibratory rollers. The current control systems consists of the following systems depicted in Figure 2.7.

CCC System	CCC Value	Definition of CCC Value	Manufacturer
Compactometer	CMV (unitless)	acceleration amplitude ratio (first harmonic divided by excitation frequency amplitude) – frequency domain	Geodynamik
Terrameter	OMEGA (N.m)	energy transferred to soil considering soil contact force displacement relationship of two excitation cycles – time domain	Bomag
Continuous Compaction Value	CCV (unitless)	acceleration amplitude ratio – frequency domain	Sakai
Terrameter	$E_{vb}$ (MPa)	dynamic elasticity modulus of soil beneath drum (inclination of soil contact force displacement relationship during loading) – time domain	Bomag
Ammann Compaction Expert	$k_s$ (MN/m)	spring stiffness of soil beneath drum (derived from soil contact force displacement relationship at maximum drum deflection) – time domain	Ammann
Machine Drive Power	MDP (kW)	net power to propel the roller	Caterpillar

Figure 2.7: Current CCC systems (Cacciola, 2013)

According to (Pistol et al., 2016) the basic principle of the CCC is to assess the soil stiffness by evaluating the motion behaviour of the dynamically excited drum.

Therefore in order to develop this system, the parameters that influence the motion behaviour should be kept constant such as the roller operating parameters (e.g. velocity), and the motion behaviour should be recorded (Pistol et al., 2016).

## 2.5. CIR system

The Continuous Impact Response (CIR) system, which is developed by Landpac, monitors the response of the soil due to loads induced by their HEIC. The system uses the accelerometer, which is placed on the axle between the two modules. The acceleration is measured continuously and the peak deceleration is recorded at each impact. These peak decelerations give an indication of the response of the soil, where lower decelerations indicate a softer response and an increase in deceleration indicate a stiffer soil.

In order to provide a more qualitative answer, the decelerations are related to an appropriate traditional engineering measurement catered to the particular site. These include cone penetration testing, dynamic cone penetration, plate load testing, zone load testing or california bearing ratio, which are performed at the specific points where deceleration data is measured. Using the GPS data the system then generates a color coded map, which indicates the relative measure of the appropriate engineering property (Landpac). An example is given in Figure 2.8.

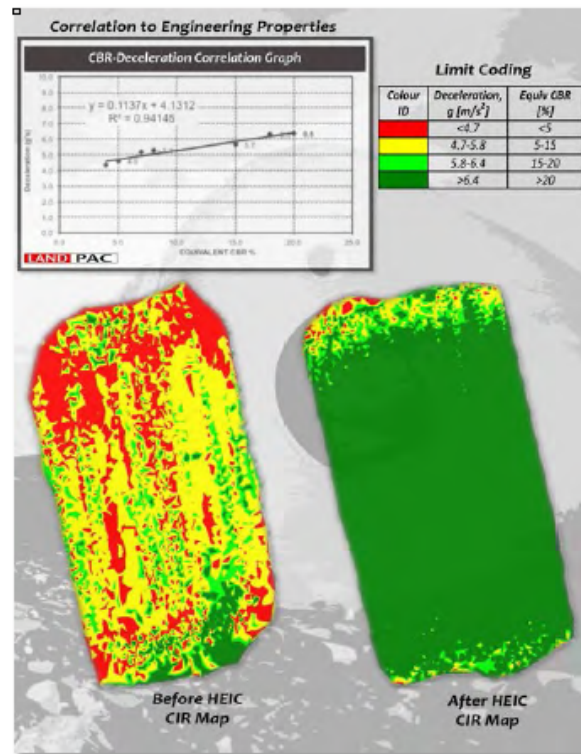


Figure 2.8: CIR maps (Kelly and Gil, 2012a)

## 2.6. Signal processing

Processing of the acceleration signals depend upon the usage of it. Given that displacement is to be quantified from the double numerical integration of the acceleration-time signals, the following should be implemented in the code (Tsouvalas, 2019):

- Detrending of the data
- Type of filter
- Cut-off frequency
- Order of filter
- Acausality or causality
- Numerical integration method

The specifications of the accelerometer determine the frequency bandwidth in which the response can be recorded. In order to capture an accurate ground response and ensure an accurate double numerical integration of the acceleration-time data, the accelerometer should use a sampling frequency of 4 kHz (Scott et al., 2019).

Before filtering the data, the mean of each signal should be subtracted in order to detrend the data and prevent phase shifting of the signal. The accelerometer already contains an anti-aliasing filter. By further filtering the data, the absolute value of the error in position could be reduced, however there is still a chance for the variation in the positional error to increase with time (Thong et al., 2002). The frequency resolution plays a big part in the analysis of this data. The finest frequency resolution would be (Rogers et al., 1997)

$$dF = \frac{f_s}{N} \quad (2.1)$$

where  $dF$  = frequency resolution [Hz],  $f_s$  = sampling rate [Hz] and  $N$  = number of data points analyzed [-]  
 It should be noted that there is no 'best' method for filtering; it is subjective.

Filtering can take place in either the time domain or the frequency domain. In the time domain it is performed by a convolution of the transform of the filter and the actual signal, while in the frequency domain, the acceleration-time data is constructed in the frequency domain by applying a Fourier transform and afterwards identifying the lower and upper limits of the interested frequency range. Regardless of which domain is chosen, the filtered result will remain the same (Tsouvalas, 2019).

Three types of filters exist namely low-pass filters, high-pass filters and band-pass filters. As the name suggest, a low-pass filter allows frequencies lower than the stated cut-off frequency to pass through, while a high-pass filter allows frequencies higher than the stated cut-off frequency to pass through. A band-pass filter allows frequencies within a certain bandwidth to pass through.

A wide range of generic filters are available including Butterworth, Chebyshev, Elliptic and Bessel. A simplified overview of the frequency response to these filters is given in Figure 2.9.

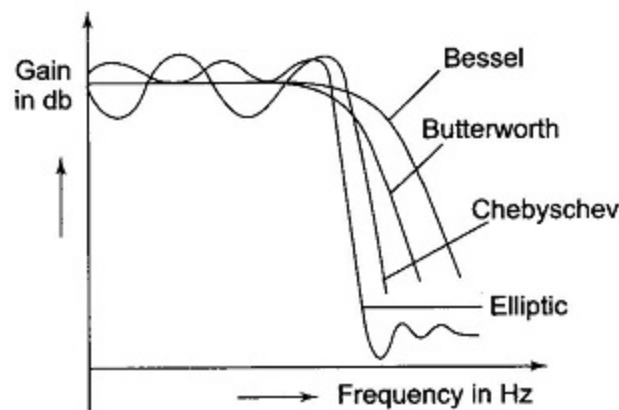


Figure 2.9: Frequency response to the Butterworth, Chebyshev, Elliptic and Bessel filter (EEEguide)

The following can be noted from Figure 2.9:

- The Butterworth filter has the flattest pass-band but a poor roll-off rate.
- Compared to the Butterworth filter, the Chebyshev filter has a steeper roll-off rate, but some pass-band ripple.
- The Elliptic filter has the steepest roll-off rate, but it also contains some pass- and stop-band ripple.
- The Bessel filter has the worst roll-off rate, but the best phase response.

The identification of the cut-off frequencies plays a big role in obtaining a correct displacement response from the acceleration signal. The upper limit of the frequencies depend on the accelerometer specifications and the sampling rate, while the lower limit depends on the observed time window (Tsouvalas, 2019).

Furthermore, the order of the applied filter also plays a role in filtering. As depicted in Figure 2.10, an increase in order is linked to a more abrupt cut-off, while a lower order filter might remove valuable information.

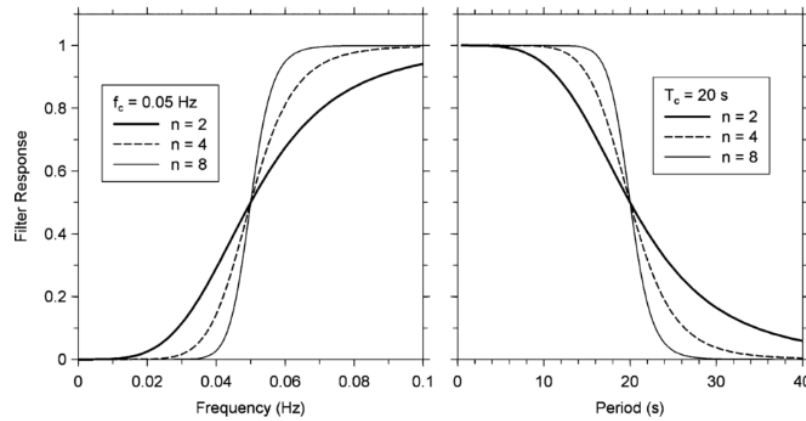


Figure 2.10: Low-cut Butterworth filter in the frequency domain and the time domain with a cut-off frequency of 0.05 Hz (Boore and Bommer, 2005)

A filter is called causal if its output only depends on current and past inputs, while acausal filters are outputs of past and future inputs. An acausal filter is recommended in this case, considering that it prevents phase distortion in the signal.

After acceleration signals are corrected, the velocity and displacement response can be obtained by two methods. This can be done by either direct time integration of the acceleration signal or transformation in the frequency domain and inverse transformation back in time (Tsouvalas, 2019).

## 2.7. Past field tests

Relevant past field experiments can be found in Table 2.1. These mostly include the three-sided roller. However, in order to discuss the lateral extent of the roller, (Jaksa et al., 2012) is added to this table.

Table 2.1: Past field tests

Roller type	Tests performed	Soil type	Influence depth [m]	Reference
3-sided	CPT	Loose to very loose marine sands	4	(Kelly et al., 2000)
3-sided and 5-sided	CPT	Very loose marine sands	4-5	(Kelly et al., 2000)
3-sided	CIR and geophones	Waste material with underlying loose to dense sand	4	(McCann and Schofield, 2007)
3-sided	CPT	Dredged marine sands	5	(Kelly and Gil, 2012b)
3-sided	CPT and DPL	Coarse grained marine sands	3	(Kelly and Gil, 2012b)
4-sided	EPC, sand replacement test and DCP	Well-graded sand with clay fines of low plasticity	3	(Jaksa et al., 2012)

## 2.8. Synthesis

The thesis focuses on combining the CCC and CIR system, by developing a semi-empirical energy model which is based on the contact forces of the roller-soil interface as most CCC systems, but also uses field test data as was given in the CIR system to validate this model.

# 3

## Field test

In this chapter the field test is described. The goal of this test was to determine the influence depth and lateral extent of the CRC roller and the soil properties that affect the compaction of the soil.

### 3.1. Trial location

The field test took place in Rotterdam depicted below. It is currently under development and part of the HES Hartel Tank Terminal project, where it will end up being used for the storage and transhipment of oil products and biofuels (PoR). Depending on the filling process and previous traffic movement (dozers etc.), the compaction degree can be quite significant above the water table.



Figure 3.1: Field test location

The general layout is given in Figure 3.2, which also includes the path of the roller. GPS data was available from the roller, dynamic plate load (DPL) test, nuclear density gauge (NDG) test, proctor test and the vibration monitor. However, the GPS coordinates obtained from the DPL test were proven to be quite inaccurate, extending to even a difference in 30 m. Subsequently, these could not be used and are not given in the general layout. These coordinates were thus approximated to the NDG coordinates. It should also be noted that the test consisted of two tracks with the following track definition given in Figure 3.2. After compacting the first sub-track the CRC is shifted one wheel-width on to the second sub-track (1b). Together they form one track and this is defined as 1 compaction pass. The same follows for track 2.

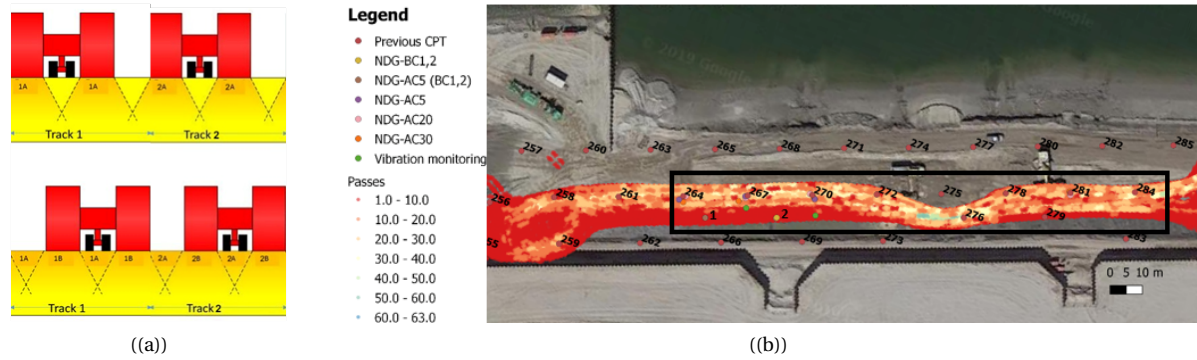


Figure 3.2: Track definitions (a) & General layout (b)

### 3.2. Soil

At location CPT 407 three samples were taken at respectively 1 m, 2 m and 3 m depth. The grain size distribution curves for these samples are given in figure 3.3.

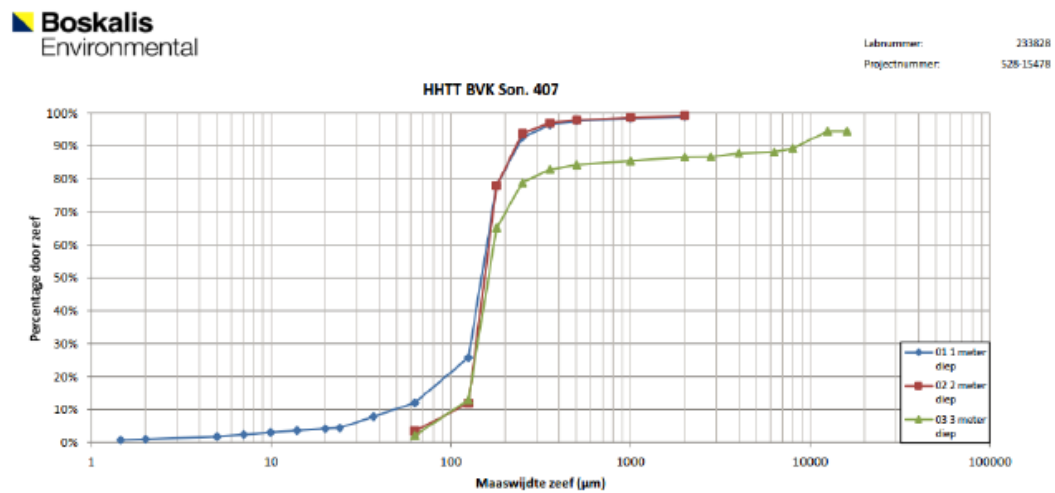


Figure 3.3: Grain size distribution curves (Mathijssen, 2019)

This resulted in the following (Mathijssen, 2019):

- The soil consists of an uniform sand with an uniformity coefficient  $C_u$  of 1.5 – 1.7. This poorly graded sand demands more compactive effort to reach the same compaction as opposed to a well graded sand. This can also be seen in Figure 3.4.
- Sample 1 has a higher uniformity coefficient. However, this is due to the relatively large amount of silt.
- The fine material of the samples (< 63 m) only consist of non-plastic silt.
- Overall there is a low average grain diameter  $D_{50}$  (i.e. 150 m), low uniformity coefficient and between 0 to 20 % silt.

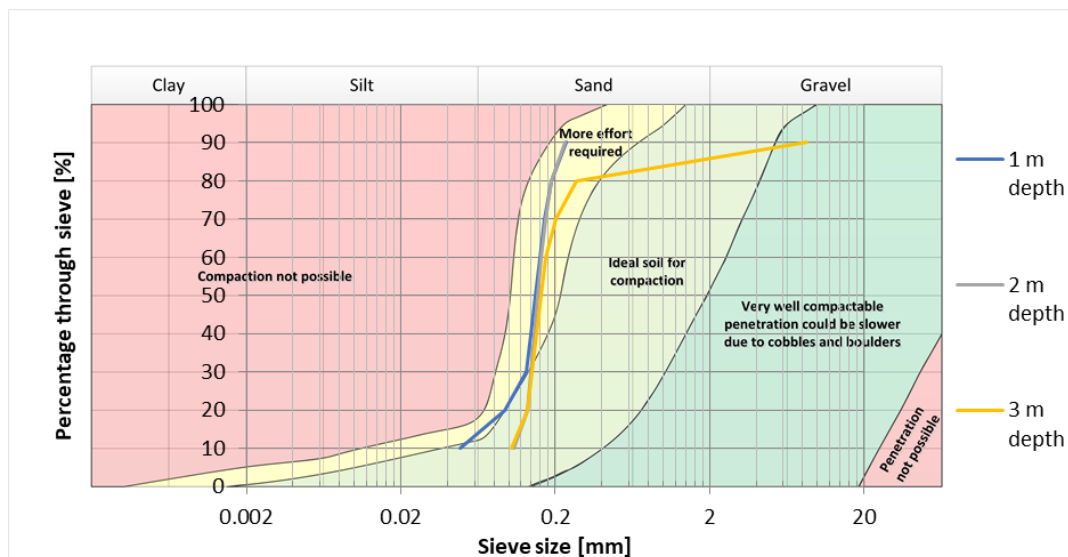


Figure 3.4: Compactive effort (Cofra B.V.)

### 3.3. Schedule of works

The schedule of activities regarding the field test are presented in Table 3.1, where the red font represents the cone penetration tests performed on the tracks and the green font represents the cone penetration tests performed next to the tracks.

Table 3.1: Overview of trial activities

Activities	Amount	Date
Pre-CPT* (on the track)	6	Day 1
Pre-CPT (next to the track)	1	Day 1
Samples for Proctor test	4	Day 1
DPL test	4	Day 1
Roller compaction 5 passes	-	Day 1
Post CPT*'s after 5 passes	6	Day 1
Post CPT's after 5 passes	4	Day 1
NDG after 5 passes	7	Day 1
DPL test	7	Day 1
Samples for Proctor test	2	Day 2
Roller compaction 20 passes	-	Day 2
Post CPT*'s after 20 passes	4	Day 2
Post CPT's after 20 passes	2	Day 2
NDG after 20 passes	4	Day 2
DPL test	4	Day 2
Roller compaction 30 passes	-	Day 2
Post CPT*'s after 30 passes	4	Day 2
Post CPT's after 30 passes	2	Day 2
NDG after 30 passes	4	Day 3
DPL test	4	Day 3
Roller compaction 5 passes	-	Day 3
NDG after 5 passes	2	Day 3
DPL test	2	Day 3

### 3.4. Methodology

Various tests were performed during this field test such as CPT, DPL tests and NDG tests. These were performed before compacting the soil with the roller, and after 5, 20 and 30 passes with the roller. Furthermore, a vibration monitor was placed to measure the vibrations caused by the roller and soil samples were taken to perform laboratory tests such as the proctor test. This section describes the method for each test.

#### 3.4.1. Trial pits

As previously mentioned, the roller impacts the ground due to the non-circular shape of the roller and the towing velocity of the tractor. The roller hits the ground surface with the flat part of the lobe and the wedge part of the lobe pushes the topsoil forward due to the constant towing velocity, depicted in Figure 3.5. As a result of this, the soil remains looser till approximately 0.5 m depth (Kim and Chun, 2016). Hence, the NDG and the DPL tests, which are surface tests, were unable to deliver results which could be compared to the BC results. Thus, it was decided to respectively dig 10 cm, 20 cm and 50 cm of soil and perform these tests at location 264. By comparing this to the value obtained before compacting the soil, the relevant depth could be approximated. This is given in Table 3.2.



Figure 3.5: Heaving and loosening of the topsoil due to the motion of the roller

Table 3.2: Overview of DPL test results for location 264

Type	Depth [m]	Dynamic modulus E <sub>vd</sub> [MPa]
BC	0	40.11
AC5	0	17.46
	0.1	25.37
	0.2	30.12
	0.5	46.78

The decision was made to make pits with length of 2.5 m, width of 2.2 m and depth of 0.5 m, to perform these tests. After execution of these tests, the pits were covered and the roller could be used again. This is depicted in Figure 3.6.

After the roller performed a total of 20 passes, the post-CPT's were taken and again the pits were dug to perform the NDG and DPL tests. The same method followed after 30 passes. Considering that the pre-compaction data could not be used for comparing due to the depth difference, two new pits were dug up next to the tracks. These pits serve to see the comparison in results between before compaction and after compacting the soil with 5 passes.



Figure 3.6: Preparing the trial pits

### 3.4.2. Cone penetration test

Cone penetration tests were performed on the track and next to the track at a depth of around 5 m. The measured cone resistance is used to determine respectively the depth- and lateral influence of the CRC. The GPS coordinates for the performed CPT's could not be recovered. However, considering the close proximity of these to the previous CPT's and the NDG tests, the assumption was made to use the GPS coordinates of the latter tests which are given in the general layout depicted in Figure 3.2. Figure 3.7 shows Geonius performing the CPT's.



Figure 3.7: CPT truck

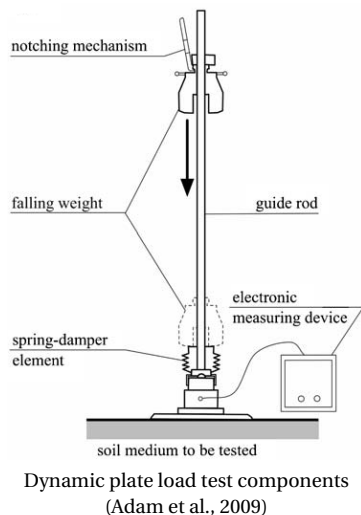
### 3.4.3. Dynamic plate load test

The dynamic plate load test with the light weight falling device is used to determine the deformation modulus of the soil. It is based on the dynamic soil response by application of an impact-like load to a load plate (Adam et al., 2009). The components of this device are depicted in Figure 3.8.

This test is performed by first pre-loading the soil by applying three impacts to ensure full contact between the load plate and the soil. Hereafter the plate is connected to the computer and it should be noted that the GPS-position should be visible on the display. Subsequently a sequence of three pulses is applied where each pulse measures the peak vertical displacements of the load plate, which coincides with the settlement of the soil surface.

The maximum stress exerted on the soil is assumed to be constant and equal to  $0.1 \text{ MN/m}^2$ . The dynamic modulus is then calculated according to Equation 3.1, where  $s_{max}$  is the maximum displacement and the average of the previously measured peak settlements.

During the field test it was performed on six locations namely 1, 2, 264, 267, 270 and 281.



Performing the DPL test

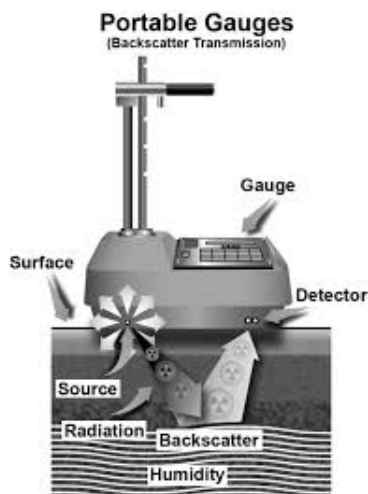
Figure 3.8: DPL test

$$E_{vd}(MN/m^2) = \frac{22.5}{s_{max}(mm)}, \quad (3.1)$$

#### 3.4.4. Nuclear density gauge test

The NDG test depicted in Figure 3.9 is performed at 0.5 m depth.

It uses low level radiation to measure the wet density, dry density and moisture content of soil. Gamma rays are emitted at the tip of the source rod and the resulting radiation is measured in the base of the gauge. By means of this the density of the soil is then calculated. The moisture content is determined by measuring the hydrogen as a result of neutron emissions in the gauge (The Virginia Department of Transportation , VDOT).



Nuclear density gauge test (The Virginia Department of Transportation , VDOT)



Performing the NDG test

Figure 3.9: NDG test

#### 3.4.5. Vibration monitoring

The Profound VIBRA vibration monitor is depicted in Figure 3.10. It registers continuously the vibration peak values over time namely velocity in x-, y- and z- direction.



Figure 3.10: Vibration monitor

### 3.4.6. Standard proctor test

According to Proctor, soil compaction depends on the following factors:

- Soil type,
- Moisture content
- Compactive effort
- Dry density of the soil

By assuming the same soil type and compactive effort, the relationship remains that the dry density of the soil will vary with moisture content. In order to perform this laboratory test, soil samples were taken at the locations of the NDG tests given in Figure 3.2. The procedure includes the following:

- Sieve the representative soil through a number four sieve.
- The soil is wet at a selected molding water content and placed in three layers into a mold of given dimensions.
- Each layer is compacted by 25 blows of a 2.5 kg rammer dropped from a distance of 304.88 mm.
- The dry unit weight is determined.

This procedure is repeated for various molding water contents to determine the relationship between the dry unit weight and the molding water content for the soil (for Testing and Materials, 1992).



Figure 3.11: Standard proctor test procedure

### 3.5. Results

This section presents the results of the HHTT field test conducted at Maasvlakte 2.

#### 3.5.1. Cone penetration test

Depth influence

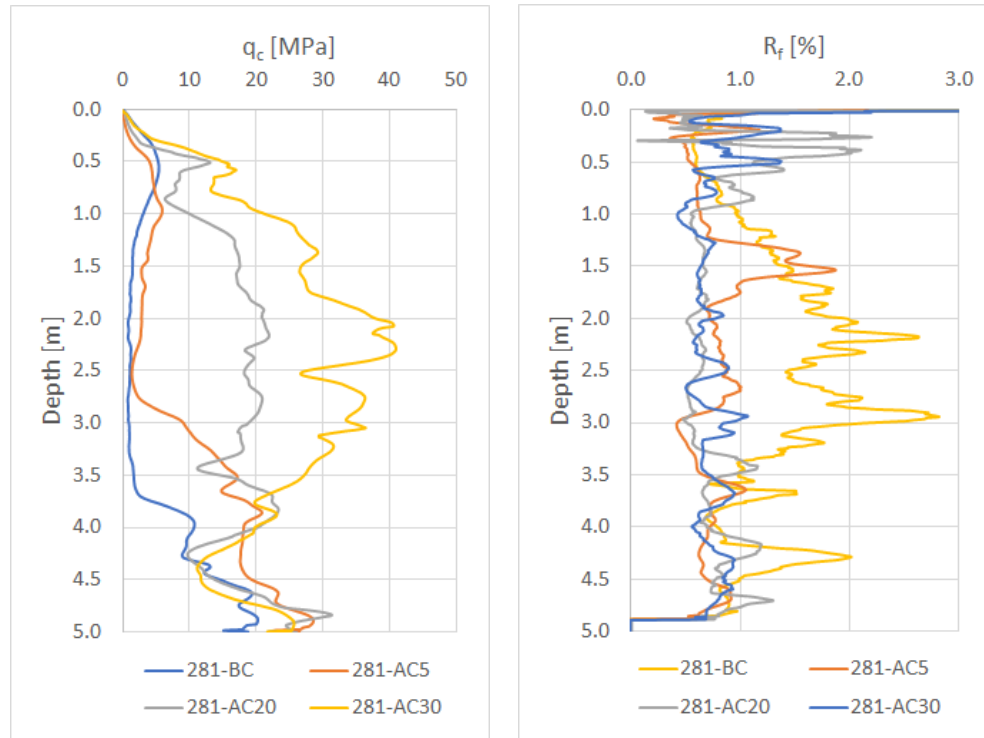


Figure 3.12: CPT 281

By comparing the results before compaction with the results obtained after compaction the following could be seen. Firstly, CPT 281 clearly shows an improvement in cone resistance with an increase in roller passes. This is depicted in Figure 3.12.

Secondly, the influence of the roller can be measured from 0.5 to 4 - 4.5 m depth.

It should also be noted that in the first 0.5 m of every CPT graph, the cone resistance after compaction is lower than before compaction. This is due to the loosening of the topsoil from the roller motion and due to the small pit that was excavated up to 0.5 m after each cycle of passes to perform the nuclear density and dynamic plate load tests.

Thirdly, before the compaction trial the soil at location 264, 270 and 284 was already dense. In order to meet the project requirements a minimum cone resistance of 10 MPa was needed. An overview of the cone resistance against the depth for previously mentioned CPT's are depicted below in Figure 3.13, Figure 3.14 and Figure 3.15. In these figures it can also be seen that there are sharp increases in cone resistance for example at 2.2 m depth for location 264. This most likely indicates a highly resistant material such as a rock (from the previous revetment).

Along with the friction ratio against the depth, also the relative density was plotted in these figures. By using the Baldi correlation, the relative densities at the locations could be determined. This correlation uses the following equation

$$D_r = \frac{1}{2.41} \ln \frac{q_c}{157\sigma_v^{0.55}} \quad (3.2)$$

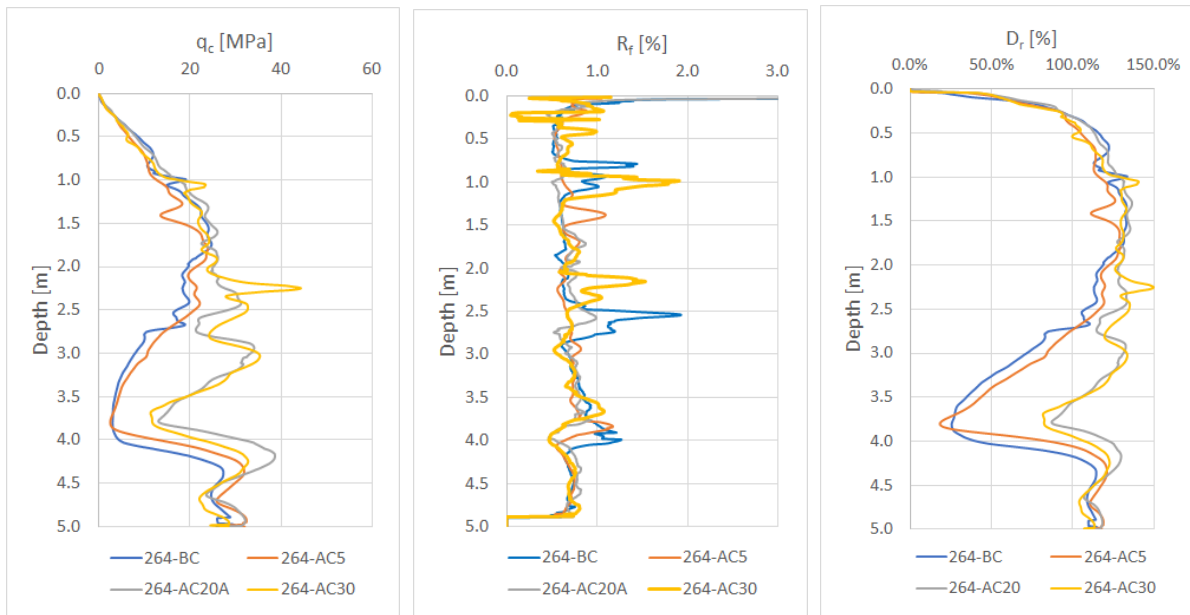


Figure 3.13: CPT 264

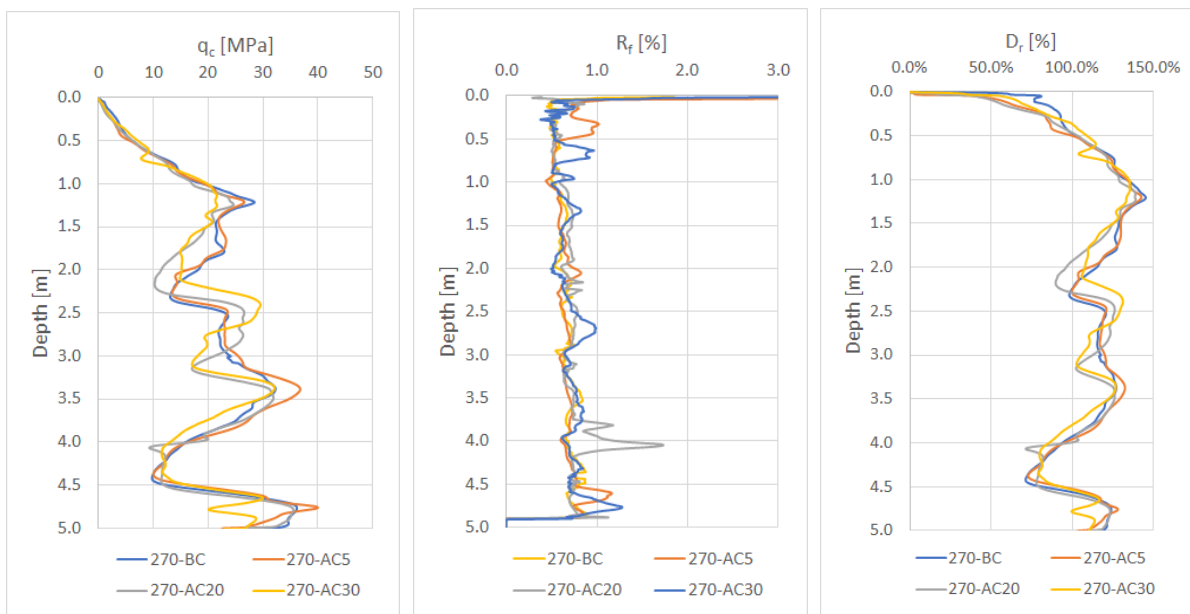


Figure 3.14: CPT 270

The dense state of the soil can be confirmed by the previous figures. As a result of this, these CPT's did not show the preferred results as for example in CPT 281.

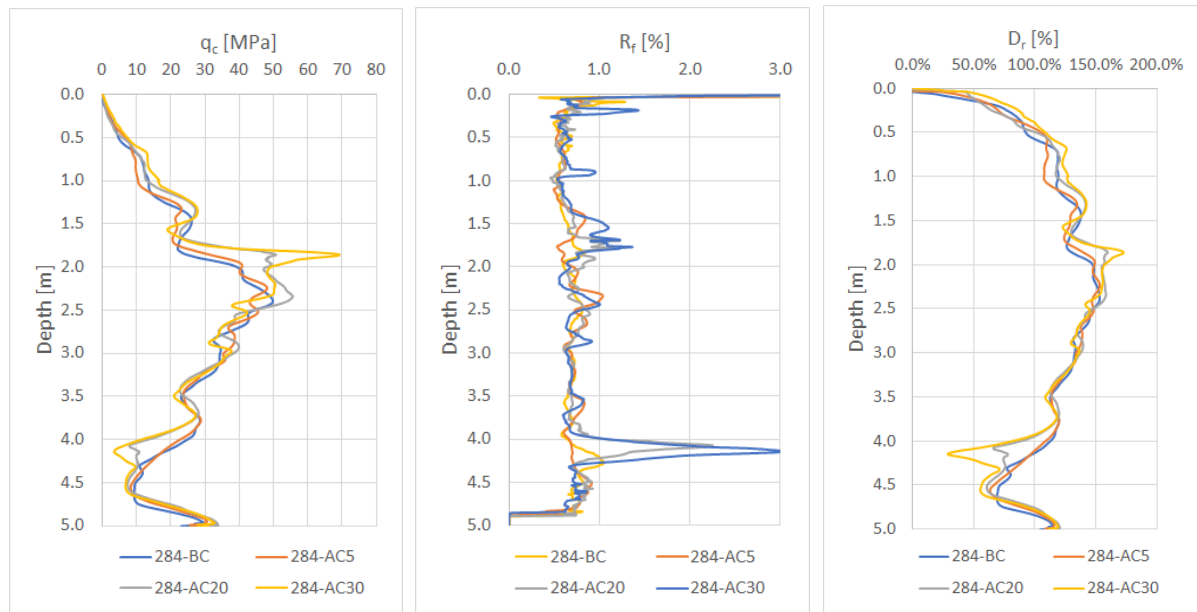


Figure 3.15: CPT 284

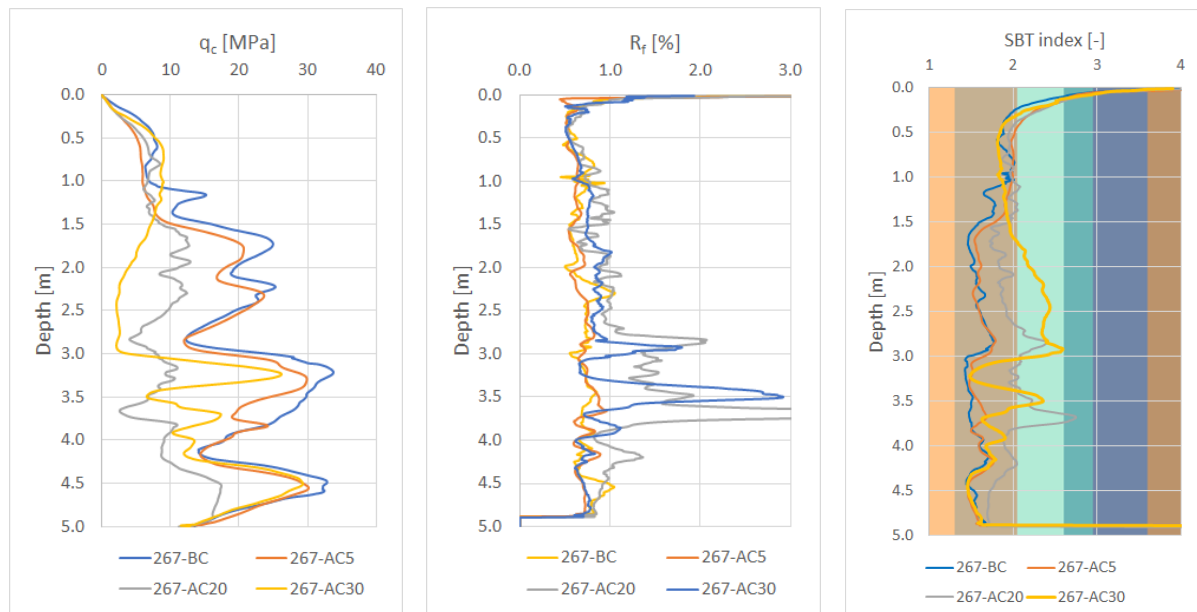


Figure 3.16: CPT 267

Lastly, CPT 267 shows very unfavourable results; depicting a decrease in cone resistance after each cycle of passes. Figure 3.17 classifies the soil according to the relation between the friction ratio and the normalized cone resistance. This classification was used to determine the soil behaviour after each cycle of passes and thus reason the decrease in cone resistance. This result could be due to the following reasons:

- AC5 was taken near the previous CPT's.
- AC20 and AC30 went through a layer of fines and/or silty sand as the friction ratio reaches up to 3%.

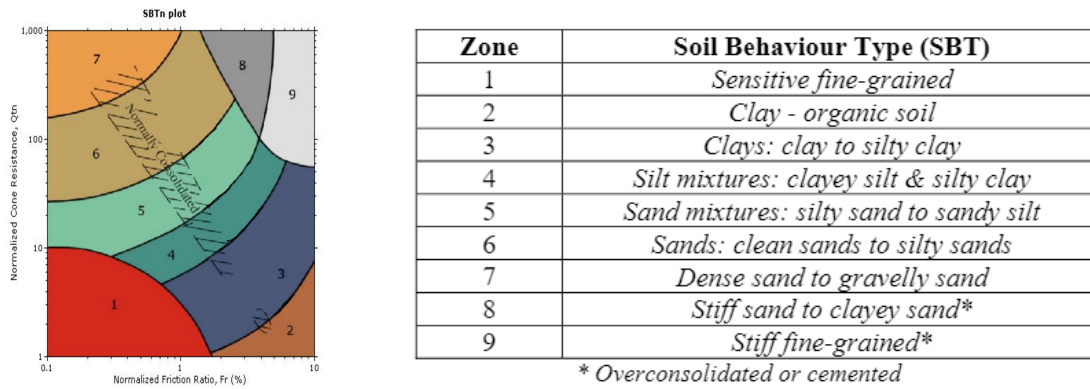


Figure 3.17: Robertson and Campanella, 1990

### Lateral influence

In order to determine the lateral extent of the roller several CPT's were performed next to the tracks where the roller had not been used. The table below shows an overview of these.

Table 3.3: Overview of CPT's (lateral influence)

BC	AC5	AC20	AC30
270 L3	264 L3	270 L1	270 L1
		270 L2	270 L2
		270 L3	270 L3
	267 L2		
	267 L3		
	270 L3		

Where L1, L2 and L3 are respectively at a distance of 0.5, 1 and 2 m from track 2. By comparing the CPT's taken at location 270 L3 for the different number in passes, no significant increase in cone resistance was noticed. The small differences in cone resistance might be due to natural soil variation.

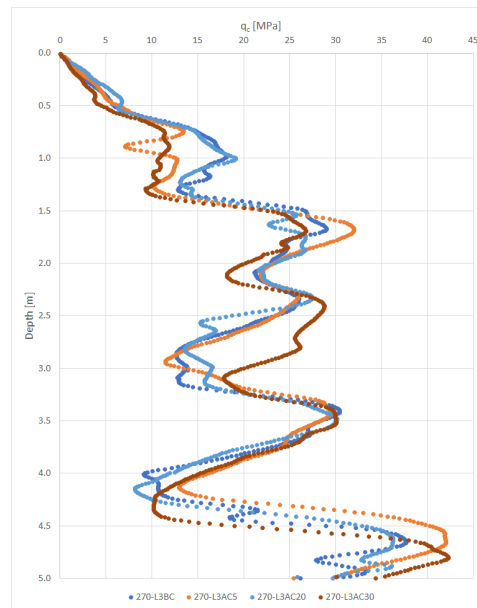


Figure 3.18: Lateral influence CPT 270 at L3

### 3.5.2. Dynamic plate load test

The results for the DPL tests, which were performed at 0.5 m depth, are given in Table 3.4. Considering the given time, some tests were performed 2 or 3 times in the pit. This leads to a more accurate overview of the dynamic modulus and it was averaged to depict the transition with increasing passes in Figure 3.19. The results show both favourable and unfavourable results with no clear relation to the previous tests. Considering that for example at location 267 an increase in dynamic modulus is noted, while from previous CPT and NDG results, the opposite was noted.

Table 3.4: Overview of DPL test results

Location	Dynamic modulus E <sub>vd</sub> [MPa]			
	BC	AC5	AC20	AC30
1	49.45	31.87 32.1		
2	35.49	39.61 37.75		
264		46.78	41.59 42.13 43.35	37.44 46.39
267		31.47	35.49	44.38 42.61
270		37.07	38.86 39.89	41.67
281		40.83	33.28 34.62	29.15 27.92

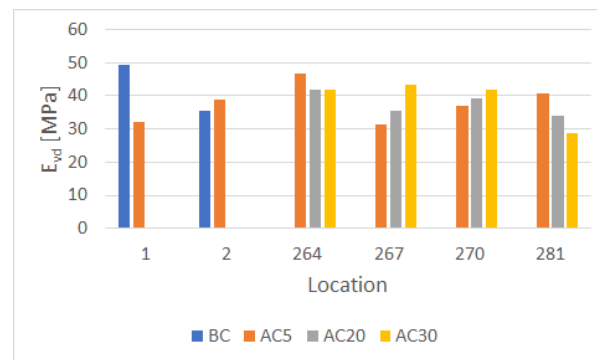


Figure 3.19: Overview of DPL test results (averaged)

### 3.5.3. Nuclear density gauge- and Standard proctor test

Table 3.5 provides an overview of the NDG results compared to the Proctor results. These NDG tests were performed at 0.5 m depth.

Table 3.5: NDG results overview compared to Proctor results

Location	# of passes	In situ density [kg/m <sup>3</sup> ]	Moisture content [%]	Dry density [kg/m <sup>3</sup> ]	Proctor density [kg/m <sup>3</sup> ]	Optimal moisture content [%]	Compaction grade [%]
1	BC	1777	8.4	1639	1653	16	99
	AC5	1760	7.2	1642			104
2	BC	1817	9.9	1653	1633	16	101
	AC5	1834	7.8	1701			104
264	AC5	1832	13.3	1617	1656	14.5	98
	AC20	1855	8.8	1705			103
	AC30	1828	6.6	1715			104
267	AC5	1900	7.4	1769	1666	14.5	106
	AC20	1804	6.2	1699			102
	AC30	1837	8	1701			102
270	AC5	1850	8.6	1703	1649	16	103
	AC20	1816	8.4	1675			102
	AC30	1857	8	1719			104
281	AC5	1816	6.7	1702	1652	14.5	103
	AC20	1879	7.4	1750			106
	AC30	1797	6.4	1689			102

From the results above it can be seen that the dry density increases with increasing passes at all locations with exception of locations 267, 270 and 281. This can be related to the previously depicted CPT results, where location 267 already showed unfavourable results. However, for location 281 this is unexpected considering the increase in cone resistance obtained from the CPT's. It should be noted that the proctor samples and NDG testing were done at 0.5 m depth and is very location specific. The table also shows that the moisture content is lower than the optimal moisture content, but the corresponding dry density is reached.

The roller thus uses a higher compactive effort, which relates to a decrease in optimal moisture content. By looking at the figure below, a fitting proctor curve would thus be more on the left side.

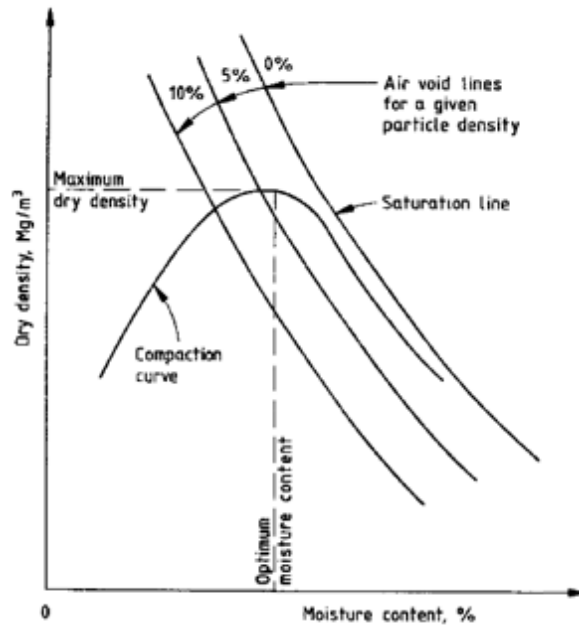


Figure 3.20: Influence of compactive effort on compaction (flatGEO Consulting Company Limited)(after BS 1377 : 1990 - Part 4)

### 3.5.4. Vibration monitoring

The following figures depict respectively the vibration velocity and acceleration as a function of the distance from the centre of the roller to the vibration monitor. This decay which can be approximated to a power trendline is expected and shows that the largest vibrations can be measured up to 2 meter next to the source.

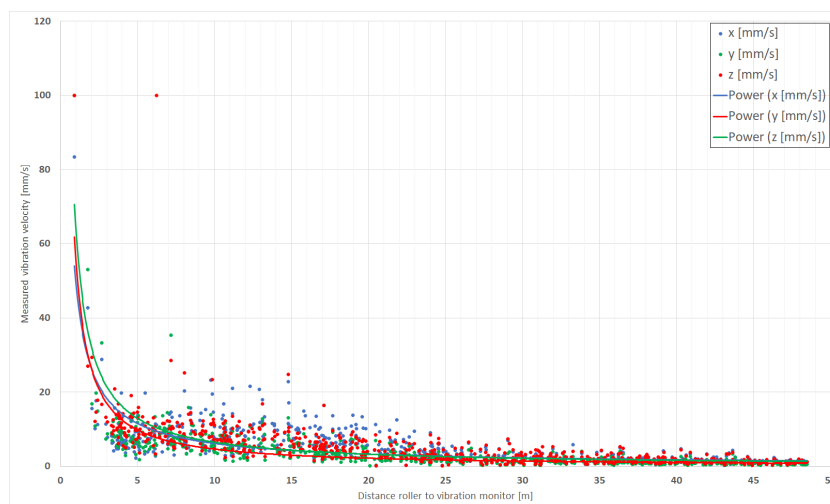


Figure 3.21: Vibration velocity as a function of the distance between the roller and the vibration monitor

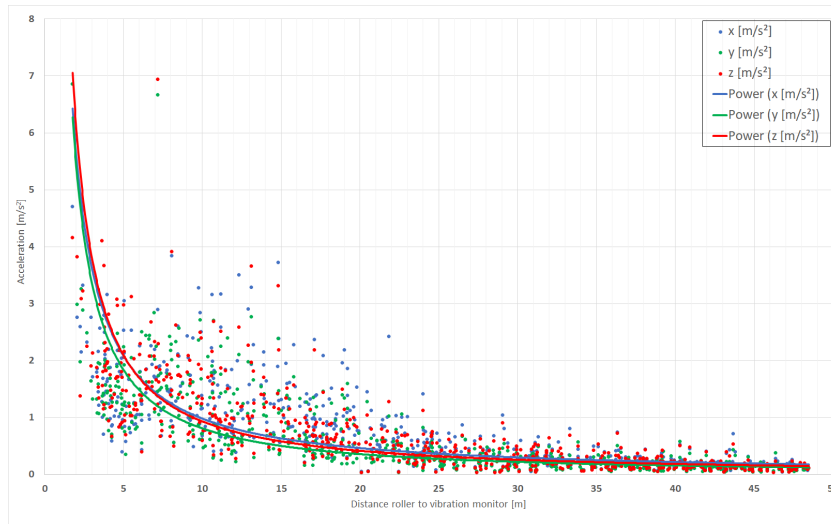


Figure 3.22: Vibration acceleration as a function of the distance between the roller and the vibration monitor

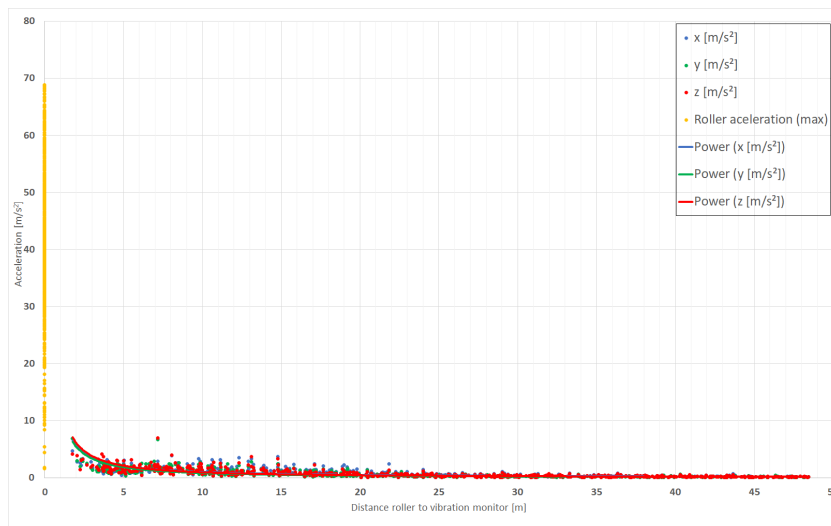


Figure 3.23: Measured vibration acceleration and corresponding roller acceleration



# 4

## Correlations

In this chapter correlations are derived based on the peak acceleration values and the field test measurements in section 4.1. This is also determined for the integrated peak velocity and the field test measurements in section 4.2. Each of these is performed for four cases with each four field test measurements. For each case the correlation was made with four field test measurements namely in situ density, dry density, dynamic modulus and the average cone resistance.

### 4.1. Peak acceleration

The four cases include the mean peak acceleration of each cycle, the maximum peak acceleration of each cycle, the peak acceleration at the last pass of each cycle and the mean peak acceleration at the last pass of each cycle. Only the correlation graphs for the case of the maximum peak acceleration per cycle are given in this section. The other three cases are depicted in Appendix A.1.1, Appendix A.1.2 and Appendix A.1.3.

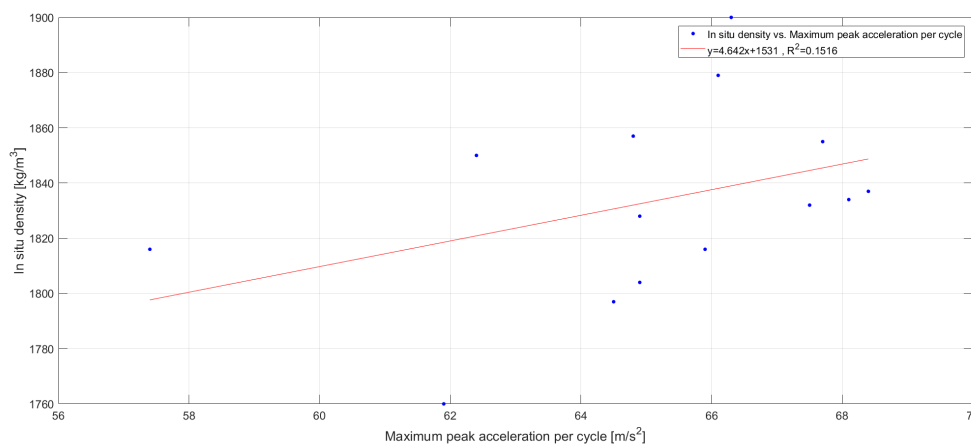


Figure 4.1: In situ density vs. Maximum peak acceleration per cycle

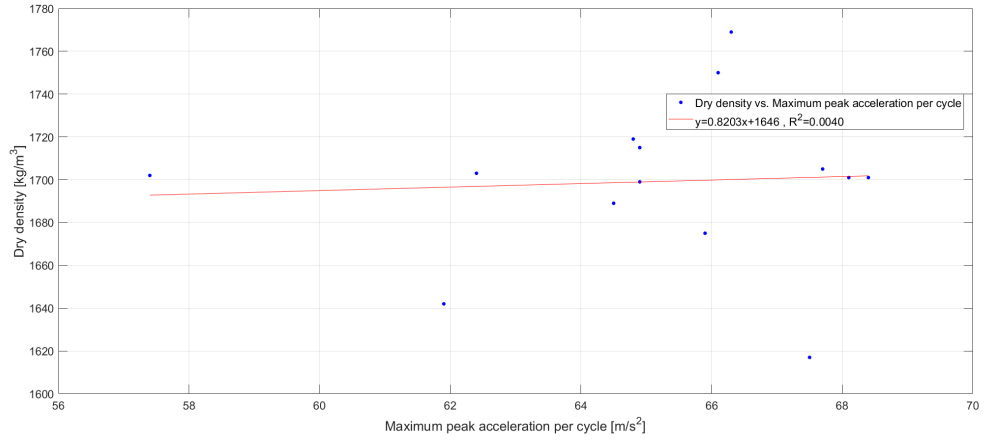


Figure 4.2: Dry density vs. Maximum peak acceleration per cycle

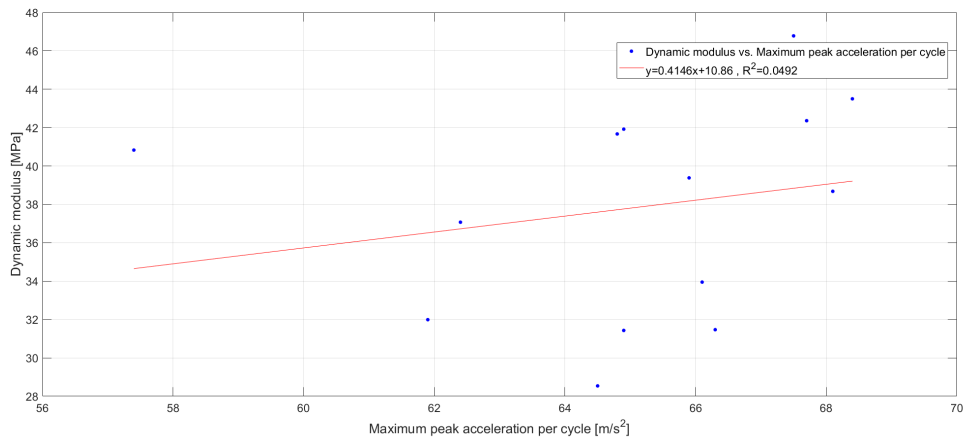


Figure 4.3: Dynamic modulus vs. Maximum peak acceleration per cycle

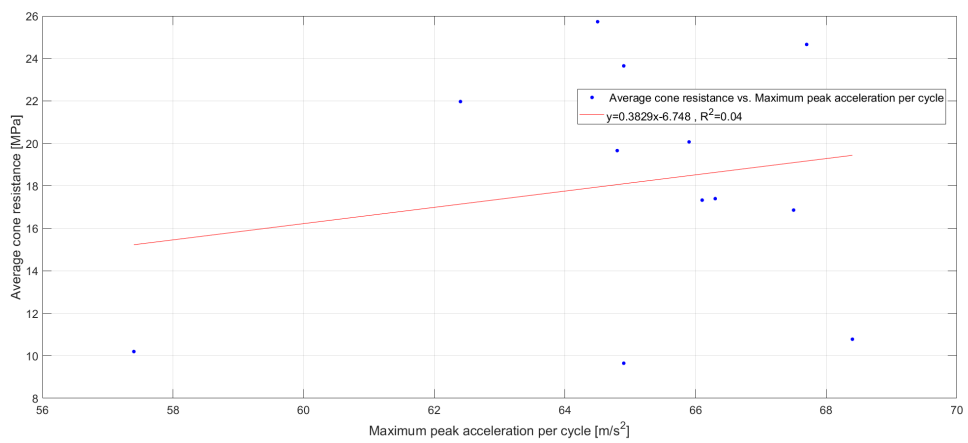


Figure 4.4: Average cone resistance vs. Maximum peak acceleration per cycle

## 4.2. Integrated peak velocities

Considering that velocity is directly related to the imparted energy, these correlations were also made for the integrated peak velocity to see if this would give a better correlation than the peak acceleration.

The four cases include the mean integrated peak velocity of each cycle, the maximum integrated peak velocity of each cycle, the integrated peak velocity at the last pass of each cycle and the mean integrated peak velocity at the last pass of each cycle. Only the correlation graphs for the case of the maximum integrated peak velocity per cycle are given in this section. The other three cases are depicted in Appendix A.2.1, Appendix A.2.2 and Appendix A.2.3.

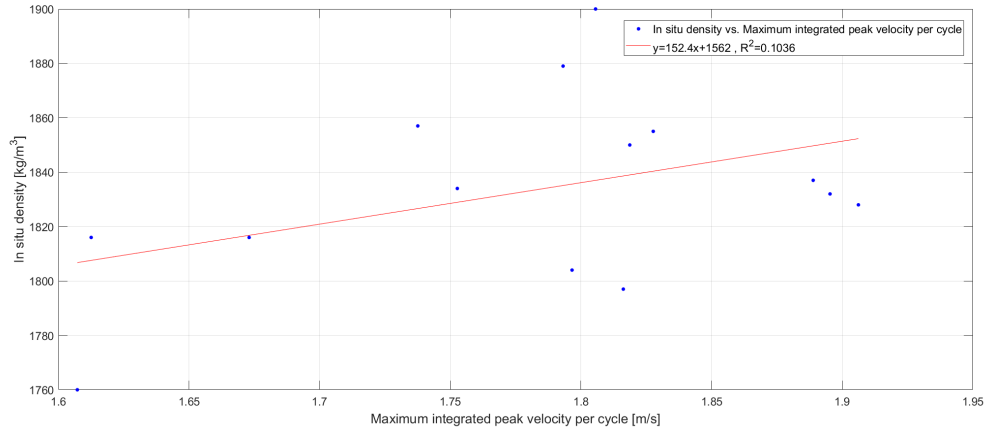


Figure 4.5: In situ density vs. Maximum integrated peak velocity per cycle

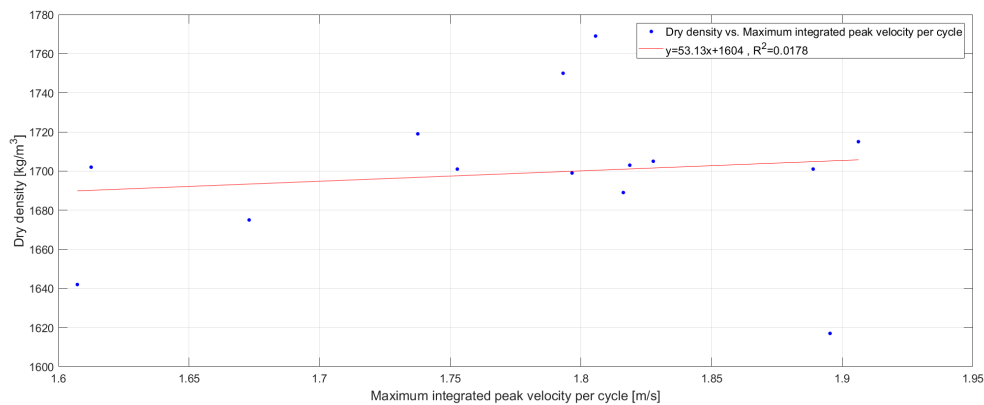


Figure 4.6: Dry density vs. Maximum integrated peak velocity per cycle

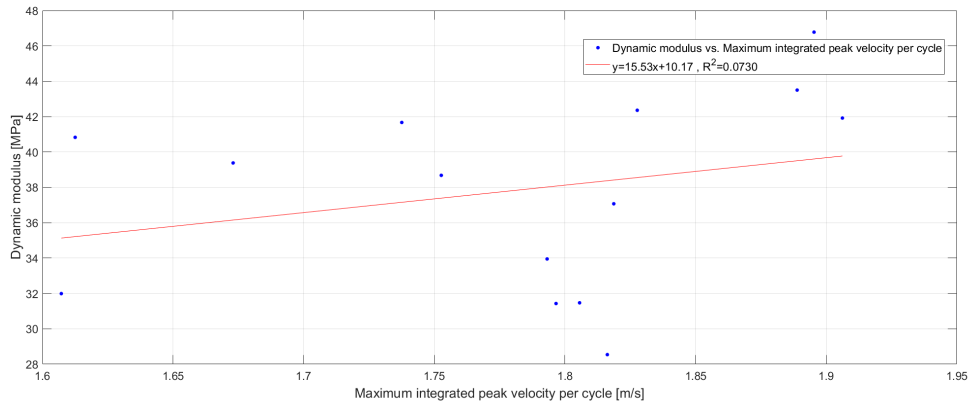


Figure 4.7: Dynamic modulus vs. Maximum integrated peak velocity per cycle

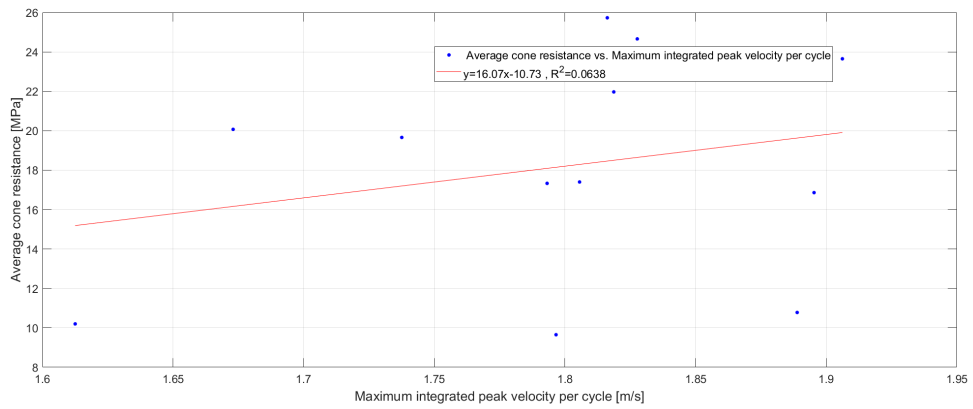


Figure 4.8: Average cone resistance vs. Maximum integrated peak velocity per cycle

# 5

## Response of the roller

In this chapter the response of the roller is analysed in terms of the measured acceleration signals. The first section 5.1 describes the method of acceleration signal processing. The corrected acceleration signals are then double numerically integrated in section 5.2 to obtain the displacement response of the roller.

### 5.1. Signal processing

The accelerometer used during the field test is the Ellipse A2 8g accelerometer given in Figure 5.1. It is located on the centre of the axis of the drum, which is depicted in Figure 5.2.



Figure 5.1: Ellipse A2 8g accelerometer(systems, 2018)



Figure 5.2: Accelerometer location on the centre of the drum axis

The field test defined 6 test locations and corresponding to the GPS data, the following acceleration signals given in Figure 5.3 were obtained.

The acceleration data is recorded as continuous time functions and when digitizing continuous data, certain restrictions need to be placed e.g. the length of the data window and the sampling rate (Rogers et al., 1997).

Cofra obtains 100 samples at 100 Hz to generate the acceleration pulse per impact, leading to a sampling interval of 0.01 s. This sampling interval should be chosen corresponding to the data of interest, because it determines the Nyquist frequency, which is the highest frequency component that can be properly reconstructed in spectral calculations (Rogers et al., 1997). Before sampling, the accelerometer uses an advanced anti-aliasing FIR filter in order to prevent the signals to become indistinguishable when sampled.

With a given 100 samples per impact, the observed time window is 1 s, leading to a lowest frequency of 1 Hz.

Given that displacement is to be quantified from the double numerical integration of the acceleration-time signals, the following was implemented in the code (Tsouvalas, 2019):

- Detrending of the data

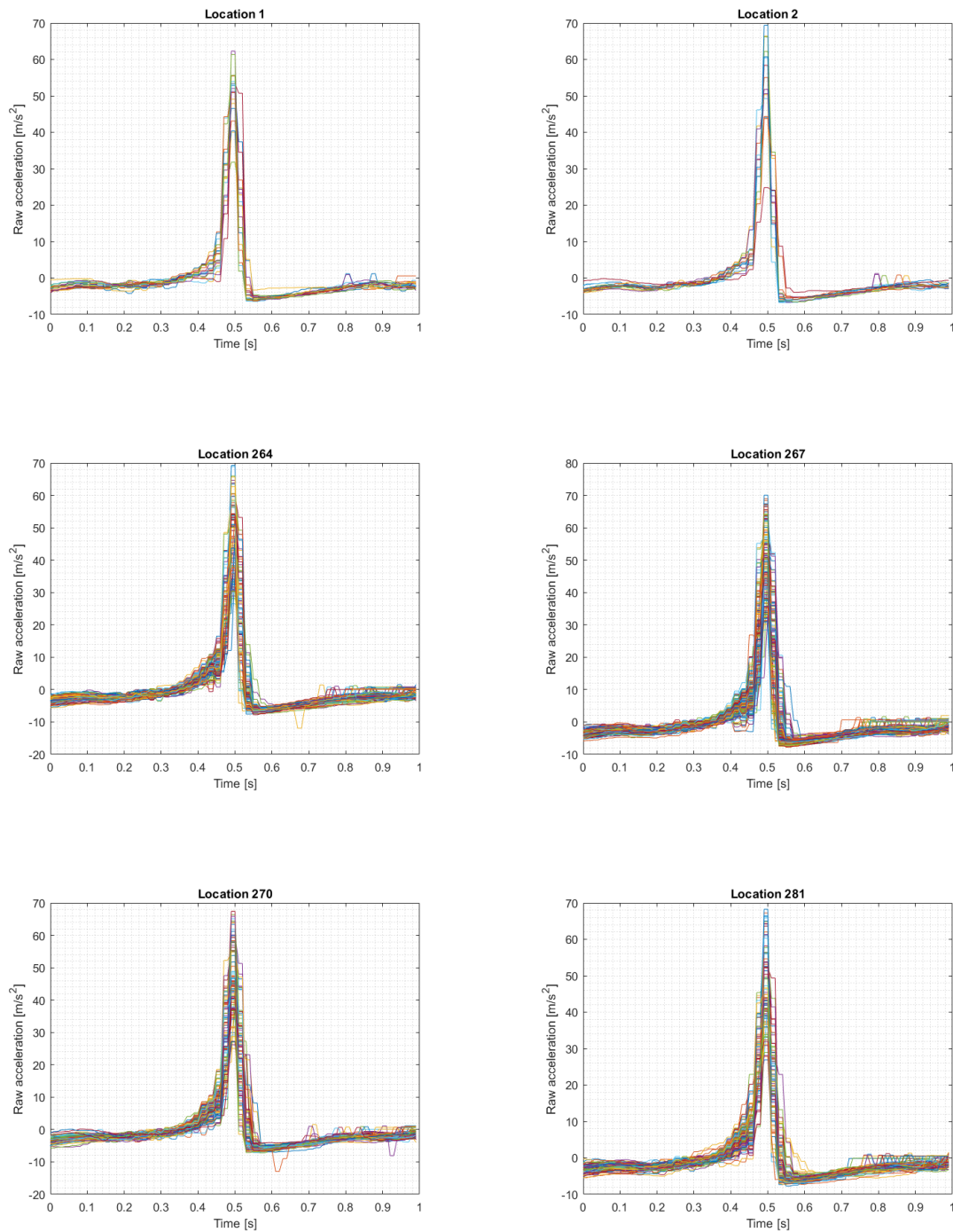


Figure 5.3: Overview of raw accelerations signals per location

- Acausality
- Butterworth filter
- Trapezoidal rule as numerical integration method

Before filtering the data, the mean of each signal was subtracted in order to detrend the data and prevent phase shifting of the signal. The Fourier spectra of these signals were obtained to define the proper cut-off frequency. These are depicted in Figure 5.4.

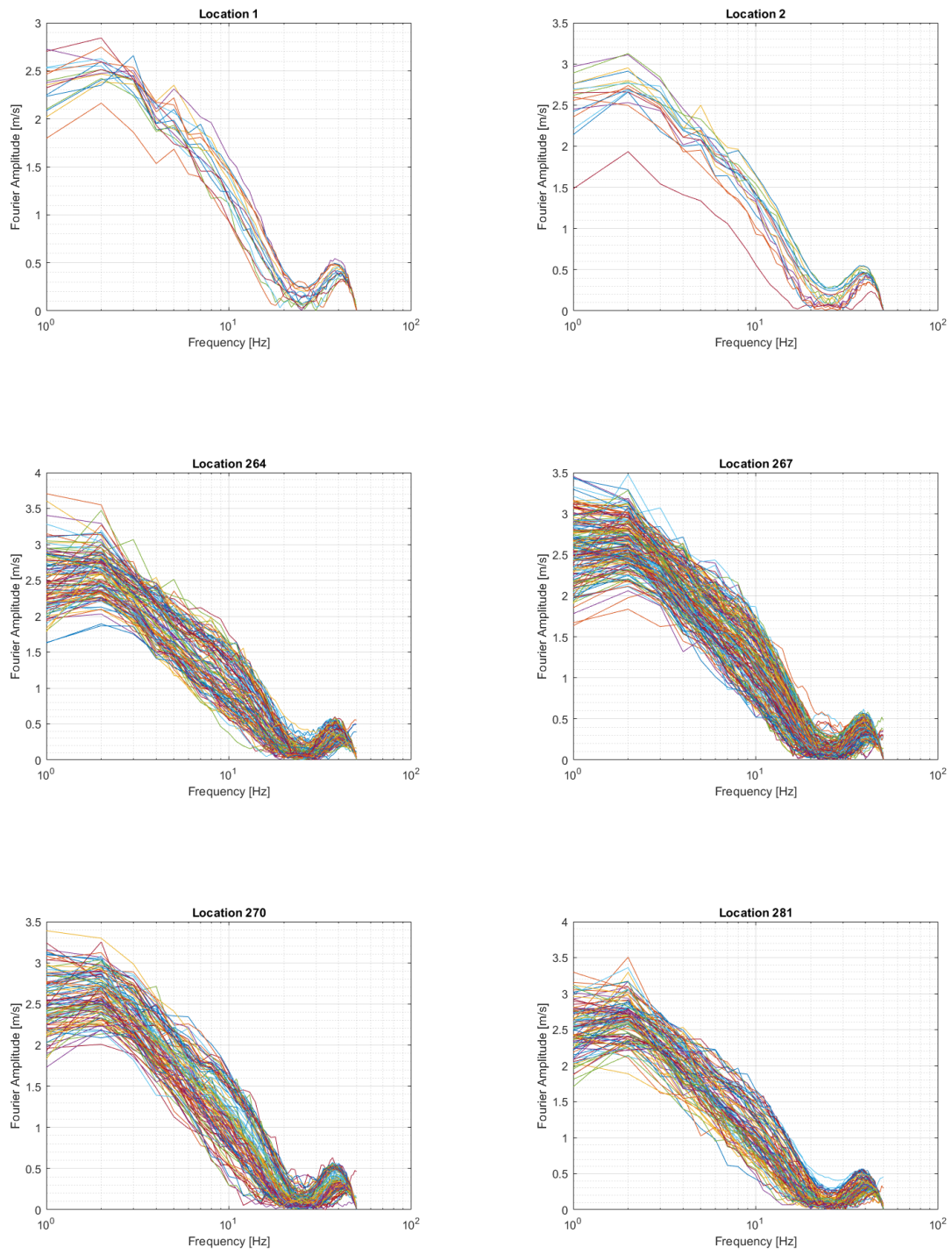


Figure 5.4: Overview of Fourier spectra per location

An acausal filter was chosen, considering that a causal filter had almost no effect on the corrected signal and acausal filtering eliminates the delay. A butterworth filter with order 6 was chosen based on the steepness of the curves. The higher the filter order, the more abrupt the cut-off.

The identification of the cut-off frequencies plays a big role in obtaining a correct displacement response from the acceleration signal. The upper limit of the frequencies depend on the accelerometer specifications and the sampling rate, while the lower limit depends on the observed time window (Tsouvalas, 2019).

The accelerometer has a bandwidth of 390 Hz and a sampling rate of 4 kHz. The acceleration data is processed by Cofra with a sampling rate of 100 Hz. The highest frequency component that can properly be reconstructed is thus, according to the Nyquist rule, 50 Hz.

The observed time window per impact is 1 s, leading to a lowest frequency of 1 Hz.

However, from the raw acceleration signals given in Figure 5.3 can be seen that the acceleration starts at a non-zero value. This non-zero value can be removed by removing the lower frequencies.

Filtering is subjective and in this case with the filtering is focused on conserving the peak acceleration, removing the non-zero start value of the acceleration and most importantly, deriving the correct displacement response. The examples shown are applied to the acceleration signal after 1 pass at location 270.

In figure 5.5 the unfiltered vs. filtered acceleration signal is depicted, where the filtered signal was cut-off at 28 Hz. It can be observed that by applying a cut-off frequency of 28 Hz, the peak acceleration is higher and the pulse is more smooth compared to the unfiltered signal. Hence, the cut-off frequency of 28 Hz was chosen.

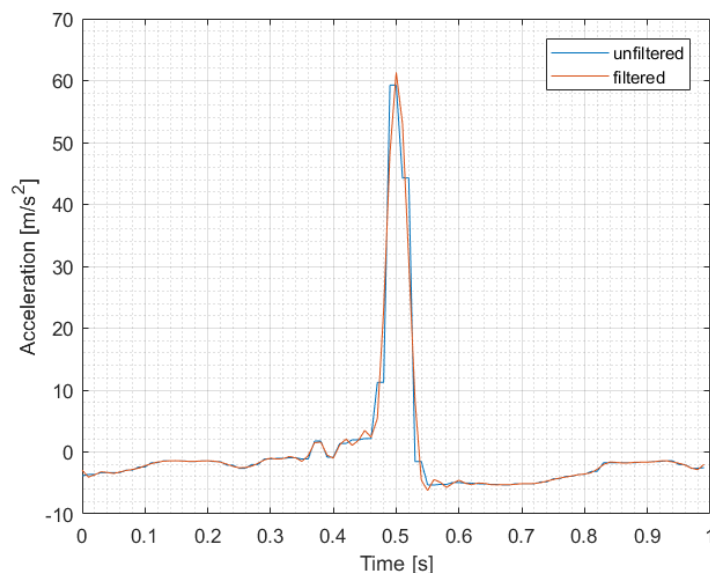


Figure 5.5: Unfiltered vs. filtered acceleration signal with a cut-off frequency of 28 Hz

Figures 5.6, 5.7 and 5.8 show the effect of removing the lower frequencies. By comparing these figures it can be seen that the peak acceleration reduces more when applying a cut-off frequency of 4 Hz compared to 2 Hz, while maintaining the same initial acceleration. However, Figure 5.8 shows the curve approaching zero in the beginning and the end of the impact.

Hence, the corresponding displacement response for lower cut-off frequencies should be analyzed as well. The corresponding displacement response for a cut-off frequency of 1 Hz and 2 Hz are given in figures 5.9 and 5.10.

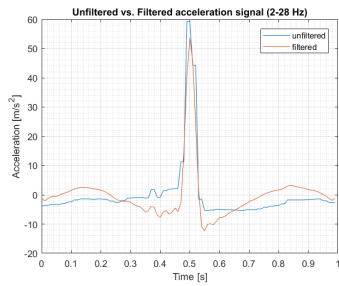


Figure 5.6: Unfiltered vs. filtered acceleration signal of 2 to 28 Hz

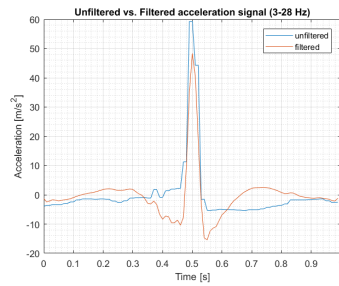


Figure 5.7: Unfiltered vs. filtered acceleration signal of 3 to 28 Hz

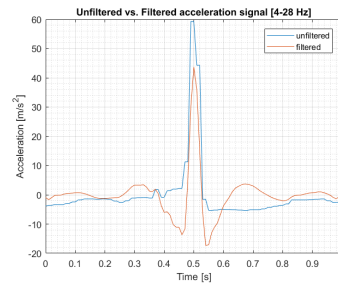


Figure 5.8: Unfiltered vs. filtered acceleration signal of 4 to 28 Hz

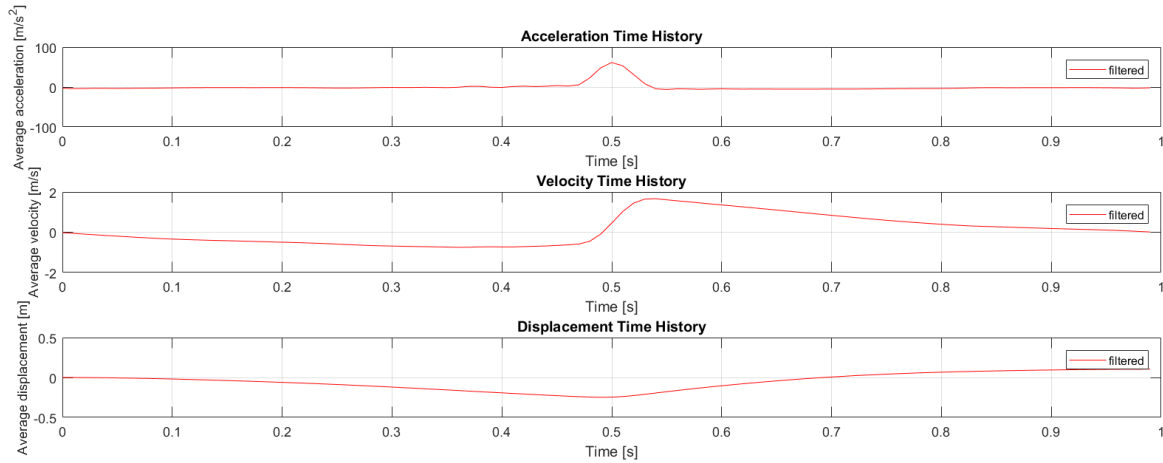


Figure 5.9: Displacement response with a bandwidth of 1 to 28 Hz

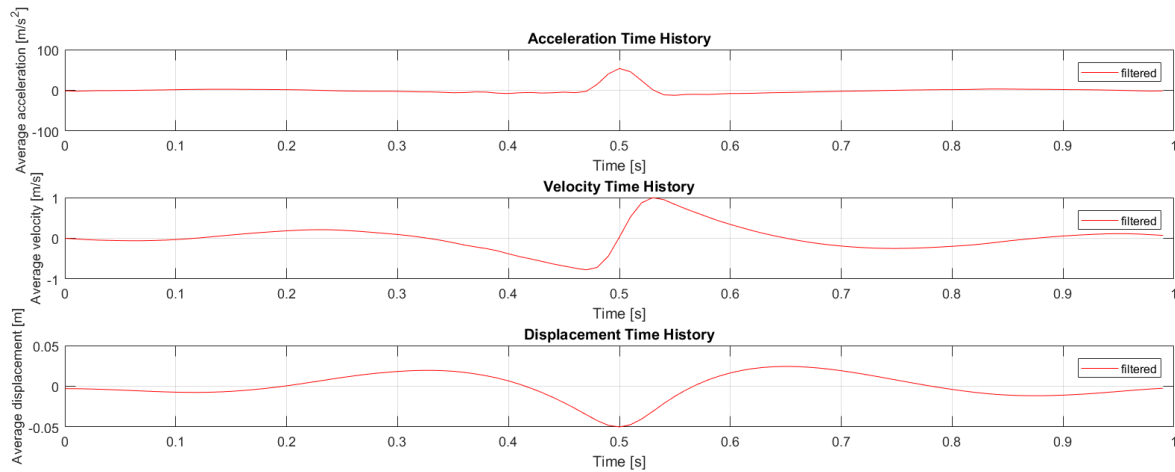


Figure 5.10: Displacement response with a bandwidth of 2 to 28 Hz

It can be observed that both figures do not show the expected displacement response, where after the impact the displacement increases slightly until residual settlement in the form of plastic deformation is obtained. By removing low frequencies, the peak acceleration decreases, but the initial acceleration approaches zero. However by not removing low frequencies, the peak acceleration is conserved, but the initial acceleration is non-zero. It should also be noted that within this observation window of 1 s, only one impact is measured. Therefore with an excitation frequency of 1 Hz, valuable information can be lost by removing the lower frequencies. Therefore it was decided to conserve the peak acceleration and try out other methods to correct

the start acceleration. Filtering in the form of a low-pass Butterworth filter with a cut-off frequency of 28 Hz was applied to the remaining acceleration signals.

The filtering was applied to the mean of the acceleration signals for each cycle per location. These cycles include 5, 20 and 30 passes. In this way the transition for each location could be clearly distinguished with three representative mean signals from each cycle.

In order to represent the acceleration signals in the frequency domain, the Fourier transform was applied. The Fourier spectrum of these mean acceleration signals is depicted in Figure 5.11. The frequency bandwidth is then identified where the signal-to-noise ratio is adequately high. After applying a low-pass filter with a cut-off frequency of 28 Hz, the filtered Fourier spectrum of each mean acceleration signal could be determined. The filtered Fourier spectrum of the mean acceleration signal of all locations is given in figure 5.12.

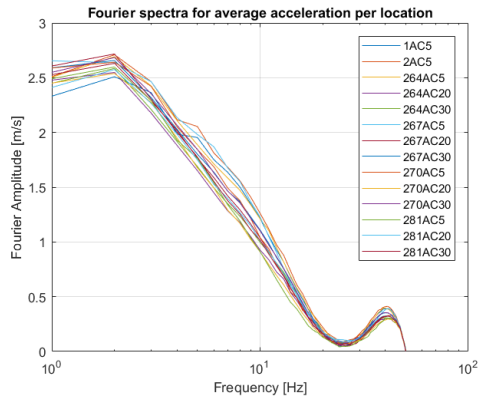


Figure 5.11: Fourier spectra of mean acceleration signals

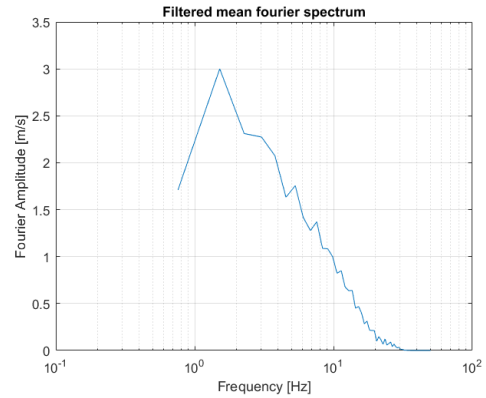


Figure 5.12: Filtered Fourier spectrum of mean acceleration signals

## 5.2. Displacement response of the roller

### 5.2.1. Original displacement response

The displacement response of the roller, which is depicted in Figure 5.13, is obtained by double numerical integration of the filtered acceleration signal. The trapezoidal rule is used as numerical integration method.

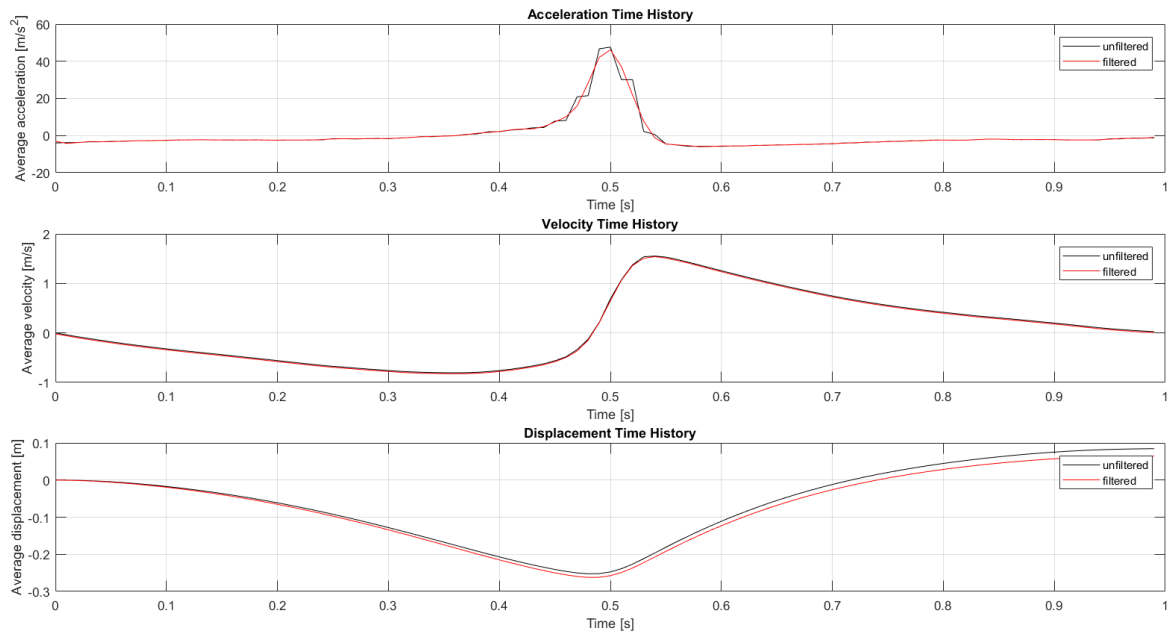


Figure 5.13: Displacement response of the roller after 5 passes at location 270

### 5.2.2. Verification of numerical integration method

In order to verify the double numerical integration, the obtained displacement-time signal was double differentiated and plotted against the filtered acceleration-time signal. This was applied to the mean displacement response after 5 passes at location 270, given in Figure 5.14.

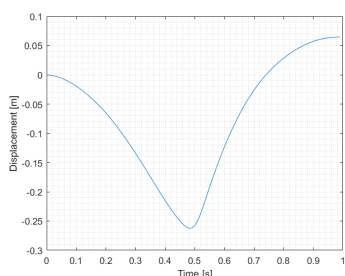


Figure 5.14: Integrated displacement response of the roller

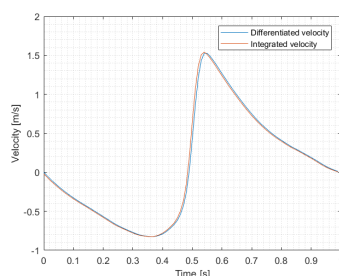


Figure 5.15: Differentiated velocity vs. integrated velocity

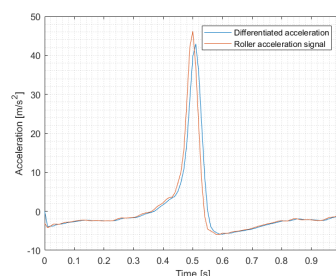


Figure 5.16: Differentiated acceleration vs. roller acceleration signal

From Figure 5.16 can be seen that the original form of the acceleration pulse is conserved. However, the differentiated acceleration is shifted by 0.01 s and the peak is reduced by 3 m/s<sup>2</sup>.

### 5.2.3. Correction based on non-deformable surface

Considering that the drum of the roller is non-circular, the centre of the axis will also move when rolling as opposed to the movement of a circular drum. Therefore the expected roller movement was determined over a non-deformable surface and the corresponding acceleration was subtracted from the raw acceleration signals. This movement is depicted in Figure 5.17, where the dropheight before each impact is 0.23 m.

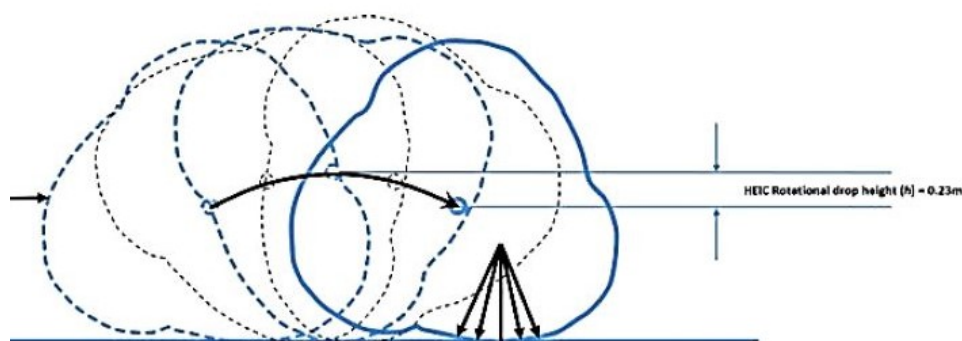


Figure 5.17: Dropheight of the roller (Kelly)

By determining the angular velocity with equation 5.1, where  $v$  is the average tractor velocity of 3.43 m/s and  $r$  is the roller radius of 2.07 m, the time for one revolution could be determined.

$$\omega = \frac{v}{r} \quad (5.1)$$

During one revolution the roller hits the surface three times, leading to a time of 0.63 s for each impact. By substituting this value and the dropheight into equation 5.2, an acceleration of 1.15 m/s<sup>2</sup> was obtained.

$$y(t) = \frac{1}{2}at^2 \quad (5.2)$$

By applying the same numerical integration method as before, the displacement response given in Figure B.15 was obtained.

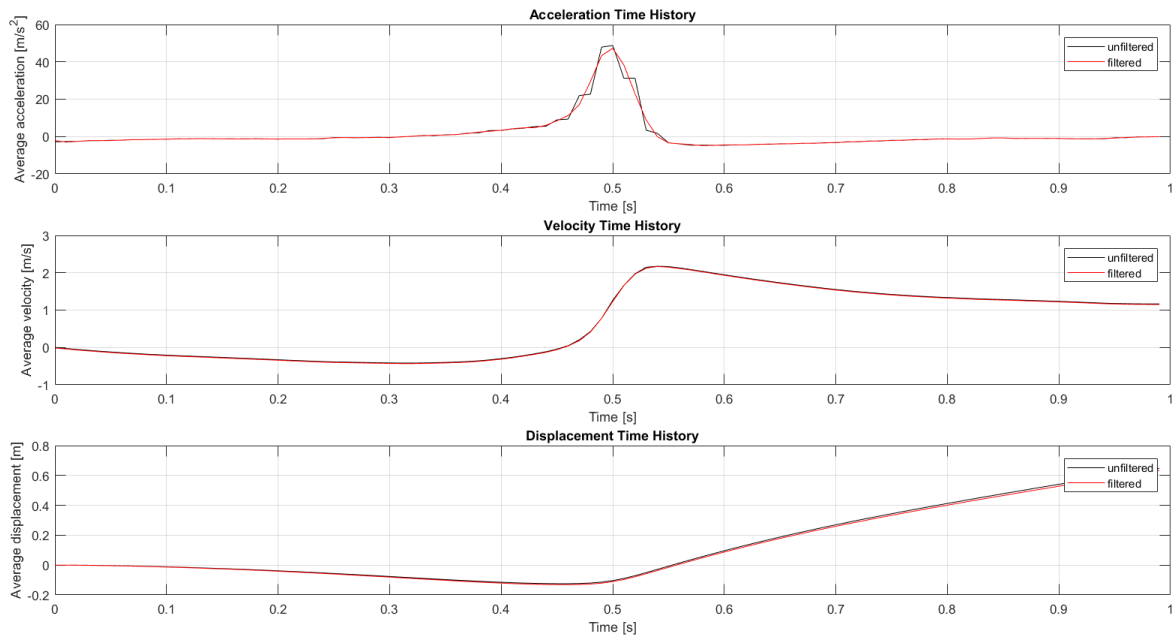


Figure 5.18: Displacement response of the roller after 5 passes at location 270

However, a steep increase in displacement is noticed after the impact. This corresponds with the non-zero value of the velocity at the end of the impact. This velocity increase is divided over the given time period of 0.99 s. Subsequently the acceleration signal is corrected by subtracting that value over the whole signal. After application of double numerical integration, the corrected displacement response given in Figure 5.20 was obtained.

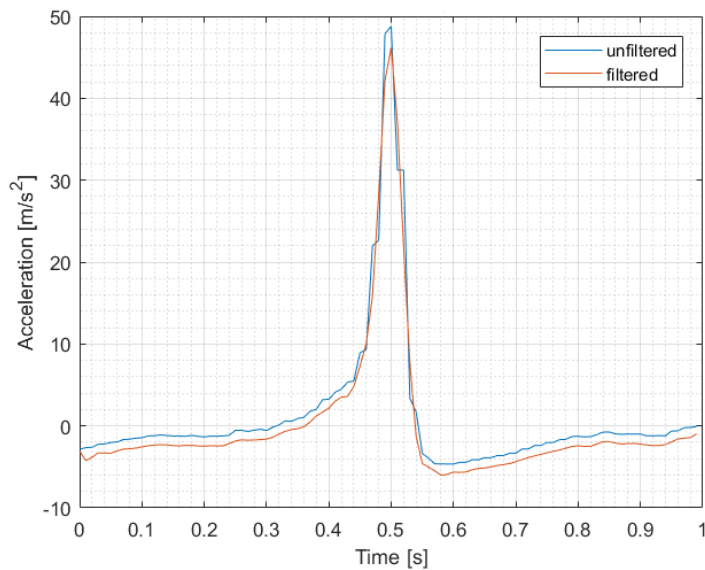


Figure 5.19: Unfiltered vs. Filtered mean acceleration signal after 5 passes at location 270

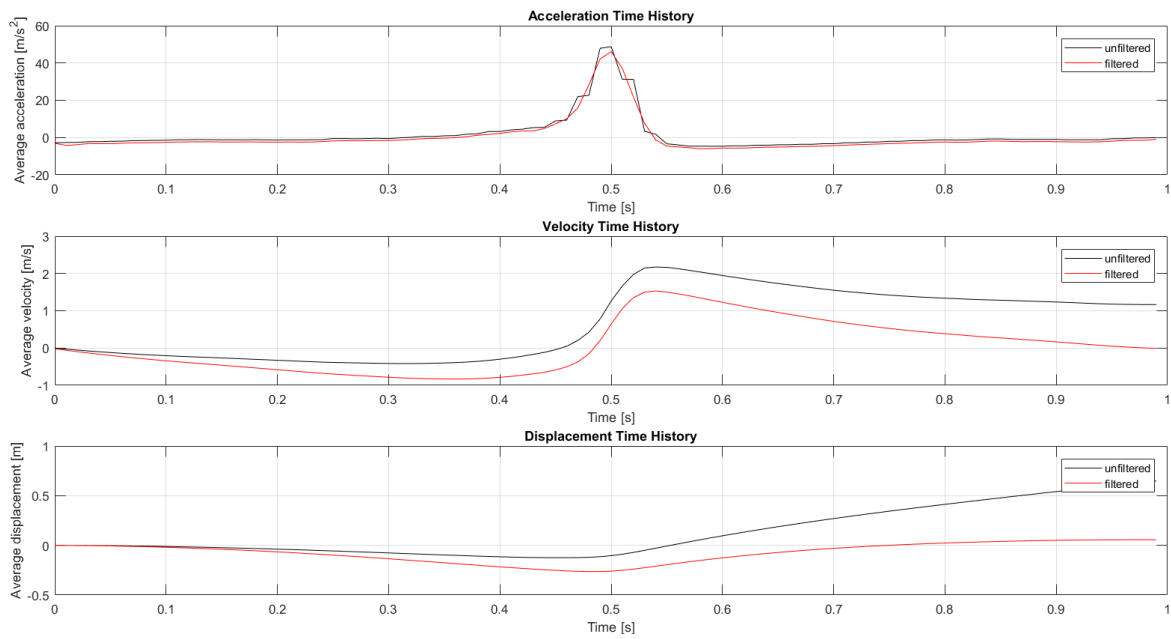


Figure 5.20: Corrected displacement response of the roller after 5 passes at location 270

This displacement response matches the original displacement response, considering that the subtraction of the velocity difference divided by the timeperiod, equals the initial subtraction of the acceleration signal due to the non-deformable surface, namely 1.15 m/s<sup>2</sup>.

### 5.2.4. Correction based on accelerometer in rest state

The acceleration signals contain a pulse which starts at a non-zero value. Before the roller impacts the ground, the acceleration would have to be zero at a rest state. In order to compensate for these non-zero values, a correction is applied on the acceleration signals. Namely the maximum non-zero value of acceleration before the impact is subtracted from the whole acceleration signal. By applying the same numerical integration method as before, the displacement response given in Figure 5.21 was determined.

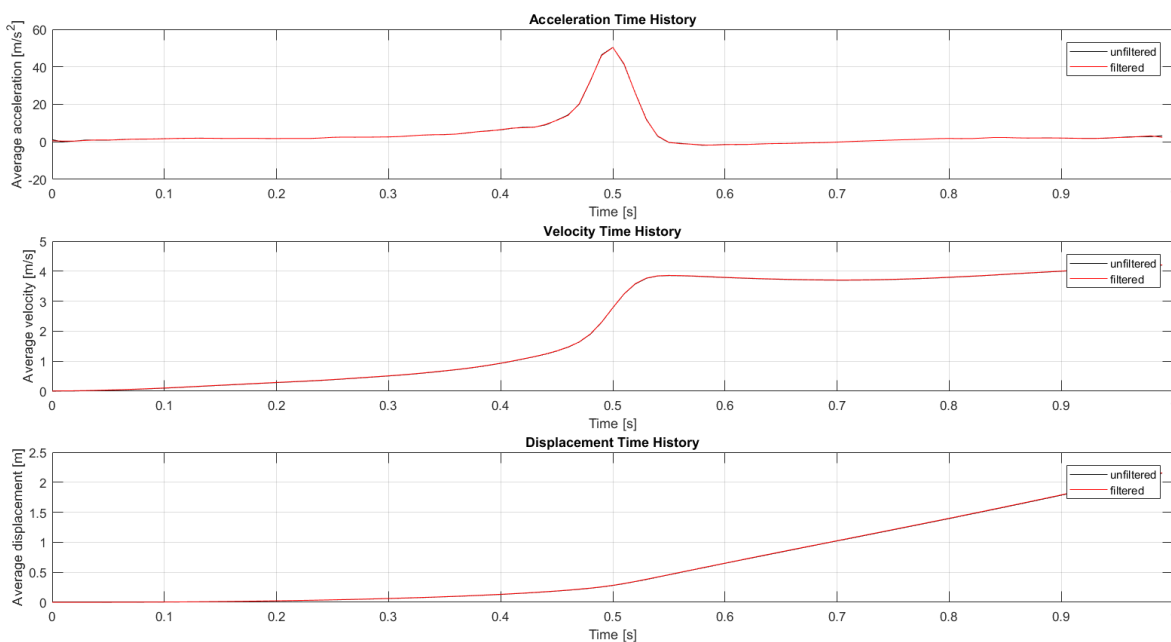


Figure 5.21: Displacement response of the roller after 5 passes at location 270

In comparison to the previous section, the displacement response also contains a steep increase, but more steep. Hereafter, the same method of correcting the acceleration signal was applied, leading to figures 5.22 and 5.23.

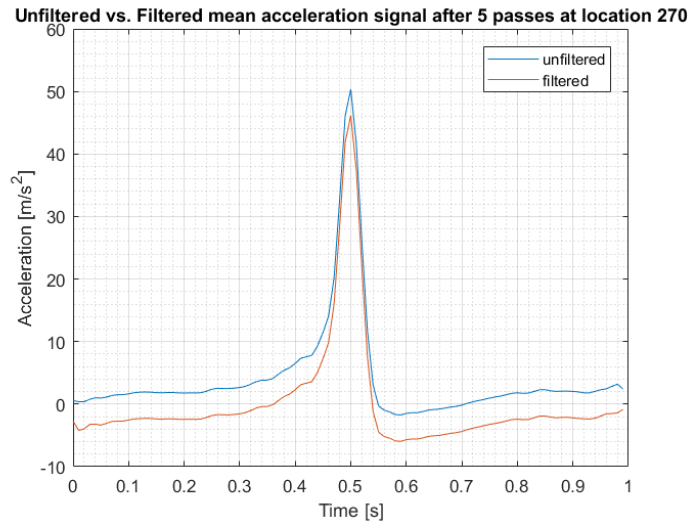


Figure 5.22: Unfiltered vs. Filtered mean acceleration signal after 5 passes at location 270

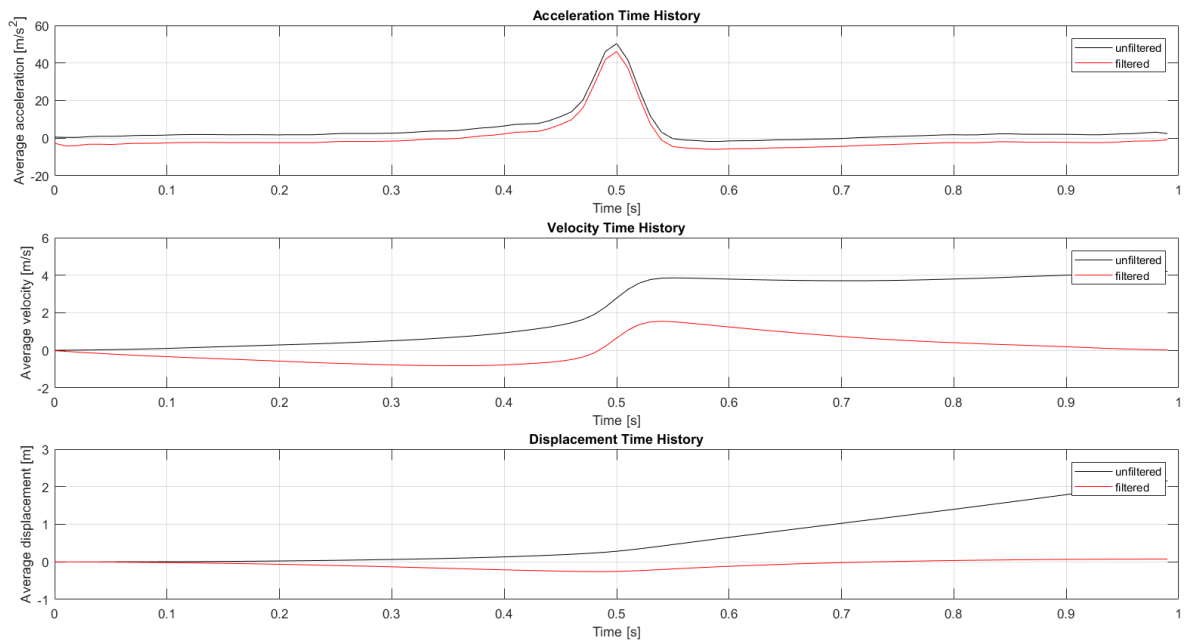


Figure 5.23: Corrected displacement response of the roller after 5 passes at location 270

# 6

## DPL-Soil model

In this chapter the DPL-Soil model is described, which functions as step 1 for obtaining the Roller-Soil model. The setup of the model is described in section 6.1, followed by the results in section 6.2.

### 6.1. Model setup

In developing this model a substructure technique is used, where the two systems namely the dynamic plate load test and the soil are first treated separately and hereafter the systems are coupled.

#### 6.1.1. DPL

When using the DPL, an impact-like load is applied to the subsoil via a rigid circular steel plate. The falling weight slides down approximately 0.7 m along the guide rod and hits a spring-damper element. Only compression forces can be transferred to the steel plate, considering that the rod rests on a sphere without connection in the middle of the steel plate. The dynamic deformation modulus can be determined by using the average maximum plate displacement of three impacts and assuming a constant soil stress, given in equation 3.1 (Adam and Adam, 2003). The DPL can be modeled as a spring-mass-damper system, which is given in figure 6.1.

The mechanical model considers the following assumptions.

- Kelvin Voigt body (linear spring with stiffness  $k$  and viscous damper with damping coefficient  $c$ )
- Mass of falling weight  $m$  is 10 kg
- Mass of guide rod  $m_s$  is 5 kg
- Mass of load plate  $m_p$  is 15 kg
- Falling height  $h_0$  is 0.7 m
- Spring stiffness coefficient  $k$  is 337 N/m
- Damping coefficient  $c$  is 130 Ns/m

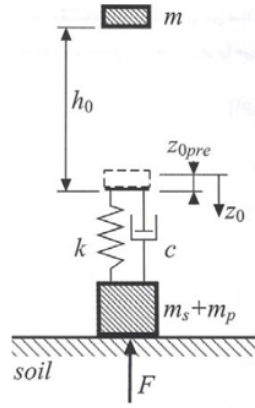


Figure 6.1: Mechanical model of the DPL (Adam and Adam, 2003)

### 6.1.2. Soil

The complex dynamic soil behaviour of the soil is simplified to a viscoelastic one-dimensional wave propagation problem. This is represented by a frequency independent spring-mass-dashpot system given in figure 6.2.

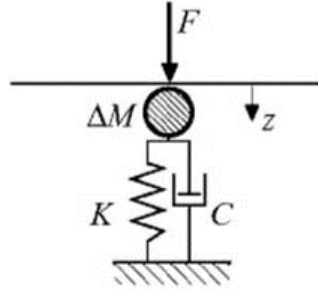


Figure 6.2: One-dimensional soil model of the elastic homogeneous halfspace (Adam and Adam, 2003)

For cohesionless soils the following equations hold:

$$K = 2 \cdot z \cdot E_{dyn} \frac{1 - 2\nu^2}{1 - \nu} \quad (6.1)$$

$$C = \sqrt{2 \cdot \rho \cdot E_{dyn} z^2 \pi} \quad (6.2)$$

$$E_{dyn} \approx \frac{\pi(1 - \nu^2)}{3(1 - 2\nu)} E_{vd} \quad (6.3)$$

The following assumptions were made:

- The difference in mass is negligible compared to the device load.
- $\nu$  is 0.3 (Range silty sand: 0.2 - 0.4)
- $E_{vd}$  is obtained from DPL field test results
- $\rho$  is obtained from NDG field test results

### 6.1.3. DPL-Soil interaction system

The DPL-Soil system is divided into two phases namely the fall phase and the full contact phase. A relevant assumption is that the soil and load plate are in contact during the entire motion.

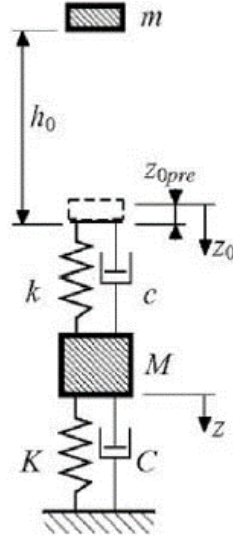


Figure 6.3: DPL-Soil interaction system (Adam and Adam, 2003)

$$z(t_0) = -h_0 + z_{0pre} \quad ; \text{ where } z(t_0) = 0$$

Phase 1: *Fall phase* ( $t_0 \leq t \leq t_1$ )

$$\begin{aligned} \text{During the fall} \quad z_0 &= -h_0 + z_{0pre} + g \frac{t^2}{2}; & ; \text{ where } \dot{z}_0 &= gt \\ \text{Load plate at rest} \quad t_1 &= \sqrt{\frac{2h_0}{g}} & ; \text{ where } z &= \dot{z} = 0 \end{aligned}$$

Phase 2: *Full contact phase* (at  $t = t_1$ )

$$\begin{aligned} F_1 + k(z - z_0) + c(\dot{z} - \dot{z}_0) &= m\ddot{z}_0 & F_2 - Kz - C\dot{z} - k(z - z_0) - c(\dot{z} - \dot{z}_0) &= M\ddot{z} \\ \boxed{M\ddot{z}_0 + c(\dot{z}_0 - \dot{z}) + k(z_0 - z) = F_1 = mg} & & \boxed{M\ddot{z} - c\dot{z}_0 + (c + C)\dot{z} - kz_0 + (k + K)z = F_2 = 0} \end{aligned}$$

$$\begin{bmatrix} m & 0 \\ 0 & M \end{bmatrix} \begin{Bmatrix} \ddot{z}_0 \\ \ddot{z} \end{Bmatrix} + \begin{bmatrix} c & -c \\ -c & c + C \end{bmatrix} \begin{Bmatrix} \dot{z}_0 \\ \dot{z} \end{Bmatrix} + \begin{bmatrix} k & -k \\ -k & k + K \end{bmatrix} \begin{Bmatrix} z_0 \\ z \end{Bmatrix} = \begin{Bmatrix} mg \\ 0 \end{Bmatrix} \quad (6.4)$$

For the full contact phase, the motion can be described by a 2-DOF system. The mass ( $m$ ) and the load device are in full contact when the following equations hold (Adam and Adam, 2003):

$$-kz_{0pre} + k(z - z_0) + c(\dot{z} - \dot{z}_0) \leq 0 \quad \text{and} \quad z_0 - z_{0pre} \geq z$$

## 6.2. Results

By solving the equations of motion, the soil displacement was obtained. This was plotted against the dynamic modulus from the DPL field test and compared to the soil displacement obtained from the DPL field test in figure 6.4.

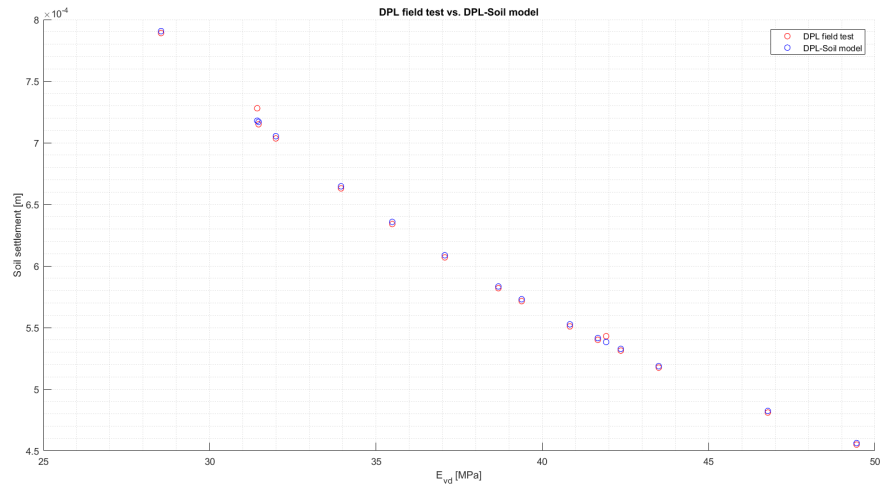


Figure 6.4: DPL field test vs. DPL-Soil model

It can be seen that the DPL-Soil model almost matches the DPL field test results; a maximum margin of error of 1.38 % was found.

Figure 6.5 shows the correlation between the soil settlement obtained from the model and the dynamic modulus. A perfect fit is found with the following equation

$$\text{Soil settlement} = 0.02257E_{vd}^{-1} + 1.114e - 08 \quad (6.5)$$

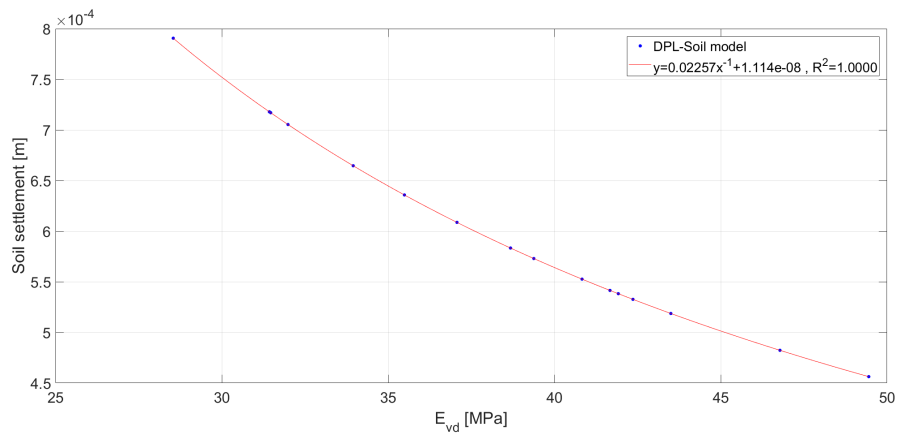


Figure 6.5: Correlation between the soil settlement and the dynamic modulus

# 7

## Discussion

This chapter presents discussions regarding the field test, the correlations, the response of the roller and the DPL-Soil model.

### 7.1. Field test

The results obtained from the HHTT field test showed both expected and unexpected results. The expected increase in cone resistance after each cycle of passes was clearly observed in CPT 281, but this increasing behavior could not always be obtained from the NDG and DPL tests. Although it was unexpected that the soil would be variable. The results showed otherwise as the performed tests showed very location specific behavior. As an example, when surveying the area, large chunks of organic clay were found as well, which could have influenced the results.

From the CPT results it can be seen that the influence depth of the CRC is between 4 to 4.5 m depth, where the maximum impact was recorded between 1 and 3 m depth. (Kelly and Gil, 2012b) shows four different case studies where the 3-sided impact roller is used. The first case study resembles the soil from the HHTT field test the most, considering that it consists of poorly graded sand with silt. The compaction was validated by means of performing CPT. The results showed improvement up to 5 m depth, but the largest improvement of cone resistance was recorded between 0.5 and 2 m from 4.7 MPa to 11.6 MPa after 40 passes. The depth range of improvement coincides with the results from the HHTT field test. The difference lies however in the values of cone resistance. For the HHTT field test an overall improvement of about 2.75 to 20.5 MPa after 30 passes was recorded.

The cone penetration tests performed in order to determine the lateral influence, proved to be insufficient considering that no significant increase in cone resistance was noticed between 0.5 and 2 m from track 2.

The possibility exists that the lateral extent is in the range of 0 to 0.5 m. However, the zone of disturbance of the CPT was included, which accounts for approximately one cone diameter and is equal to 0.4 m.

(Jaksa et al., 2012) carried out a field trial to quantify the zone of influence of the 4-sided impact roller by means of a number of earth pressure cells embedded in the ground. The lateral extent was found to be 1 m from the track, with values of approximately 50 kPa at this horizontal offset.

This difference in lateral influence can be equated to the fact that the CRC roller is a 3-sided roller and therefore has a different pressure distribution. Furthermore, 50 kPa of pressure does not necessarily indicate a visible increase in cone resistance and both field tests were performed on different soils. The soil from (Jaksa et al., 2012) is classified as well graded sand with some clay fines of low plasticity, while the soil used in this thesis is classified as uniform sand with non-plastic silt. The uniform sand will need more compactive effort to reach the same compaction compared to well graded sand.

Regarding the accelerations, the first case study of the study conducted by Kelly and Gil, observed an improve-

ment of initial decelerations from 5.3 g up to 11.4 g after 40 passes (Kelly and Gil, 2012b). This coincides with an improvement from 52 m/s<sup>2</sup> to 112 m/s<sup>2</sup>. The measured decelerations from the HHTT field test reached far lower values, namely an improvement from 25 to 70 m/s<sup>2</sup>. However, during the HHTT field test a higher range of cone resistance values was observed after a lower amount of passes namely 2.75 to 20.5 MPa as opposed to 4.7 to 11.6 MPa. This shows that the soil from the HHTT field test demands less compactive effort compared to the soil from Kelly and Gil's case study and the impact decelerations are not necessarily a quantitative tool to measure the compaction of the soil.

## 7.2. Correlations

The correlations for both the peak acceleration and the peak integrated velocity show a large spreading of the data. A positive linear fit was expected for these variables with the field test measurements, which included the in situ density, dry density, dynamic modulus and average cone resistance.

The four cases for the peak acceleration and the peak integrated velocity included the mean of each cycle, the maximum of each cycle, the last pass of each cycle and the mean of the last pass of each cycle. From these four cases, the best correlation was found for the maximum of each cycle, which was given in section 4.1 and section 4.2.

The amount of spreading in the correlations can be linked to the non-circular shape of the lobe of the roller. From figure 3.5 can be seen that due to the shape of the lobe, the topsoil is pushed as the roller is towed further by the tractor. This causes the topsoil to loosen up to 0.5 m depth. Considering that the accelerometer measures the impact acceleration, these values may vary depending on which surface the lobe hits. The flat part of these undulations indicate a compact surface, while the steeper part indicate a looser surface. With this reasoning, the large spreading of peak acceleration and peak integrated velocity in all correlations could be justified. Furthermore due to this large range of values during each cycle, no proper correlations could be found for cases one, three and four.

## 7.3. Response of the roller

### 7.3.1. Signal processing

The accelerometer uses a 4 kHz sampling rate, which according to (Scott et al., 2019) is a sufficiently high sampling frequency to capture an accurate ground response and ensure an accurate double numerical integration of the acceleration-time data. (Thong et al., 2002) discussed that an increase in accuracy of numerical integration can be achieved by using faster sampling rates, however, an increase in errors can be found depending on the duration of the time interval of integration.

From equation 2.1 it can be seen that for a given sampling rate, the frequency resolution will improve in correspondence to an increase in analyzed data points. Cofra stores 100 samples every impact using a sampling rate of either 50 Hz or 100 Hz, where the initial sampling rate of the accelerometer is 4000 Hz. The accelerometer registers the time in hours, minutes and seconds, whenever an impact takes place. From this data is noted that the time difference in subsequent impacts is 1 s. For the analysis a 100 Hz sampling rate was assumed, considering that when assuming a constant tractor velocity of 3.43 m/s, the time needed for 1 revolution is 1.9 s and during one revolution the roller impacts the ground three times. Hence, when using a sampling rate of 50 Hz, three acceleration pulses would be expected during the time period of 2 s.

This low sampling rate can have a large effect on the acceleration data, namely the actual peak acceleration could not be recognized at this low sampling rate. Furthermore due to the fact that the accelerometer is capped at 8G, the possibility exists that the actual peak acceleration is higher and not recorded by the accelerometer.

### 7.3.2. Displacement response

By comparing the various displacement responses of the roller in, for example, Figure 5.9, it can be seen that after the impact the rebound height is higher than the impact height. This is not what was expected, considering that after compaction the rebound height represents the elastic deformation. Furthermore, by removing the low frequencies as observed in Figure 5.10, the expected displacement response was not obtained. However, as previously mentioned, the upper 0.5 m of the soil layer is disturbed as the roller impacts

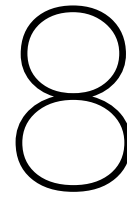
the ground. As the roller is towed by the tractor, the non-circular shape of the lobe causes horizontal shearing forces, which inhibit soil compaction. This has an effect on the corresponding acceleration signal, which is thus not representative of the soil compaction.

When verifying the numerical integration method, it was observed that the differentiated acceleration is shifted by 0.01 s and the peak is reduced by 3 m/s<sup>2</sup>. This could be due to the low sampling rate, which emphasizes any numerical error or difference.

## 7.4. DPL-Soil model

The DPL-Soil model is almost able to produce the DPL field test results. A maximum margin of error of 1.38 % was found. It was noticed that the DPL-Soil model is quite sensitive to the Poisson's ratio  $\nu$  of the soil and that calibrating the data provided a better fit. The DPL-Soil model also assumes a frequency independent spring-mass-dashpot system and uses viscoelastic modeling, even though the compaction of the soil represents a non-linear process. It must thus be noted that the given equations for the spring stiffness and dashpot coefficient of the soil are frequency independent and thus not representative of the soil. However, a perfect fit was found for the relation between the soil settlement and the dynamic modulus. It should be noted that equation 6.5 holds for soil with a Poisson's ratio  $\nu$  of 0.3035.





# Conclusion

This chapter concludes the findings of this study. The research questions described in section 1.2.2 are tackled and hereafter a general conclusion is made.

The aim of this study is to develop a semi-empirical energy model which is based on the contact forces of the roller-soil interface as most CCC systems, but also uses field test data as was given in the CIR system to validate this model. In order to achieve this objective, the following research questions are answered:

## **Which soil properties influence the compaction of the soil?**

From the literature study followed that the soil compaction depends on the frictional force between soil particles supported by the capillary action, and the lubrication effect of the moisture film around the soil particle. These consecutively depend upon the size, shape, soil mineralogy, and the pore water. This correlation between the moisture content and the soil compaction could not be derived from the HHTT test, because due to the larger compactive effort of the roller, the optimum moisture content is lower than from the Standard Proctor test. This is depicted in Figure 3.20.

## **What are the differences between the compaction control systems? (CCC vs. CIR)**

The two compaction control systems discussed in this thesis included the CCC and the CIR system. The differences between these systems include the application and the method. The literature study showed that the CCC system is used for vibratory and oscillatory rollers, while the CIR system is developed for impact rollers. The CCC system assesses the soil stiffness by evaluating the motion behaviour of the dynamically excited drum. Therefore in order to develop this system, the parameters that influence the motion behaviour should be kept constant such as the roller operating parameters (e.g. velocity), and the motion behaviour should be recorded.

The CIR system uses the accelerometer, which is placed on the axle between the two modules. The acceleration is measured continuously and the peak deceleration is recorded at each impact. These peak decelerations give an indication of the response of the soil, where lower decelerations indicate a softer response and an increase in deceleration indicate a stiffer soil. In order to provide a more qualitative answer, the decelerations are related to an appropriate traditional engineering measurement catered to the particular site. These include cone penetration testing, dynamic cone penetration, plate load testing, zone load testing or california bearing ratio, which are performed at the specific points where deceleration data is measured. These correlations are colorcoded and using the GPS data of the roller, depicted in a map.

By comparing both systems, it is noted that the CCC system provides a more accurate representation of the soil compaction, namely a value. While the CIR system provides a range of deceleration values for a given

compaction requirement, based on correlations. From the correlations performed in this thesis, it can be seen that with the given data, this CIR system would not provide an accurate representation of the soil compaction.

#### **What are the relevant parameters needed for the Roller-Soil model?**

The Roller-Soil model is based on modelling the roller as a dynamic plate load test. As a first step in this process, the DPL-Soil model was made. As input for this model the following parameters were used including the dynamic modulus, the in situ density and the velocity with which the DPL hits the soil. After validation of this model, the spring stiffness and damping coefficient of the viscoelastic soil were obtained, which could be used in the Roller-Soil model. This is a semi-empirical energy model which also considers the dissipation of energy by means of the difference in maximum and minimum acceleration. By integrating this difference over the time and multiplying it with the contact force, the amount of work could be determined.

#### **Which steps should be considered when analyzing acceleration data for displacement purposes?**

First, the acceleration data should be detrended by subtracting the mean from the acceleration signals. Hereafter, the data is filtered based on the accelerometer specifications, the sampling rate and the observed time window. Lastly the numerical integration method should be chosen.

Unfortunately, the main aim of developing a semi-empirical energy model, which combined both the CCC and CIR system was not achieved. The recorded acceleration signals were proven not to be representative of the soil compaction. Several factors contributed to this finding. Firstly, the accelerometer used had a limit of 8 G, which could imply that the peak acceleration was not captured. Secondly, the low sampling rate of 100 Hz could also contribute to the loss of peak accelerations. Thirdly, as the roller is towed by the tractor, the non-circular shape of the lobe caused horizontal shearing forces, which inhibited soil compaction and caused soil disturbance up to 0.5 m.

As a result of this, a wide range (21 - 68 m/s<sup>2</sup>) of peak acceleration values was observed regardless of the amount of passes. Due to this large spread of data, no clear correlation could be drawn between the peak acceleration and the field test measurements.

However, a perfect fit was found between the DPL-Soil model and the DPL field test measurements. With this model the corresponding dynamic modulus for a given soil settlement was determined for a silty sand with a Poisson's ratio  $\nu$  of 0.3035.

# 9

## Recommendations

Considering that this study was unable to produce a reliable semi-empirical energy model, the following steps are recommended:

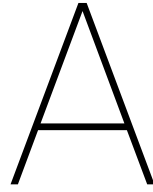
- The 8G accelerometer should be replaced with a sensor with higher range e.g. 16G accelerometer and the sampling rate should be increased to at least 1000 Hz to ensure that the peak acceleration is captured.
- In order to get an accurate acceleration response measured on the axle, it is recommended to bury accelerometers at a minimum depth of 0.5 m.
- In this thesis, the load was estimated from the acceleration signals. In order to get a more accurate representation of the pressures imparted into the ground, earth pressure cells would have to be placed at a minimum depth of 0.5 m.
- Considering the uneven pressure distribution of the roller, it is also recommended to bury these earth pressure cells at various depths to get a more accurate representation of the pressure distribution through the soil layers.
- Low frequency geophones can be used to measure the velocity directly. This because low frequency data of the accelerometer should be removed and the roller works on a low frequency.
- In order to obtain the displacement response of the roller, the trapezoidal rule was used as numerical integration method. The accuracy of the obtained response can be tested by also using other methods such as Simpson's 3/8 rule and Boole's rule.
- The DPL-Soil model can be used as a measure for the soil compaction due to the roller. However, the model in this study is based on silty sand. Further research is required to obtain the correlations for various soils.
- In order to filter out the soil variability, a field test with the roller should be performed on a homogeneous sand without fines. Correlations can then be drawn again for the same field tests performed in this thesis.
- Finite Element Modelling (FEM) could be used to model the interaction between the non-circular shape of the lobe, the rolling motion and the soil. This might form a better correction method for the acceleration signals than those explained in this thesis.



# Bibliography

- Hes hartel tank terminal. <https://www.portofrotterdam.com/en/our-port/port-development/hes-hartel-tank-terminal>. Accessed: 2019-04-22.
- C. Adam and D. Adam. Modelling of the dynamic load plate test with the light falling weight device. *Asian Journal of Civil Engineering*, 4:73–89, 01 2003.
- C. Adam, D. Adam, F. Kopf, and I. Paulmichl. Computational validation of static and dynamic plate load testing. *Acta Geotechnica*, 4(1):35–55, Mar 2009. ISSN 1861-1133. doi: 10.1007/s11440-008-0081-0. URL <https://doi.org/10.1007/s11440-008-0081-0>.
- D. Adam and H. Brandl. Sophisticated continuous compaction control of soils and granular materials. In *Proceedings of the international conference on soil mechanics and foundation engineering-international society for soil mechanics and foundation engineering*, volume 1, pages 31–36. AA BALKEMA, 1997.
- D. M. Boore and J. J. Bommer. Processing of strong-motion accelerograms: needs, options and consequences. *Soil Dynamics and Earthquake Engineering*, 25(2):93 – 115, 2005. ISSN 0267-7261. doi: <https://doi.org/10.1016/j.soildyn.2004.10.007>. URL <http://www.sciencedirect.com/science/article/pii/S0267726104001708>.
- D. Cacciola. *Using continuous compaction control systems within an earthwork compaction specification framework*. PhD thesis, University of Delaware, 2013.
- CofraB.V. Cofra roller compaction capability sheet. Technical report, 2016.
- CofraB.V. *CRC manual*, 2018.
- EEEGuide. Active filters types. URL <https://www.eeeguide.com/active-filters-types/>.
- flatGEO Consulting Company Limited. Compaction test. URL <http://flatgeo.com/index.php/en/geotech-issue/soil-testing-issue/79-compaction-test>.
- A. S. for Testing and Materials. *Annual Book of ASTM Standards*. 1992.
- C. Hogentogler. Essentials of soil compaction. In *Highway Research Board Proceedings*, volume 16, 1937.
- M. Jaksa, B. Scott, N. Mentha, A. Symons, S. Pointon, P. Wrightson, and E. Syamsuddin. Quantifying the zone of influence of the impact roller. pages 9–10, 05 2012.
- D. Kelly. 3 sided high energy impact compaction (heic) modelling - depth of influence > 3m - landpac. <https://www.linkedin.com/pulse/3-sided-high-energy-impact-compaction-heic-modelling-dermot-kelly/>, year = 2016, note = Accessed+: 2019-06-30.
- D. Kelly and J. Gil. Monitoring heic using landpac cir and cis technologies. 05 2012a.
- D. Kelly and J. Gil. Monitoring heic using landpac cir and cis technologies. pages 7–11, 05 2012b.
- D. B. Kelly et al. Deep in-situ ground improvement using high energy impact compaction (heic) technology. In *ISRM International Symposium*. International Society for Rock Mechanics and Rock Engineering, 2000.
- K. Kim and S. Chun. Finite element analysis to simulate the effect of impact rollers for estimating the influence depth of soil compaction. *KSCE Journal of Civil Engineering*, 20(7):2692–2701, 2016.
- Landpac. Using the landpac continuous impact response measurement (cir) system as a site verification tool. Technical report. Accessed+: 2020-01-08.

- F. Mathijssen. Technische memo - concept, hes hartel tank terminal, rotterdam, eisen conusweerstand zand aanvullen bouwput diepzeekade en binnenvaartkade. Technical report, Hydronomic, 05 2019.
- K. McCann and N. Schofield. Innovative methods in the in-situ determination of design parameters on heterogeneous sites subject to ground treatment using deep impact compaction. In *Proceedings of the 10th Australia–New Zealand conference on geomechanics*, pages 126–131, 2007.
- A. Patel. 2 - soil compaction. In A. Patel, editor, *Geotechnical Investigations and Improvement of Ground Conditions*, Woodhead Publishing Series in Civil and Structural Engineering, pages 7 – 18. Woodhead Publishing, 2019. ISBN 978-0-12-817048-9. doi: <https://doi.org/10.1016/B978-0-12-817048-9.00002-0>. URL <http://www.sciencedirect.com/science/article/pii/B9780128170489000020>.
- J. Pistor, S. Villwock, W. Völkel, F. Kopf, and D. Adam. Continuous compaction control (ccc) with oscillating rollers. *Procedia Engineering*, 143:514 – 521, 2016. ISSN 1877-7058. doi: <https://doi.org/10.1016/j.proeng.2016.06.065>. URL <http://www.sciencedirect.com/science/article/pii/S1877705816305057>. Advances in Transportation Geotechnics III.
- R. Ranasinghe. *Prediction of the Effectiveness of Rolling Dynamic Compaction Using Artificial Intelligence Techniques and In Situ Soil Test Data*. PhD thesis, 2017.
- M. J. Rogers, K. Hrovat, K. McPherson, M. E. Moskowitz, and T. Reckart. Accelerometer data analysis and presentation techniques. 1997.
- B. Scott, M. Jaksa, and P. Mitchell. Ground response to rolling dynamic compaction. *Géotechnique Letters*, 9 (2):99–105, 2019.
- S. systems. Ellipse 2 ahrs ins high performance, miniature inertial sensors hardware manual. Technical report, 2018. Accessed: 2020-01-23.
- M. D. The Virginia Department of Transportation (VDOT). *VDOT Soils and Aggregate Compaction*, chapter Field Moisture and Density Testing with the Nuclear Gauge. 2016.
- Y. Thong, M. Woolfson, J. Crowe, B. Hayes-Gill, and R. Challis. Dependence of inertial measurements of distance on accelerometer noise. *Measurement Science and Technology*, 13(8):1163, 2002.
- D. A. Tsouvalas. Cie5260 structural response to earthquakes, September 2019.



# Correlations

## A.1. Peak accelerations

### A.1.1. Mean peak acceleration of each cycle

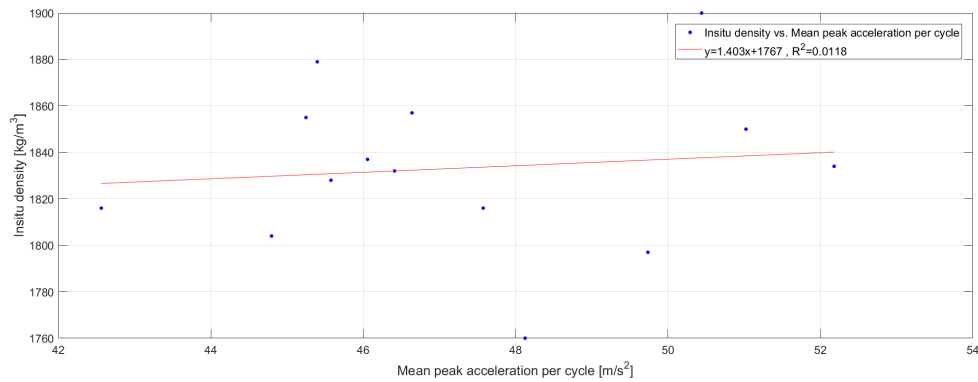


Figure A.1: Insitu density vs. Mean peak acceleration per cycle

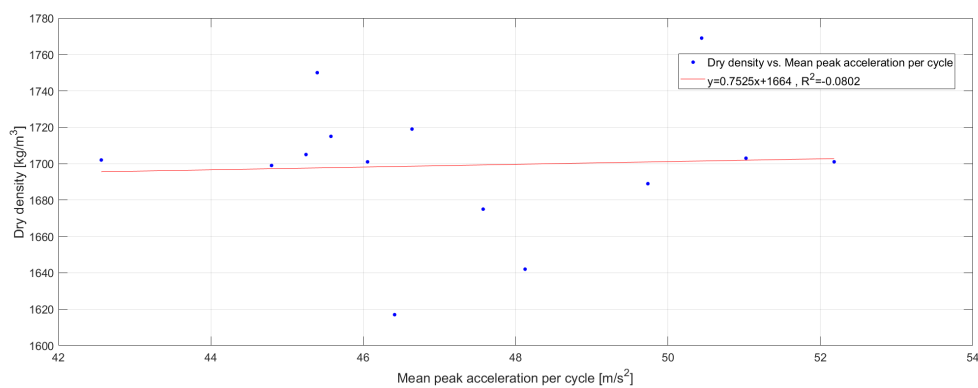


Figure A.2: Dry density vs. Mean peak acceleration per cycle

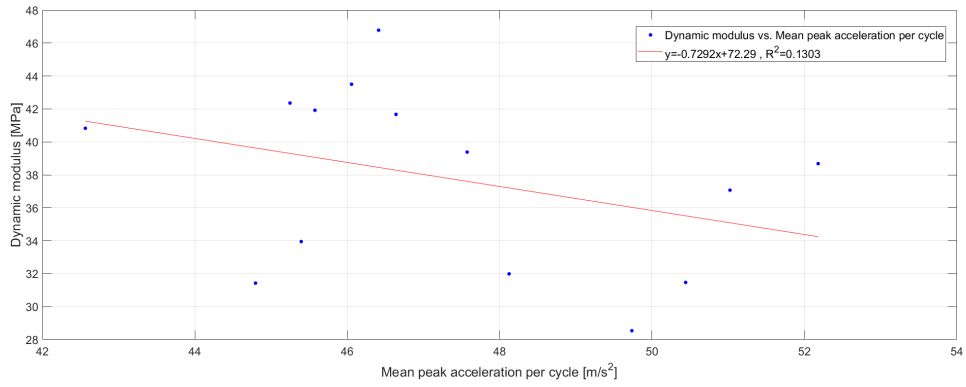


Figure A.3: Dynamic modulus vs. Mean peak acceleration per cycle

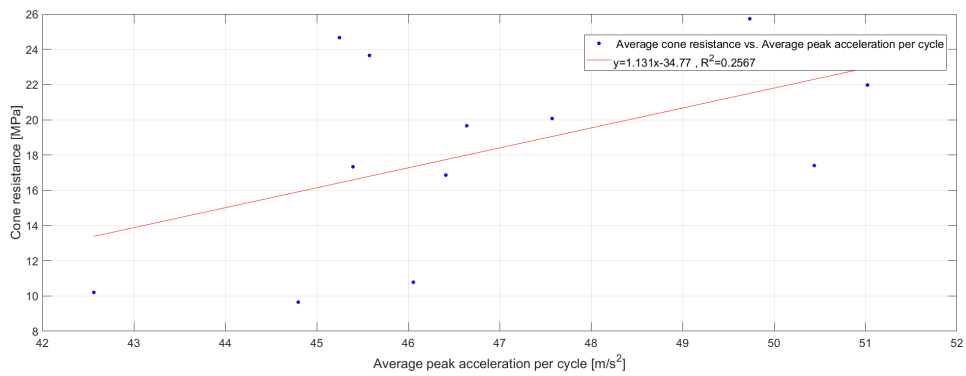


Figure A.4: Average cone resistance vs. Average peak acceleration per cycle

### A.1.2. Peak acceleration of the last pass of each cycle

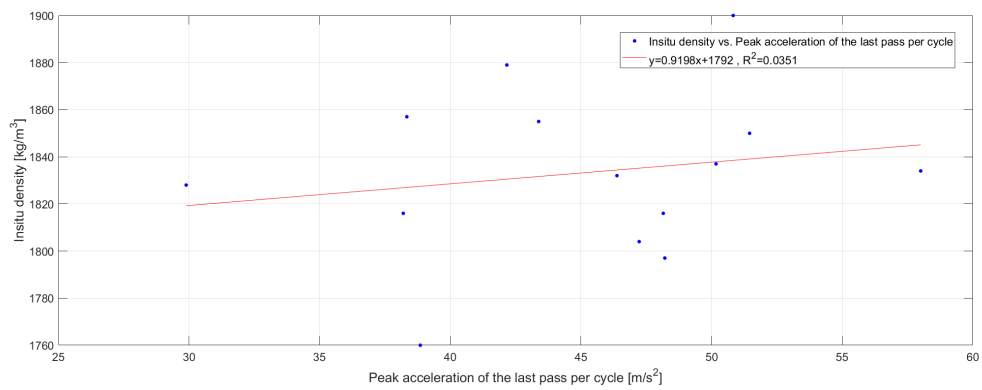


Figure A.5: Insitu density vs. Peak acceleration of the last pass per cycle

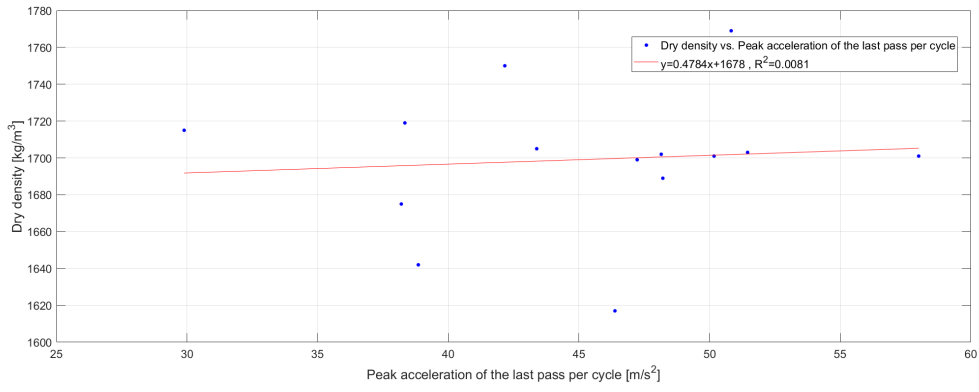


Figure A.6: Dry density vs. Peak acceleration of the last pass per cycle

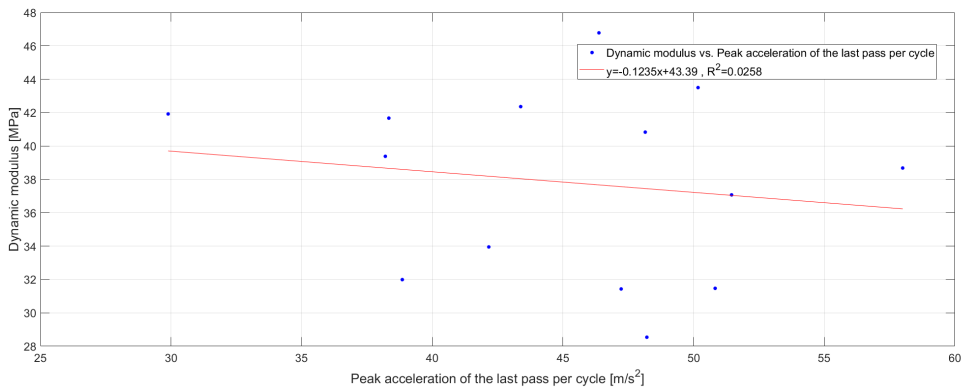


Figure A.7: Dynamic modulus vs. Peak acceleration of the last pass per cycle

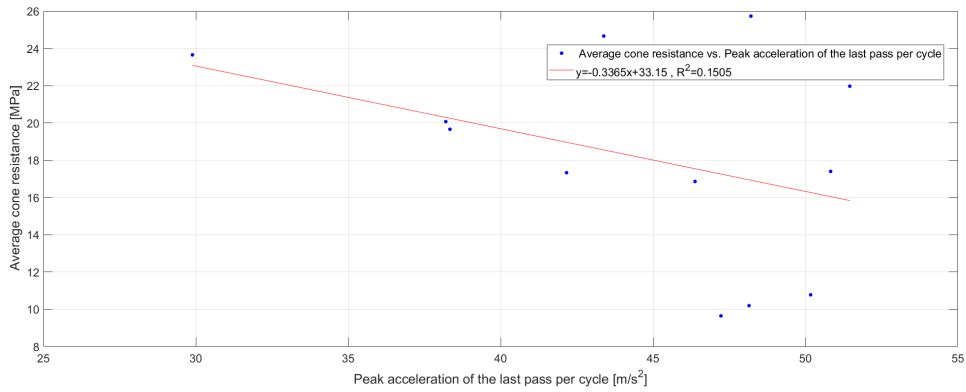


Figure A.8: Average cone resistance vs. Peak acceleration of the last pass per cycle

### A.1.3. Mean peak acceleration of the last pass of each cycle

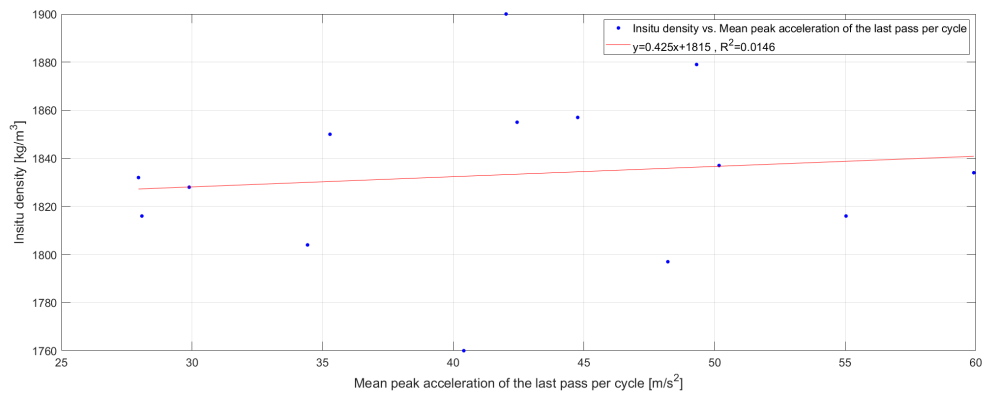


Figure A.9: Insitu density vs. Mean peak acceleration of the last pass per cycle

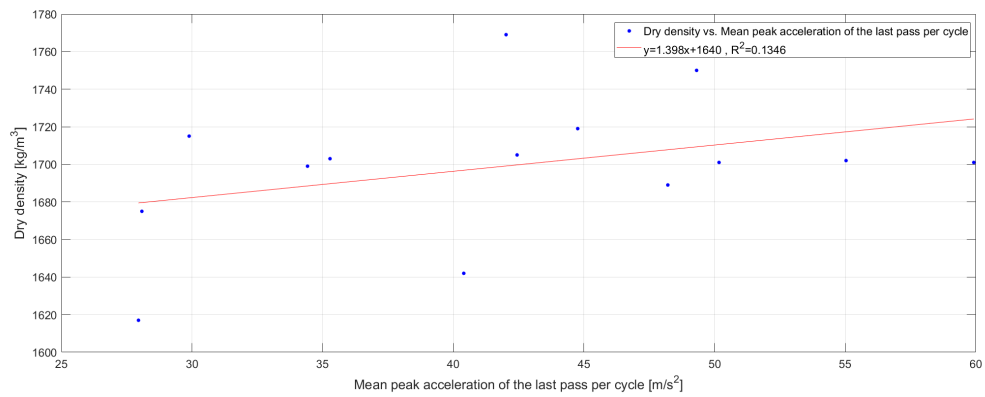


Figure A.10: Dry density vs. Mean peak acceleration of the last pass per cycle

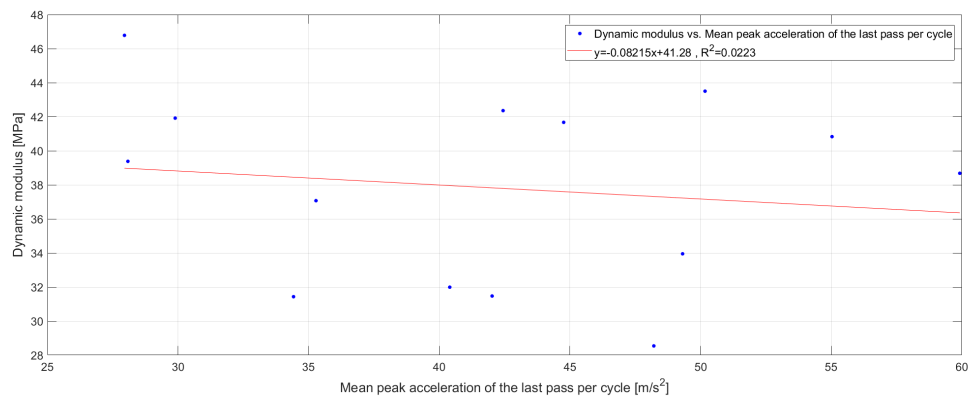


Figure A.11: Dynamic modulus vs. Mean peak acceleration of the last pass per cycle

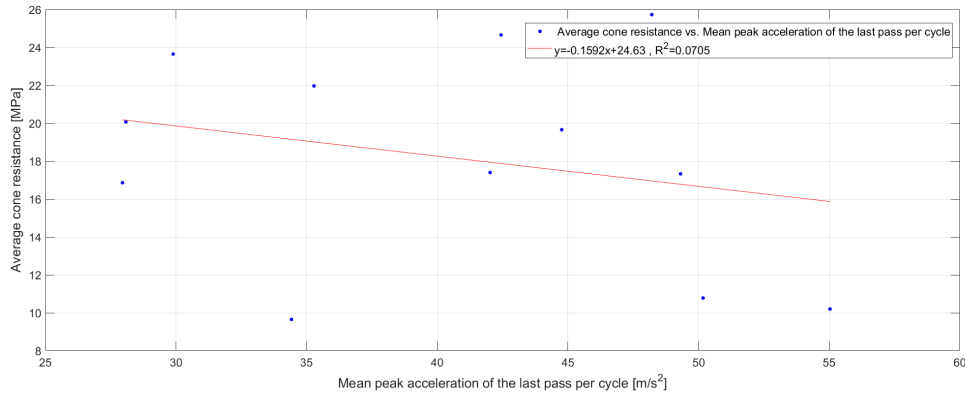


Figure A.12: Average cone resistance vs. Mean peak acceleration of the last pass per cycle

## A.2. Integrated peak velocities

### A.2.1. Mean integrated peak velocities of each cycle

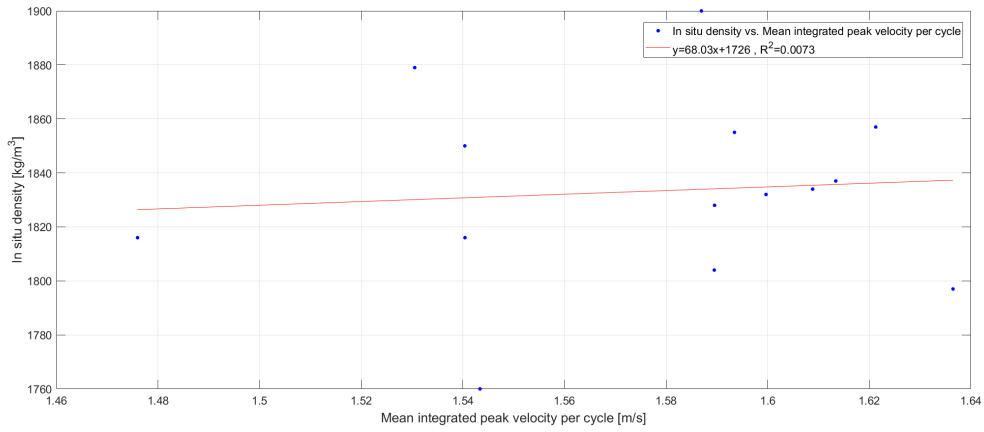


Figure A.13: Insitu density vs. Mean integrated peak velocity per cycle

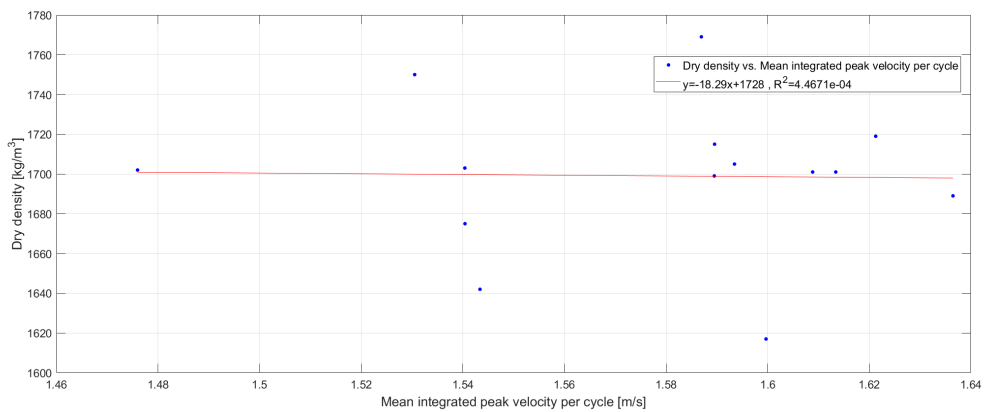


Figure A.14: Dry density vs. Mean integrated peak velocity per cycle

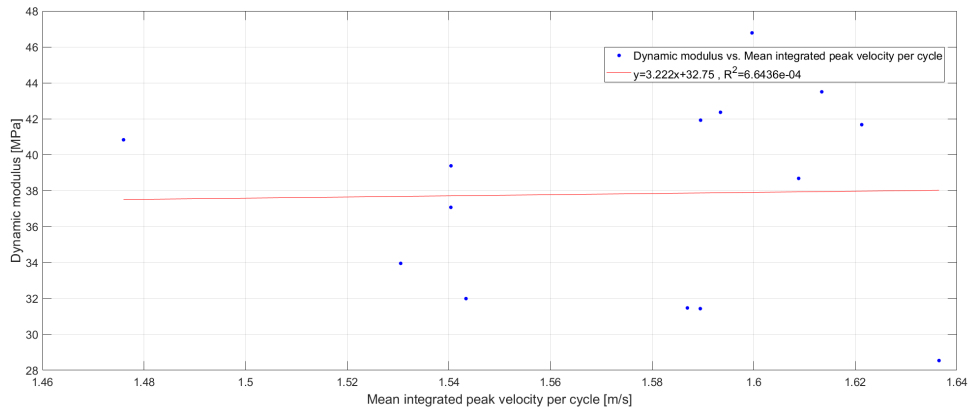


Figure A.15: Dynamic modulus vs. Mean integrated peak velocity per cycle

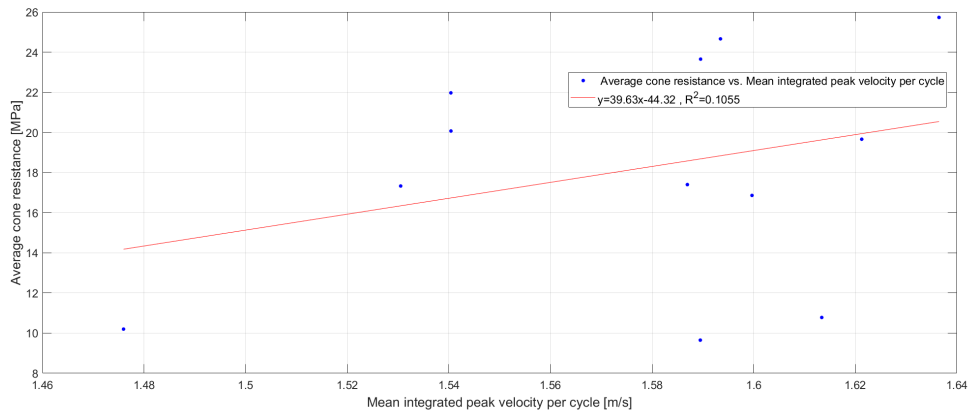


Figure A.16: Average cone resistance vs. Mean integrated peak velocity per cycle

### A.2.2. Integrated peak velocity of the last pass of each cycle

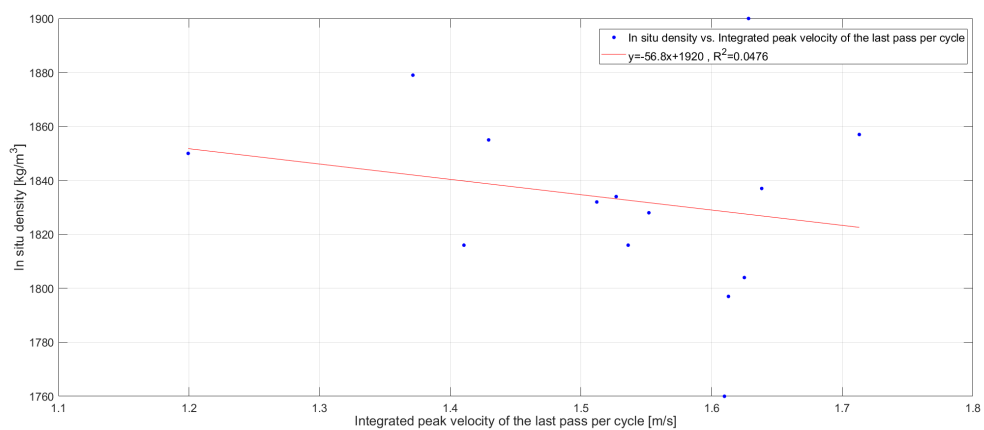


Figure A.17: In situ density vs. Integrated peak velocity of the last pass per cycle

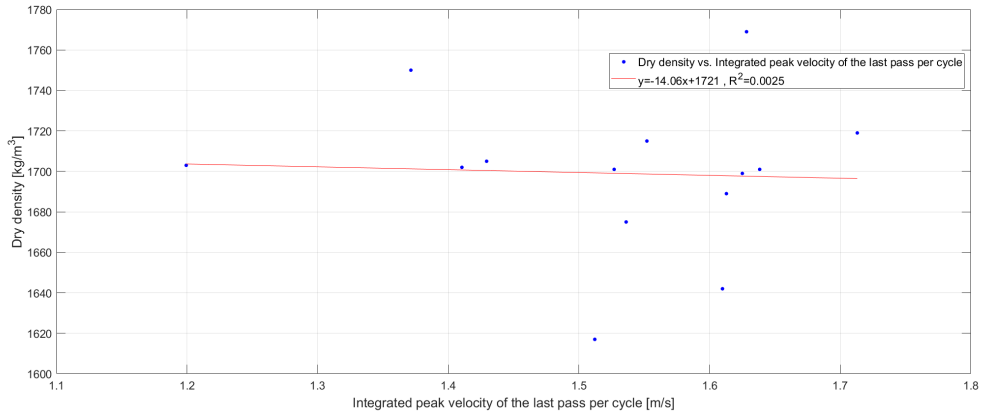


Figure A.18: Dry density vs. Integrated peak velocity of the last pass per cycle

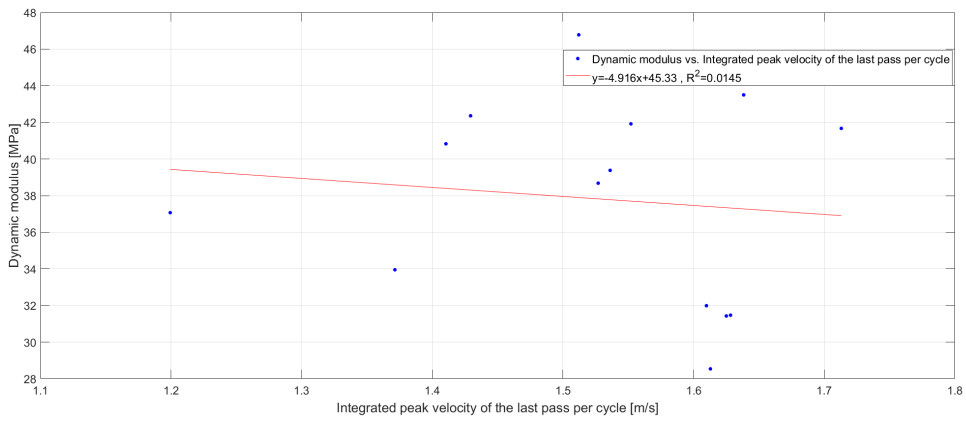


Figure A.19: Dynamic modulus vs. Integrated peak velocity of the last pass per cycle

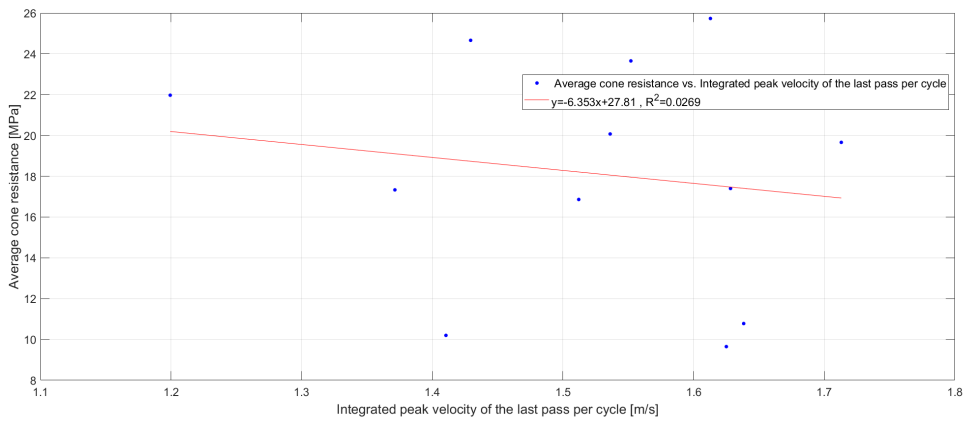


Figure A.20: Average cone resistance vs. Integrated peak velocity of the last pass per cycle

### A.2.3. Mean integrated peak velocity of the last pass of each cycle

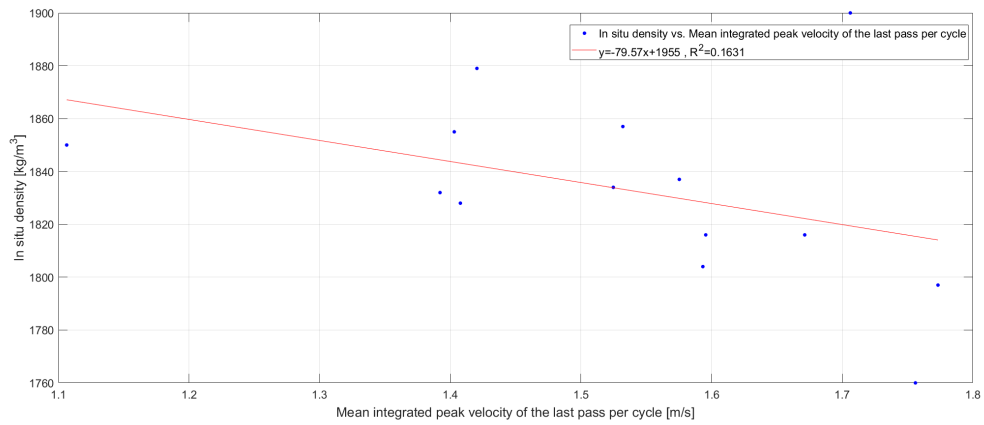


Figure A.21: In situ density vs. Mean integrated peak velocity of the last pass per cycle

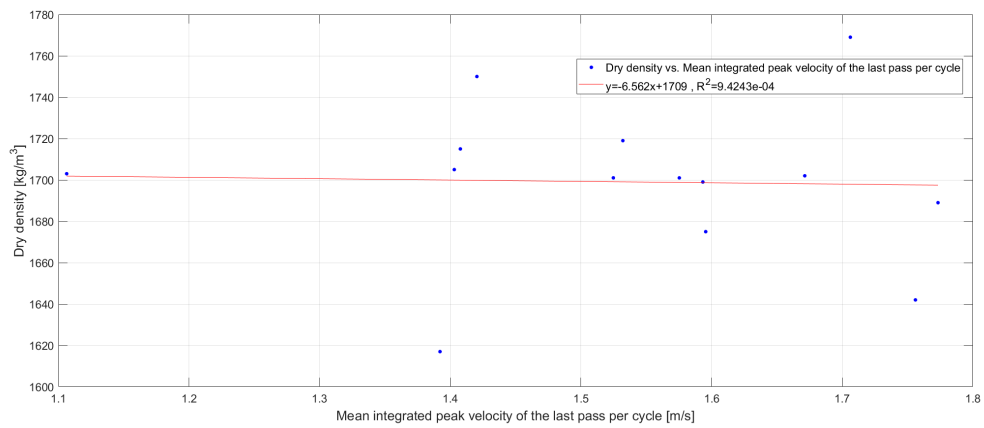


Figure A.22: Dry density vs. Mean integrated peak velocity of the last pass per cycle

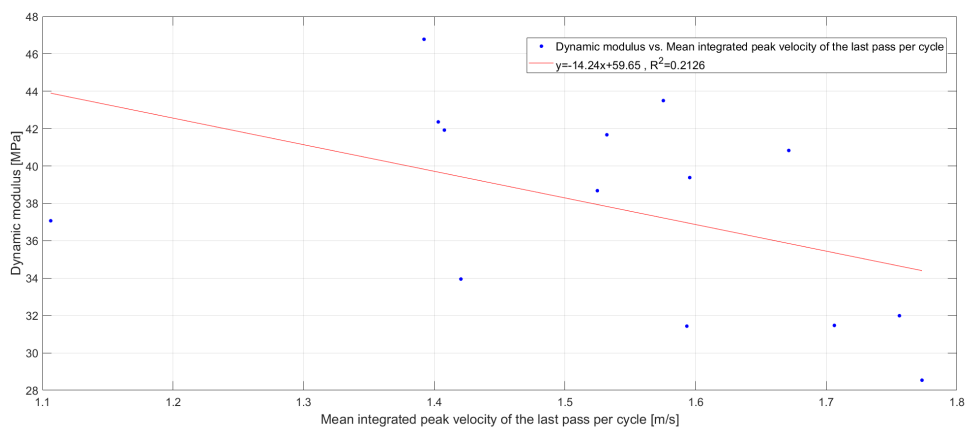


Figure A.23: Dynamic modulus vs. Mean integrated peak velocity of the last pass per cycle

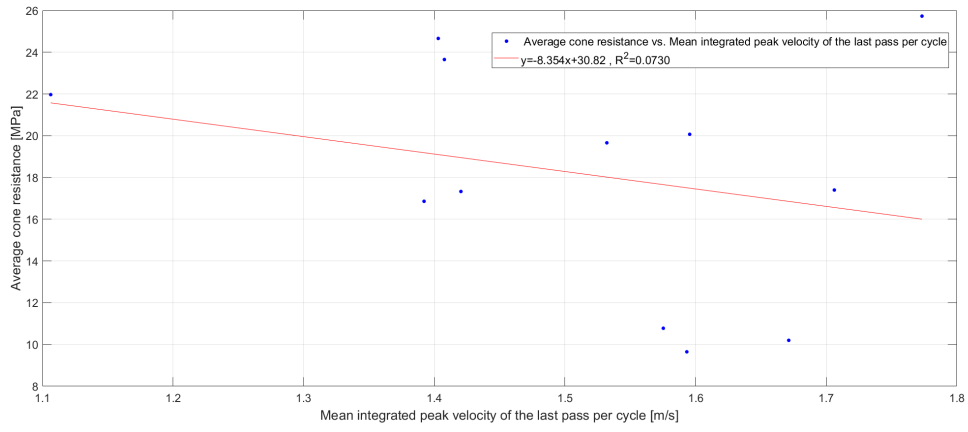


Figure A.24: Average cone resistance vs. Mean integrated peak velocity of the last pass per cycle



# B

## Displacement response of the roller

### **B.1.** Displacement response with band-pass filter of 1 to 28 Hz

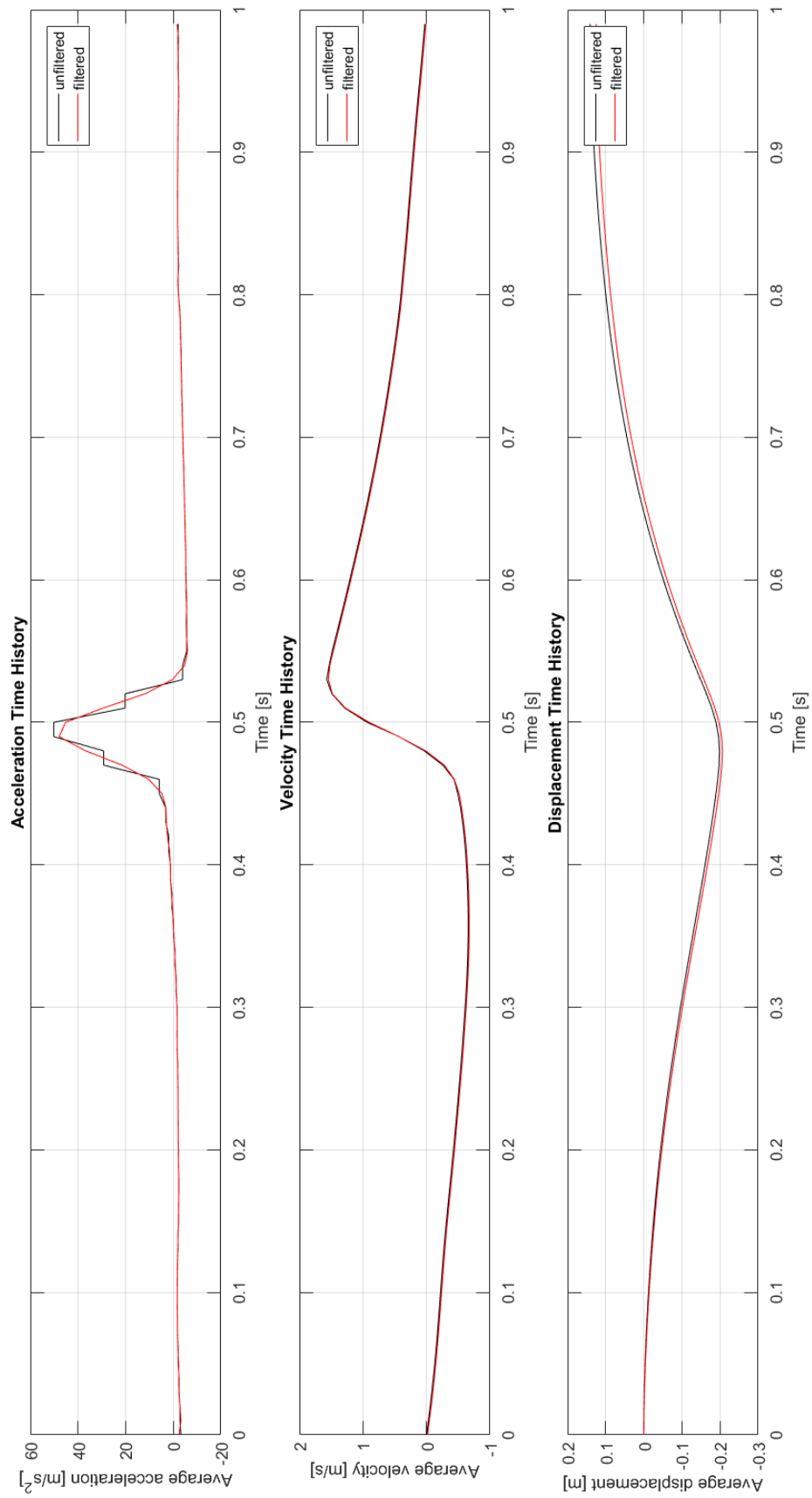


Figure B.1: Displacement response of the roller after 5 passes at location 1

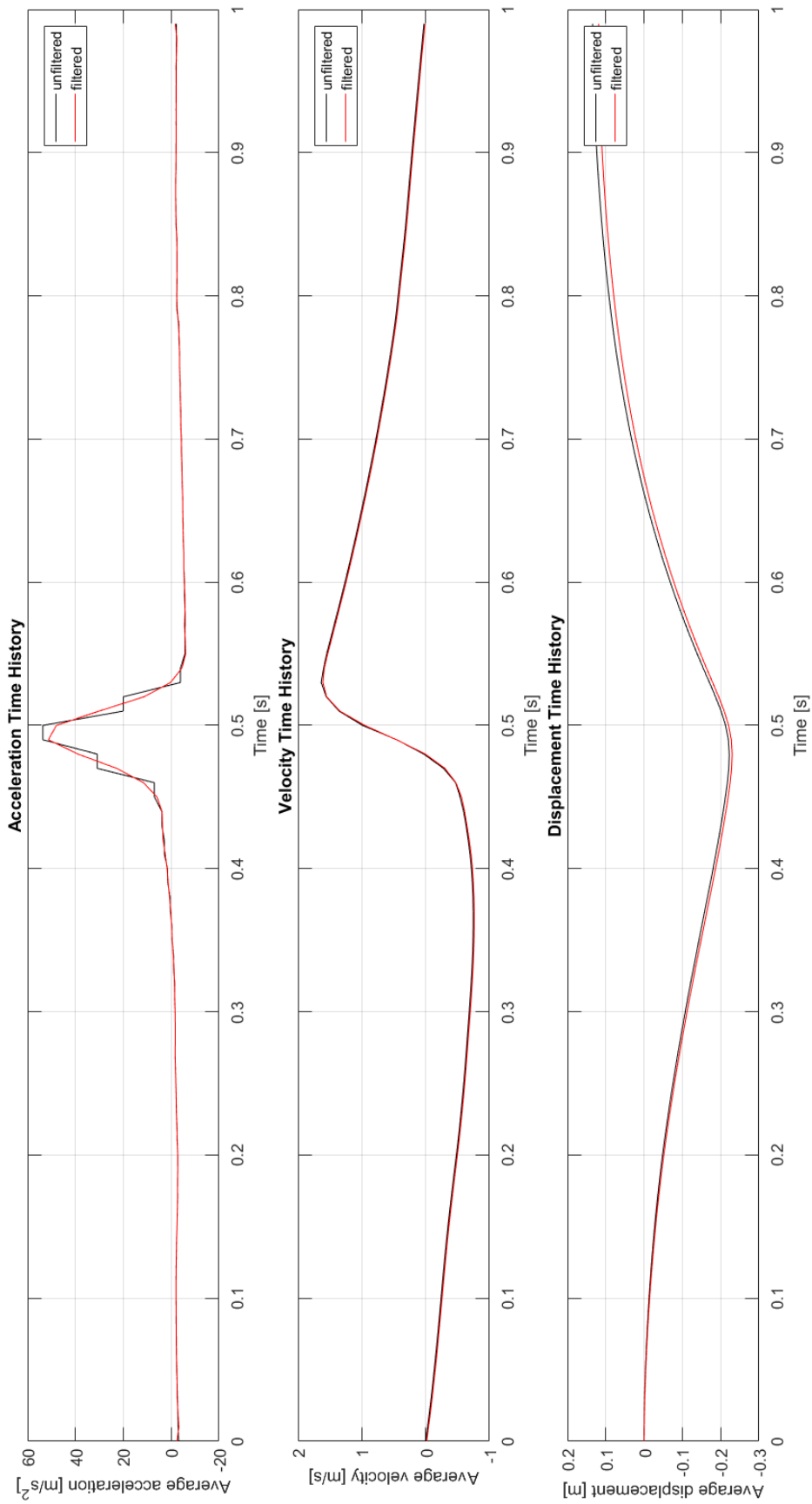


Figure B.2: Displacement response of the roller after 5 passes at location 2

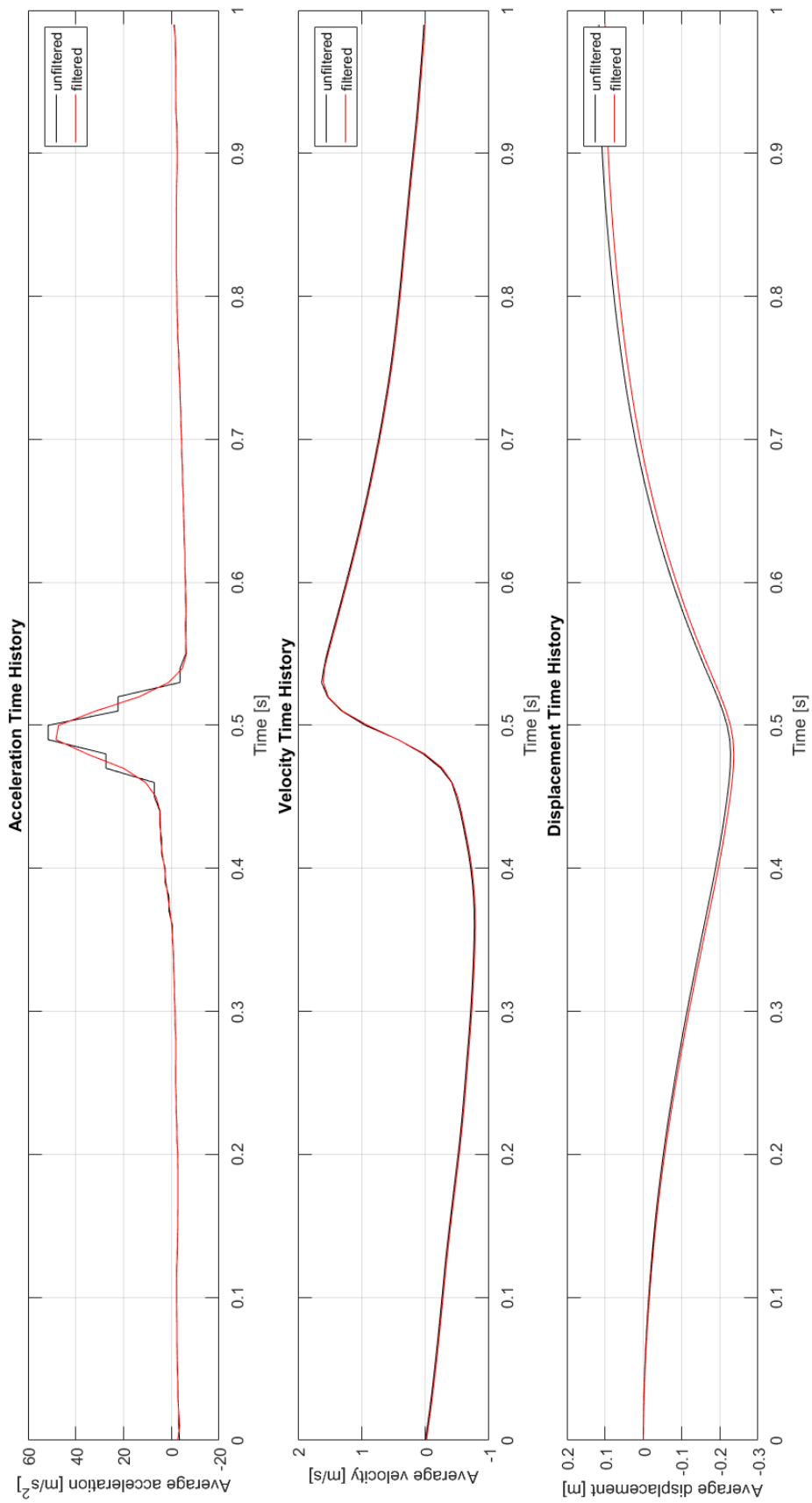


Figure B.3: Displacement response of the roller after 5 passes at location 264

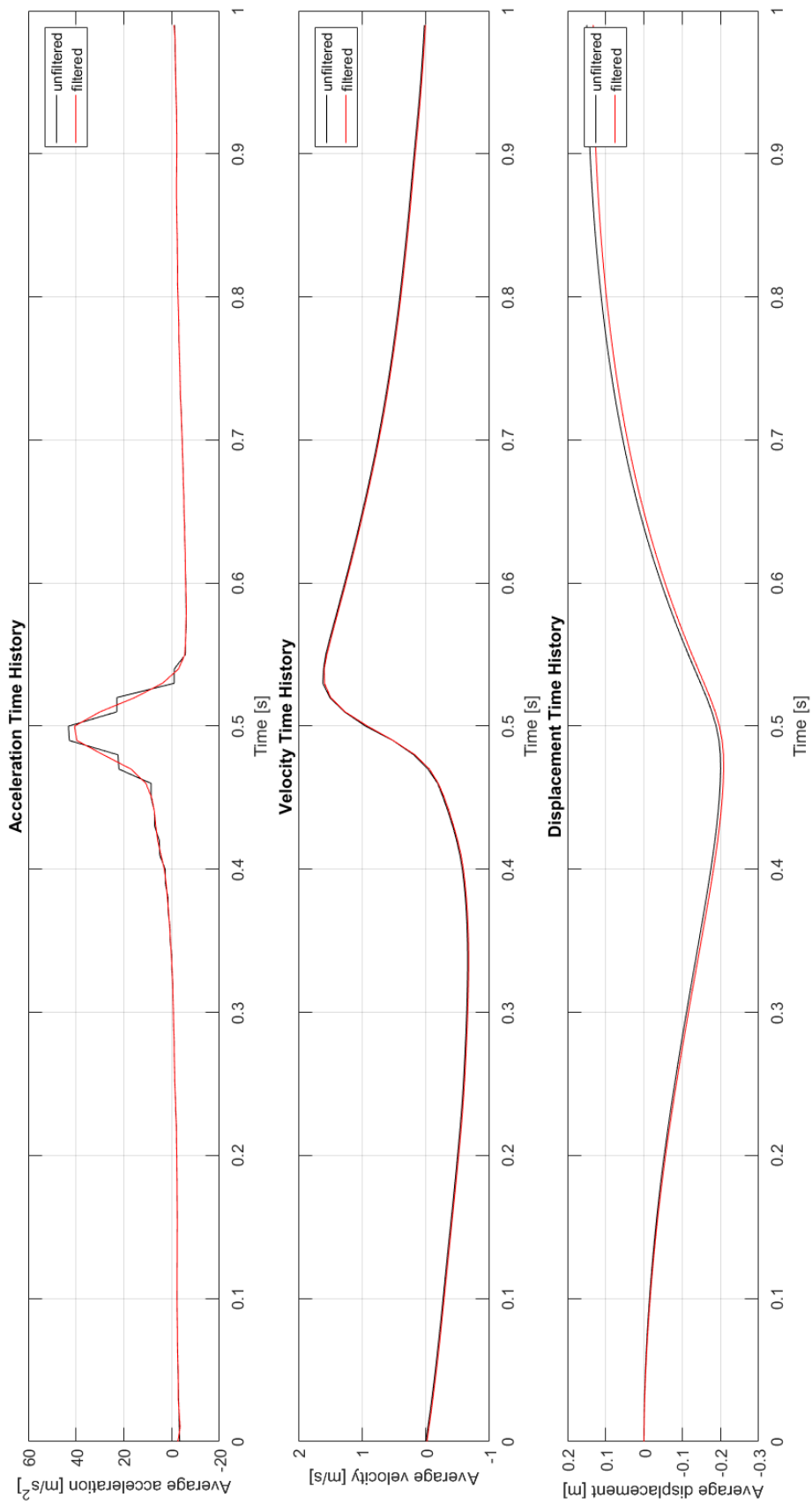


Figure B.4: Displacement response of the roller after 20 passes at location 264

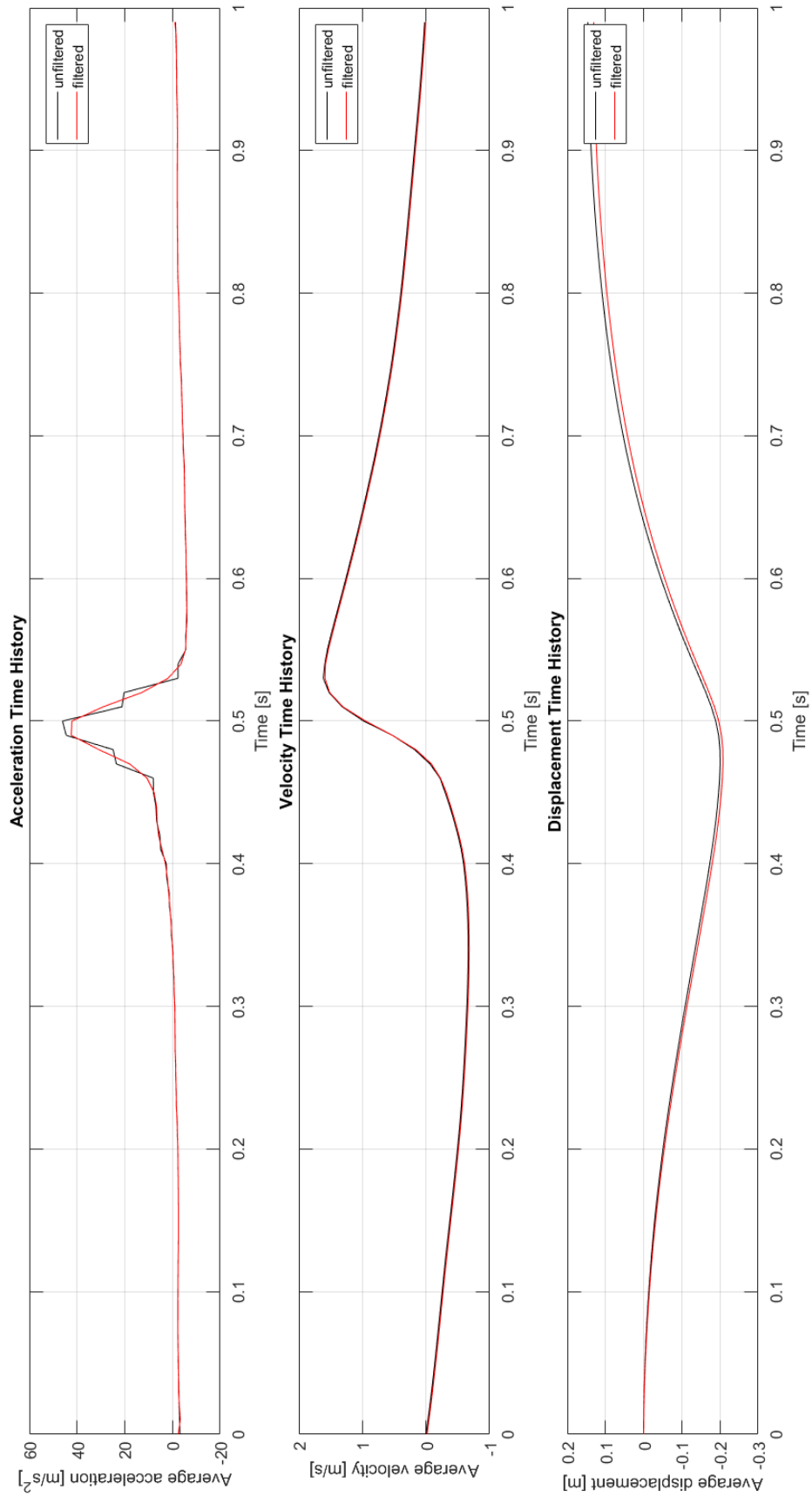


Figure B.5: Displacement response of the roller after 30 passes at location 264

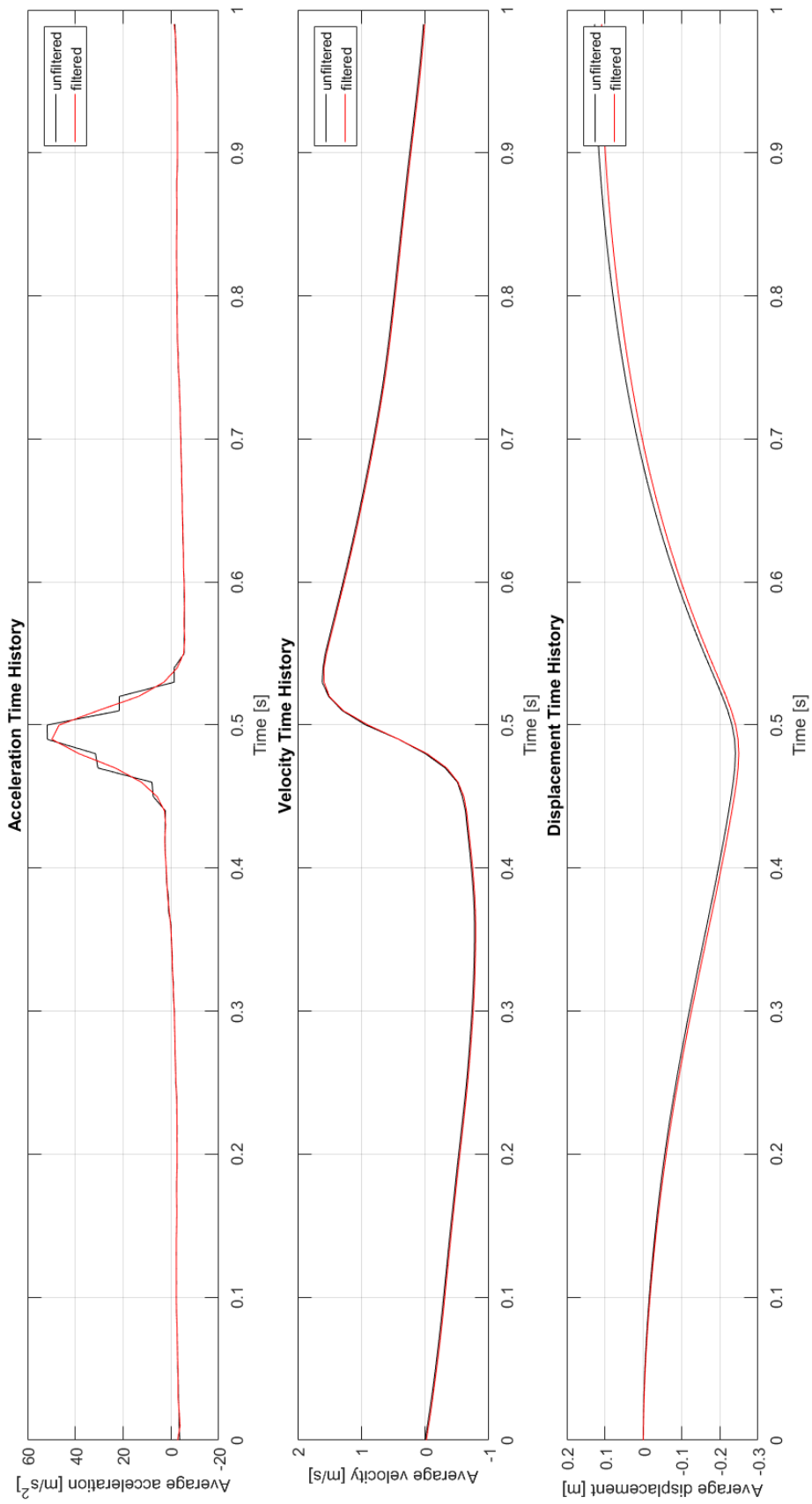


Figure B.6: Displacement response of the roller after 5 passes at location 267

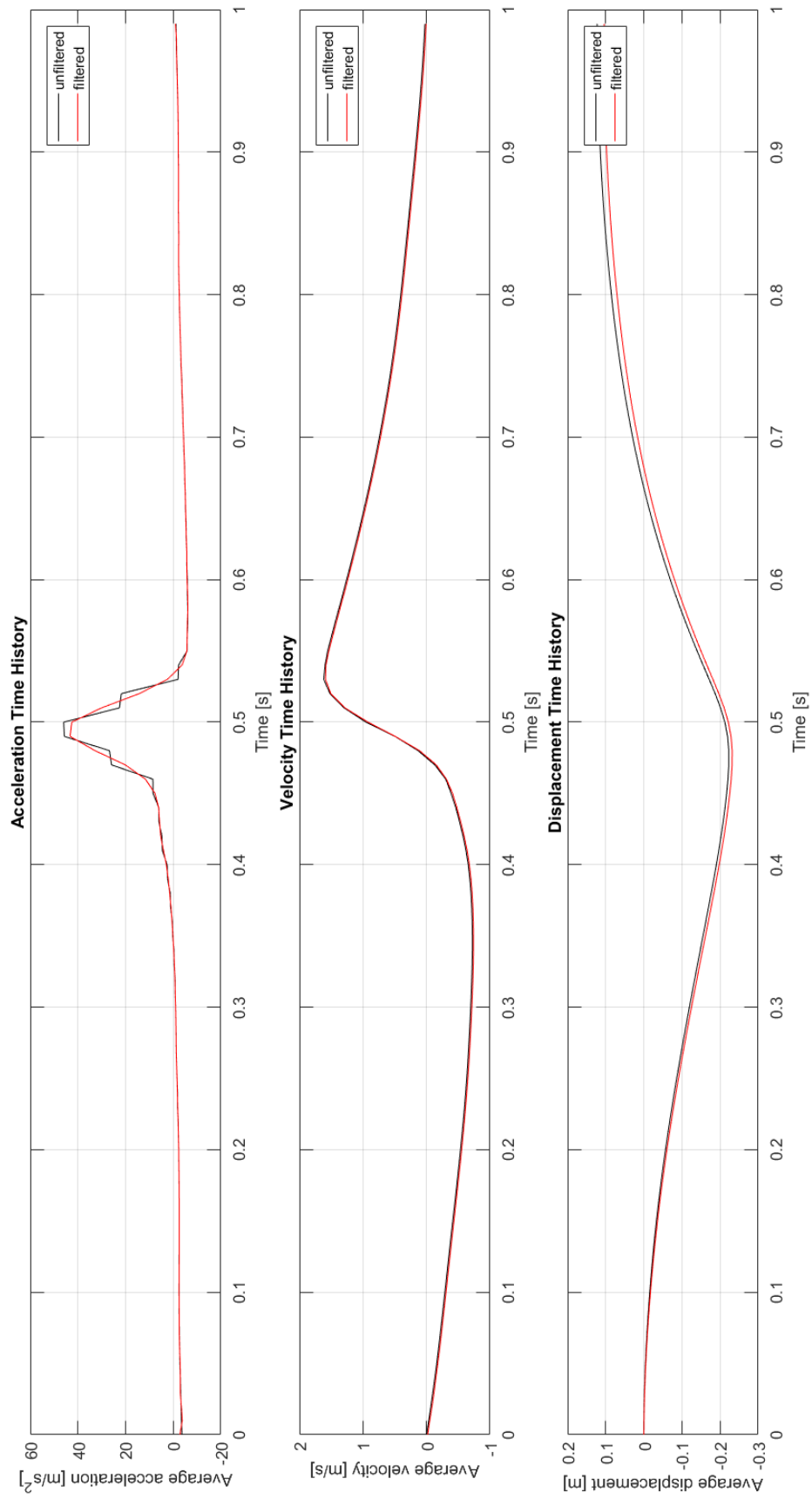


Figure B.7: Displacement response of the roller after 20 passes at location 267

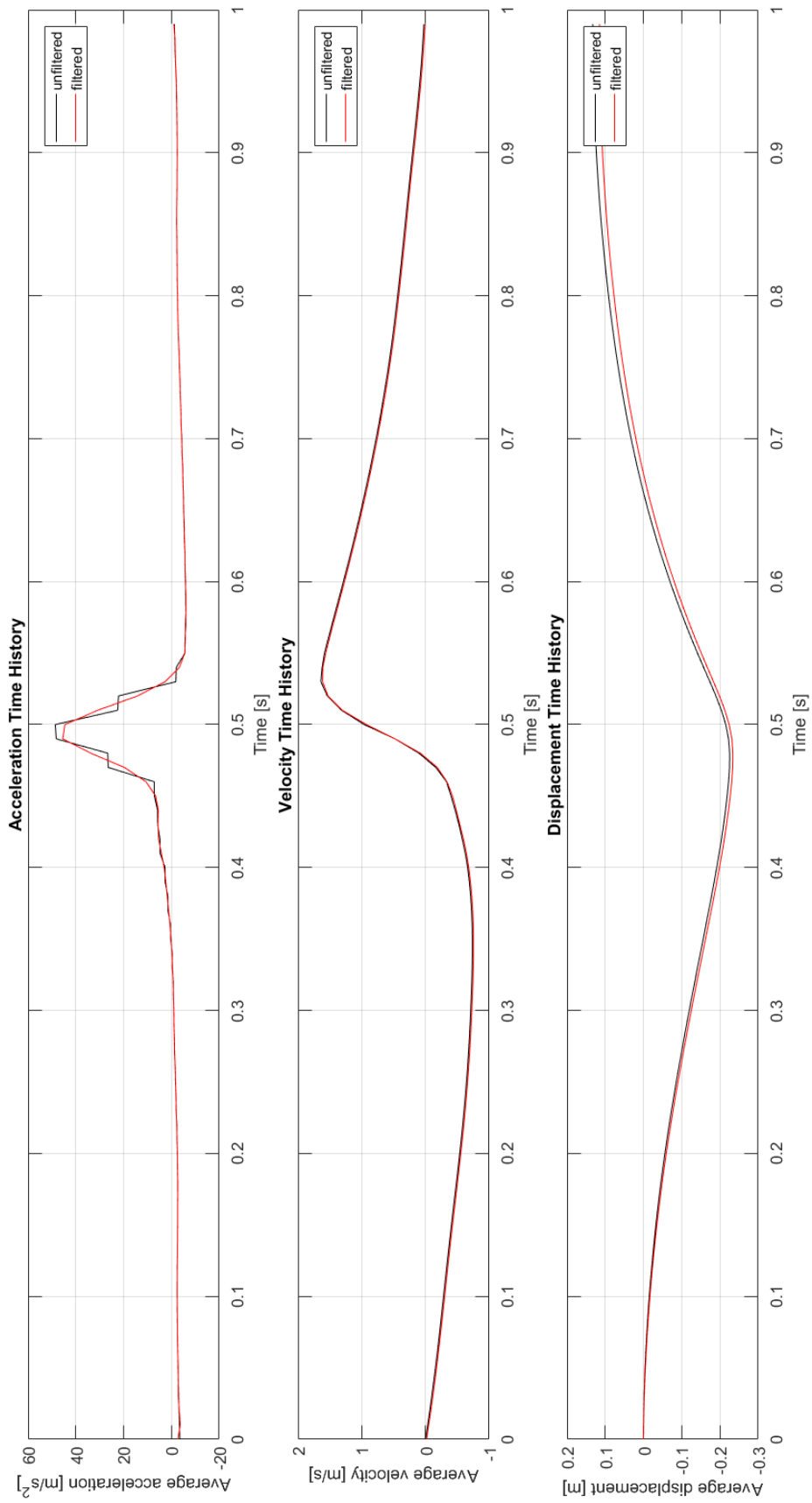


Figure B.8: Displacement response of the roller after 30 passes at location 267

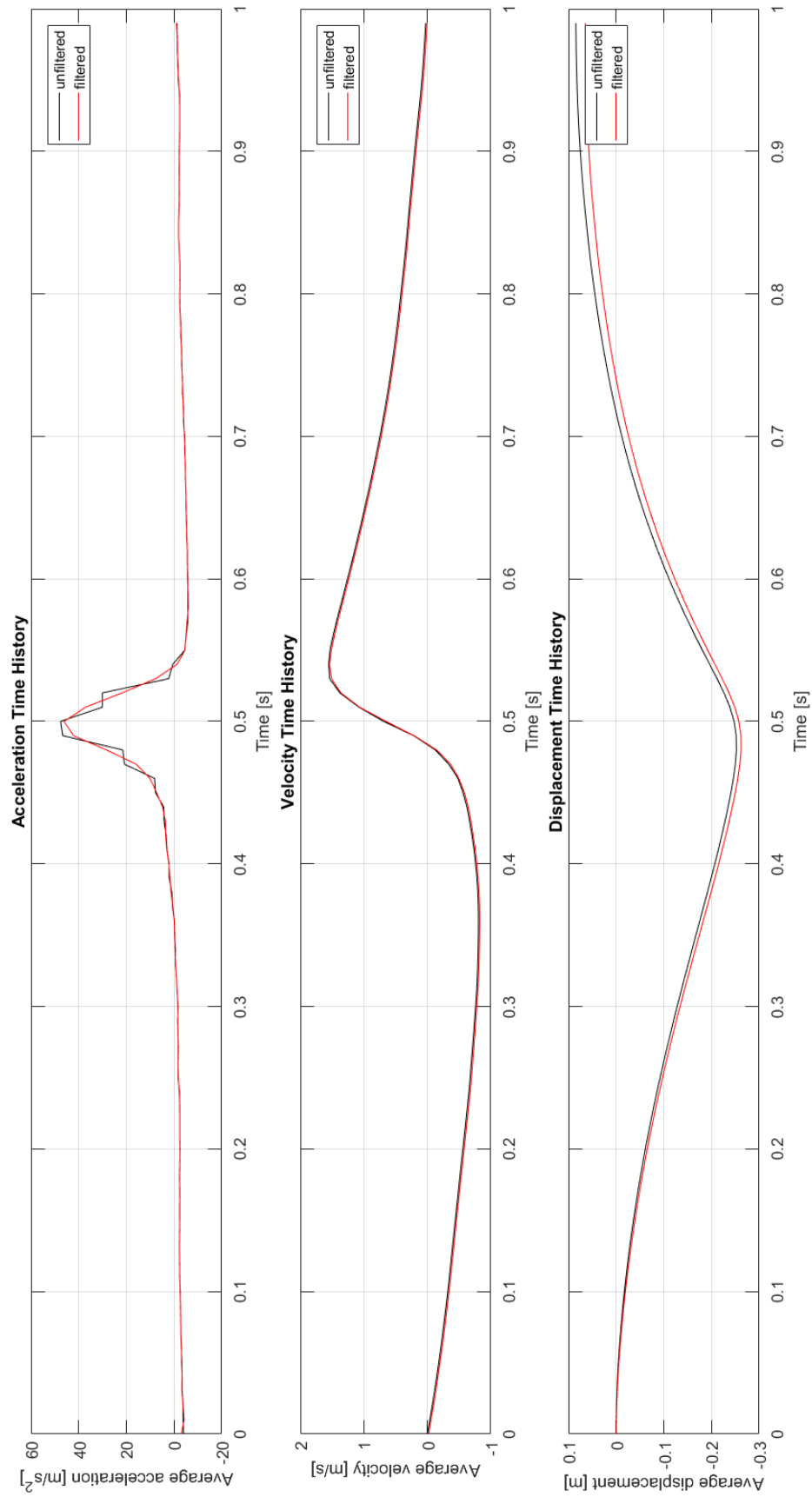


Figure B.9: Displacement response of the roller after 5 passes at location 270

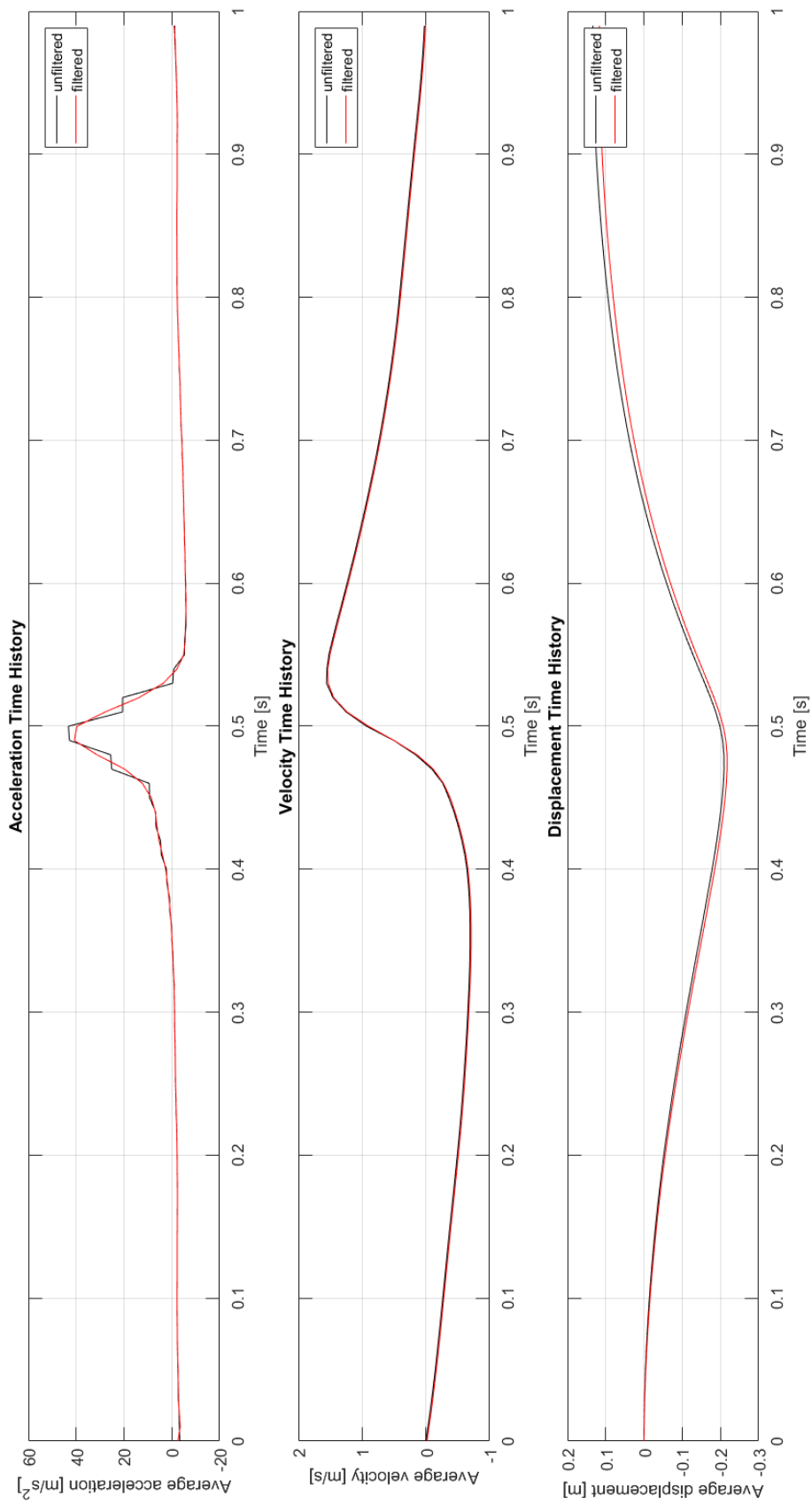


Figure B.10: Displacement response of the roller after 20 passes at location 270

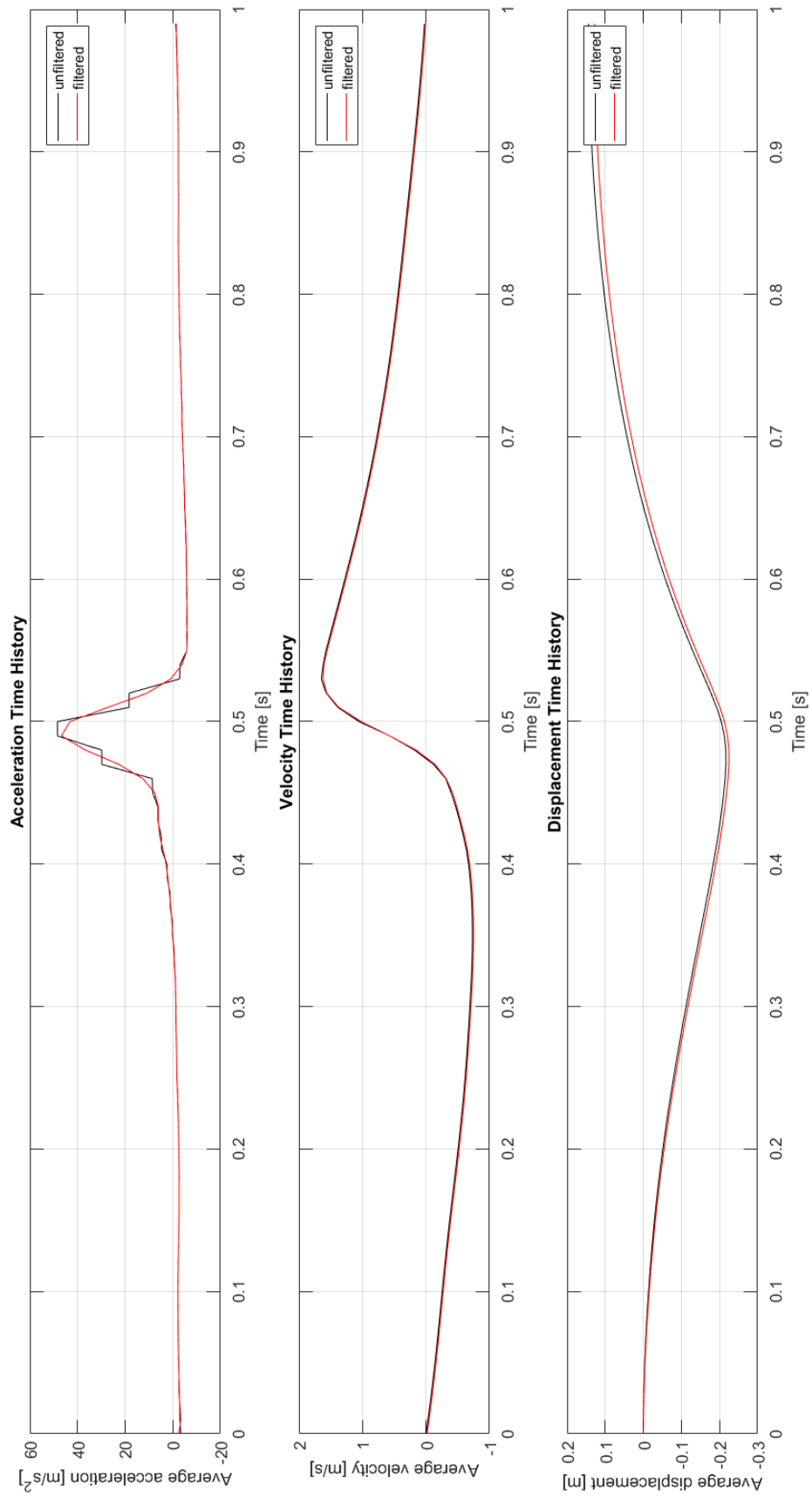


Figure B.11: Displacement response of the roller after 30 passes at location 270

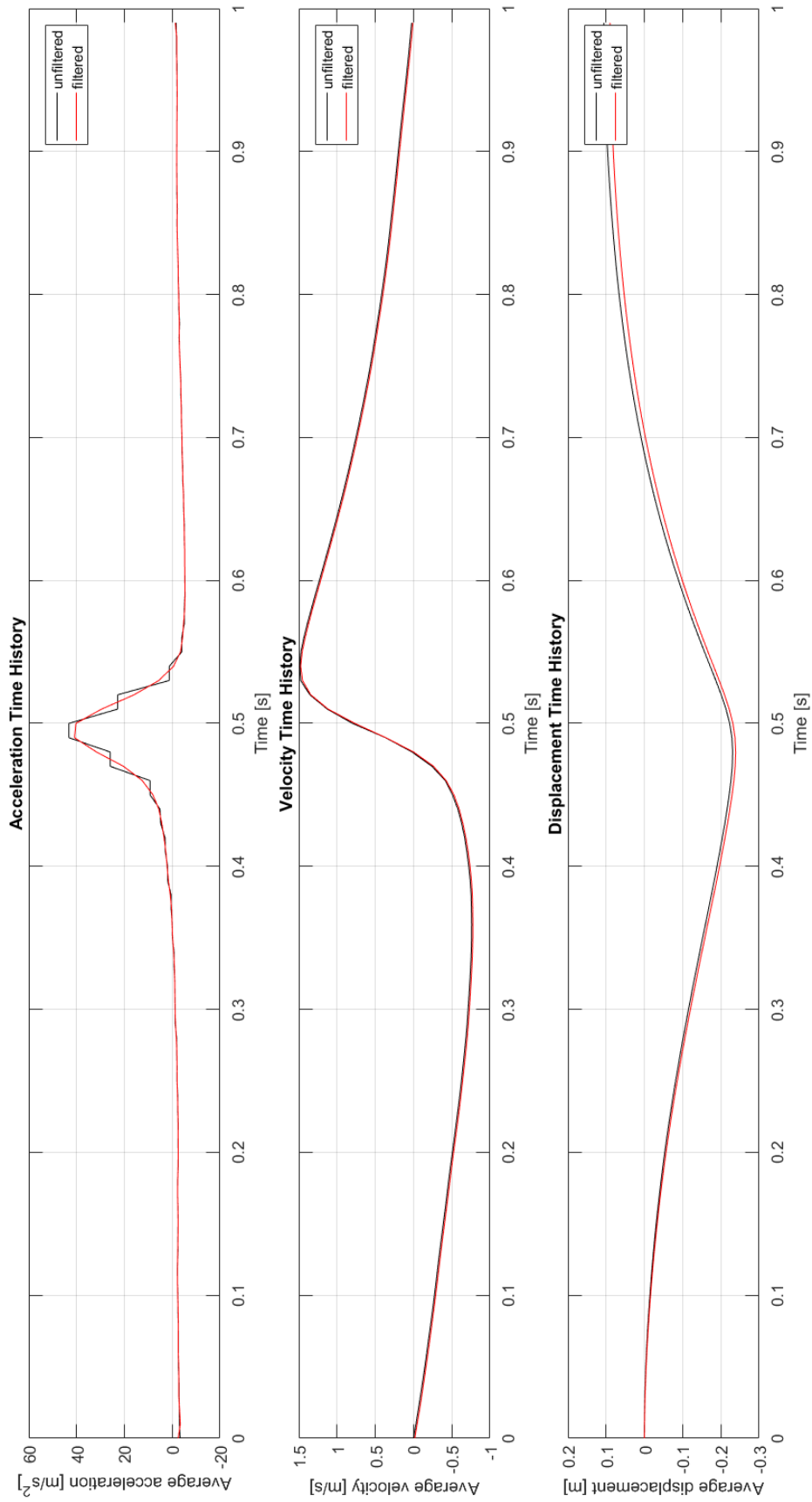


Figure B.12: Displacement response of the roller after 5 passes at location 281



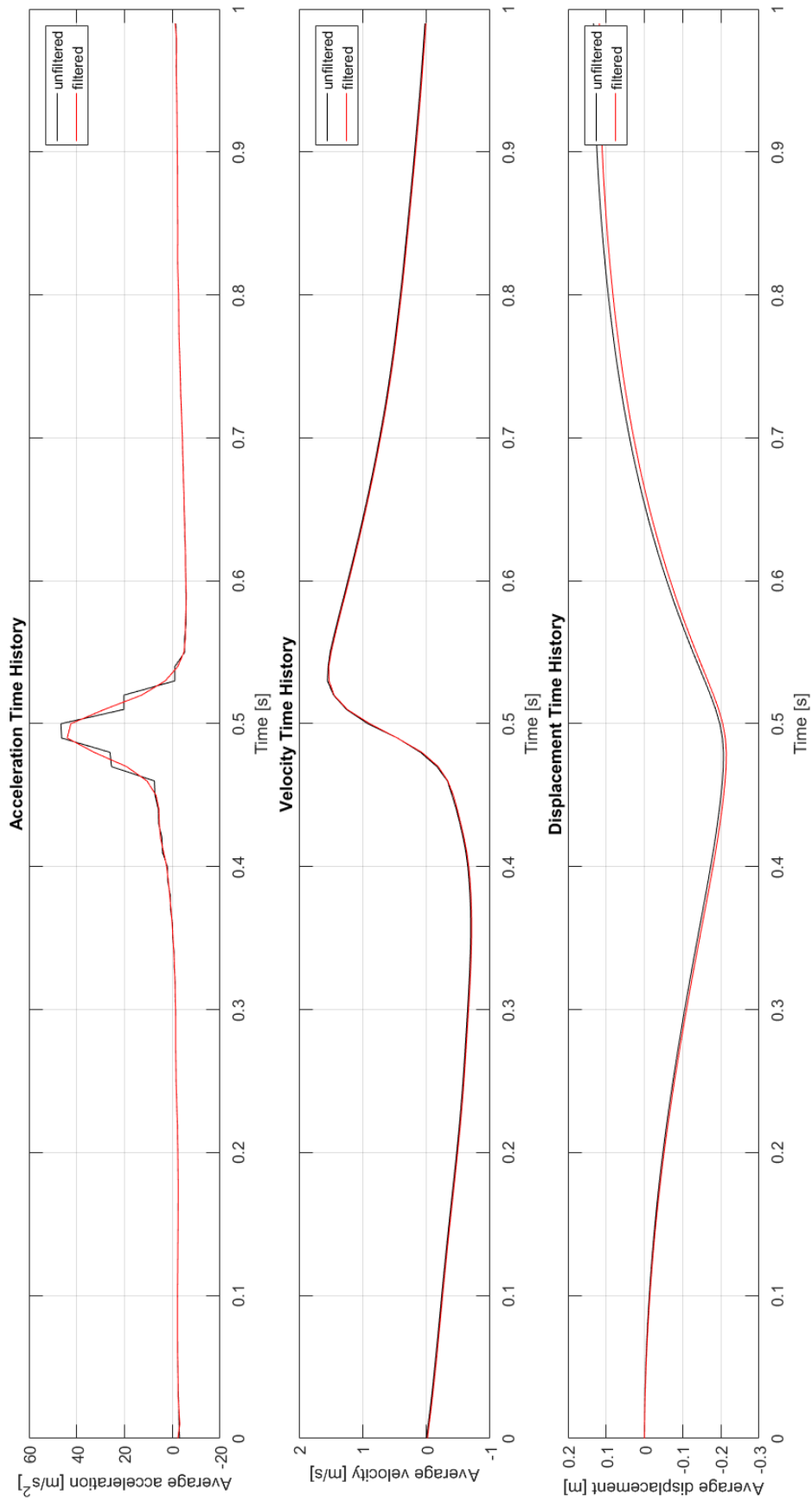


Figure B.13: Displacement response of the roller after 20 passes at location 281

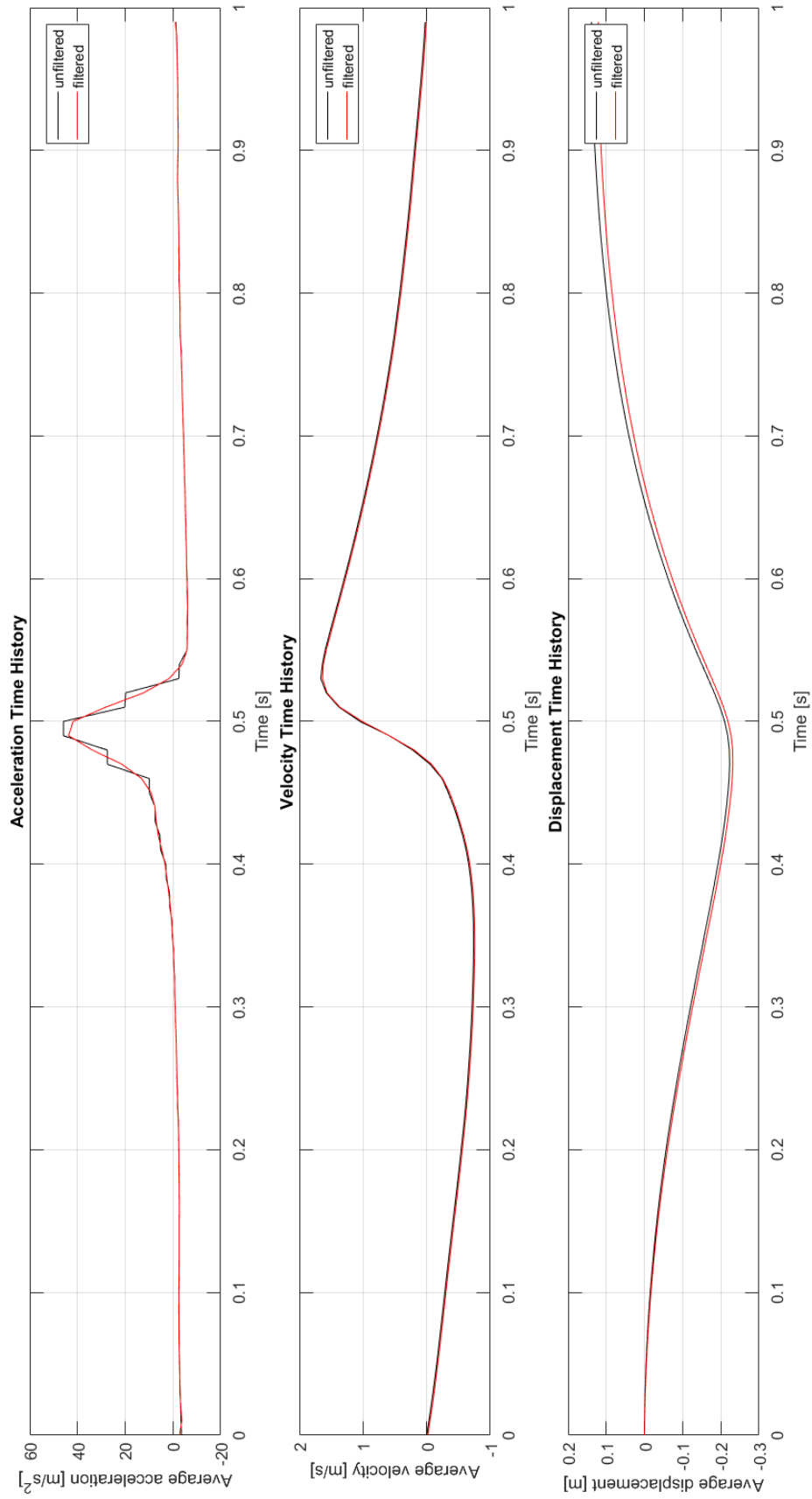


Figure B.14: Displacement response of the roller after 30 passes at location 281

**B.2.** Displacement response for the first 5 passes at location 270

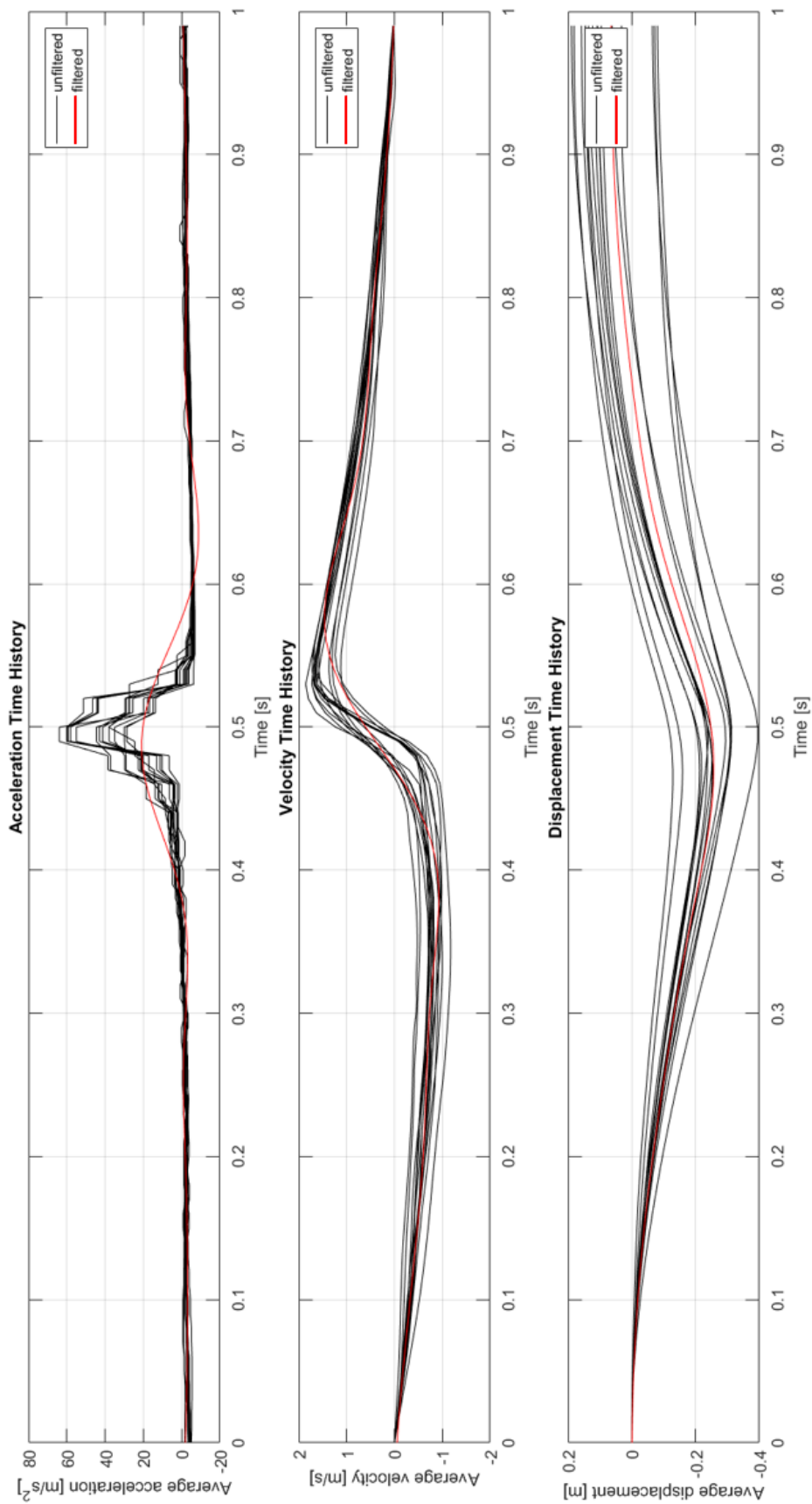


Figure B.15: Displacement response of the roller for 5 passes at location 270; Red signal depicts the filtered displacement response for the mean acceleration signal for 5 passes